June 2022

Nanophotonics and Nanomaterials for Microbial Inactivation

Sharad Ambardar
University of South Florida

Nanophotonics and Nanomaterials for Microbial Inactivation

by

Sharad Ambardar

A dissertation submitted in partial fulfillment
of the requirements for the degree of
Doctor of Philosophy
Department of Medical Engineering
College of Engineering
University of South Florida

Major Professor: Dmitri Voronine, Ph.D.
Robert Frisina, Ph.D.
Mark Jaroszeski, Ph.D.
Nathan Gallant, Ph.D.
Garrett Matthews, Ph.D.

Date of Approval:
June 24, 2022

Keywords: Integrating Cavity, Funneling, Tunneling, Nanobubbles, Quantum Plasmonics

Dedication

To my family and friends.

Table of Contents

List of Tables

List of Figures

Abstract

The study of light-matter interaction at nanoscale, also termed as nanophotonics, has gained vast attention due to its multidisciplinary application in the field of chemical engineering for the synthesis of nanomaterials, in the field of physics to study non-linear optical processes and optical phenomena in nanocavities and in the field of biology, biomedicine to study and develop novel optical nanoprobes for diagnostics, nanobiosensing and near-field imaging.

We studied UV-irradiation-based inactivation of SARS-CoV-2 and other respiratory viruses. In this work, we fabricated a device comprising a pulsed nanosecond 266 nm UV laser coupled to an integrating cavity (LIC), composed of a UV-reflective material, polytetrafluoroethylene (PTFE). This device overcomes the limitations of state-of-the art UV inactivation strategies via UV lamps by providing higher efficiency, low power and dose requirement and shorter irradiation times. Our results show that LIC device inactivated SARS-CoV-2 at ~ 1 millisecond effective irradiation time, with > 2 orders of magnitude higher efficiency compared to UV lamps. This LIC device due to its exceptional virus inactivation efficiency has a huge potential for development of real-time UV air and water purification systems.

Next, we used two-dimensional transition metal dichalcogenides (2D-TMDs), and their exceptional mechanical and optoelectronic properties provide flexible platform for nanophotonic engineering. Using strain engineering, continuous band gap tunability has been achieved in 2D TMDs. In our work, we presented a new method of nanobubble fabrication on monolayer 2D-lateral heterostructure (MoS_2-WS_2) using high temperature superacid treatment. We used tip enhanced photoluminescence (TEPL) spectroscopy to perform near-field imaging with nanoscale

resolution on the fabricated nanobubbles. TEPL nanoimaging revealed the coupling between MoS_2 and WS_2 nanobubbles with a large synergistic photoluminescence (PL) enhancement due to the plasmonic tip, hot electrons and exciton funneling. This work opens new avenue in exploration of novel nanophotonic coupling schemes. In addition, we used TEPL to analyze the optical properties of heterojunction, which are atomically thin p-n junction, formed by lattice mismatch of monolayer 2D TMDs. We performed picoscale control of quantum plasmonic PL at 2D heterojunctions and observed more than three-orders magnitude of PL enhancement than the pure material, due to the classical near-field mechanism and charge transfer across the junction. The controllable photoresponse of these lateral heterojunctions can be used to develop novel nanodevices for chemical and biosensing.

Finally, we utilized strong optical properties of 2D TMDs for detection of untreated and antibiotic-treated bacteria. We introduced two bacteria-2D TMD interaction models, mechanical and electrical. Using mechanical model we determined the intensity of the exciton funnels created by both untreated and antibiotic-treated bacteria. Our hypothesis states that an antibiotic treated bacteria forms weaker funnels because of the inhibitory effect of the antibiotic on the bacterial adhesion proteins. On the other hand, the electrical model involves two mechanisms, firstly tunneling from the plasmonic tip to the bacteria and to the 2D TMD and secondly, the charge transfer mechanism between the 2D TMD and bacteria. A correlated study using AFM, KPFM and TEPL measurements show that tunneling was more prominent in the case of the untreated bacteria at the bacterial adhesion sites (poles). Lastly, we show the application of heterojunction, by dropcasting bacteria on top of it. We observed tunneling was stronger at the junction than the pure materials, providing with new avenues for biosensing using heterojunctions.

Chapter 1: Introduction

1.1 UV-based Antiviral Therapy

UV spectrum is divided into three ranges UV-A (320 – 400 nm), UV-B (290 – 320 nm) and UV-C (200-290 nm)[1]. UV-C is the most efficient in antimicrobial activity, typically at 254 nm[2,3], which is also termed as germicidal UV. UV irradiation as an effective, non-contact method of viral pathogen inactivation has been used for a long time, mainly in the form of low-pressure mercury lamps or light emitting diodes (LEDs)[4–7]. The maximum absorption of nucleic acids is at 265 nm, with UVC light causing damage by inducing photochemical fusion of two adjacent pyrimidines into covalently linked dimers, RNA-protein cross-linking, and site-specific molecular damage[8]. Virus inactivation using UV radiation has been explored for the treatment of human enteroviruses (HuEV), zika, hepatitis E, dengue, west Nile and others[9–17] and more recently for SARS-CoV-2 [18–26]. Minamikawa et al. developed an irradiation apparatus to quantitatively analyze SARS-CoV-2 inactivation by DUV-LED and reported the dose dependence inactivation in various UV ranges required to inactivate 99.9% of SARS-CoV-2 as shown in Fig 1.1[24].

The virucidal efficacy of UV light is influenced by a number of factors, including the target pathogen, environment, and the material being decontaminated[27]. Further, germicidal UV has been combined with heat treatment for viral disinfection [28,29], including SARS-CoV-2 [30].
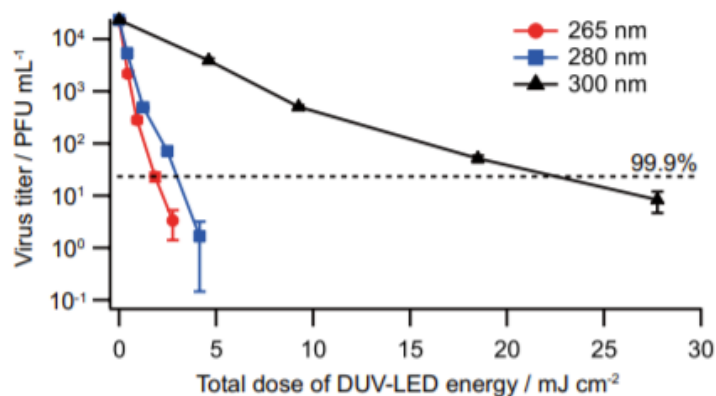
Figure 1.1 Inactivation efficacy at various deep UV (DUV) doses[24].

1.1.1 Mechanisms of Ultrafast Laser Based Viral Inactivation

Ultrashort laser pulses in the visible (Vis) at 425 nm and near-infrared (NIR) at ~ 800 nm ranges were reported to inactivate viruses [31–33]. It was suggested that impulsive stimulated Raman scattering resulting in aggregation of viral capsid proteins was the main inactivation mechanism [31]. However, the inactivation efficiency of the pulsed Vis-NIR irradiation is smaller than germicidal UVC lamps. Pulsed UVB lasers such as nanosecond excimer 308 nm laser were also used for viral inactivation but showed low efficiency similar to Vis-NIR [34] . High efficiencies were obtained using pulsed UVC lasers such as 193 nm excimer and 266 nm fourth harmonic Nd:YAG [35,36]. Nanosecond 266 nm UV pulsed laser irradiation revealed the nonlinear two-quantum mechanism of the RNA-protein crosslinking in inactivation of Venezuelan equine encephalomyelitis (VEE) virus with more than one order of magnitude increase of the quantum yield compared to the 254 nm UVC lamp [36]. This is contrasted with the linear one-photon nature of the conventional pyrimidine dimer formation mechanism which is present in both pulsed UV laser and UV lamp irradiation. Pulsed UV laser ablation is based on a combination of several mechanisms including thermal and photochemical decomposition that may increase viral inactivation efficiency beyond the conventional UV lamps. UV pulses contain more energy per

2

unit time and can penetrate solutions further than continuous UV light[35]. On the other hand, UV pulses correspond to stronger absorption than Vis or NIR pulses resulting in more effective inactivation.

1.2 2D Transition Metal Dichalcogenides (TMDs)

The unique physical properties of 2D transition metal dichalcogenides and their potential for opto-electronic applications make them one of the most important research areas. Additionally, their ultrathin thickness and tunable band gaps of ~ 1-2 eV, exhibit unique properties compared with their bulk counterparts[37–40], which makes them a great avenue for the fields of nanoelectronics, sensing and photonics[41–44].

Recently van-der Waals (vdW) heterostructures have gained wide attention due to their broad-range of optical bandgap and strong light matter interactions[45,46]. Different TMD layered materials, due to lattice mismatch, can form defect-free lateral atomically sharp interfaces. MoX₂-
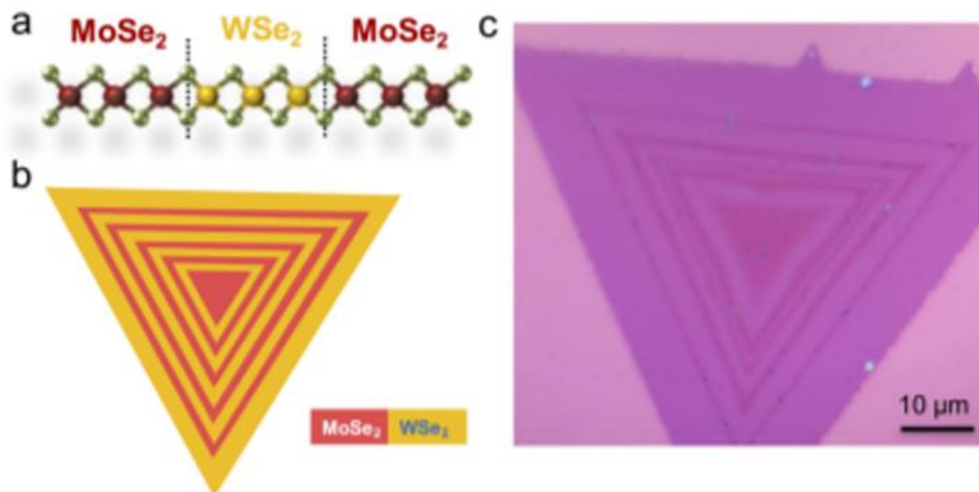
Figure 1.2 Lateral 2D heterostructure. (a) Schematic ball-model representation of a two-junction monolayer $MoSe_2$-WSe_2-$MoSe_2$ lateral heterostructure. A 2D nine-junction $MoSe_2$-WSe_2 lateral heterostructure, (b) schematic 2D representation and (c) optical image. Dark contrast and bright contrast represents $MoSe_2$ and WSe_2 domains, respectively[47]. Reproduced with permission from [Xue, W. et al. Nano-optical imaging of monolayer $MoSe_2$-WSe_2 lateral heterostructure with subwavelength domains. Journal of Vacuum Science & Technology A: Vacuum, Surfaces, and Films 36, 05G502 (2018)], Copyright AVS [2018].

WX$_2$ (X=S, Se or Te) heterointerfaces[47–50] form type-II energy band alignment that promotes the elecction-hole separation, which can be beneficial for solar cells, photosensors and harnessing interlayer excitons[51–53]. Figure 1.2 shows a chemical vapor deposition (CVD) grown 2D TMD heterostructure with multiple heterojunctions.

1.2.1 Biosensing Using 2D TMDs

Biosensors are powerful tools that monitor biological and biochemical processes which range from disease diagnosis to therapy and have been widely used for the detection of nucleic acids, proteins and small biomolecules. One important characteristic of a suitable biosensor is to amplify the detected signal especially for the detection of biological analytes which are present in a very low concentration levels and for which a suitable material is required[54].

2D TMDs with their unique physio-chemical and opto-electronic properties and their large specific surface areas, show great potential in the field of bio-sensing[55–58]. For example, MoS$_2$ and WS$_2$ nanoflakes were used for the fluorescence detection of nucleic acids, based on a signal-on sensing approach. The FAM-Lprobe molecule can be readily adsorbed onto TMD nanoflakes due to van der Waals forces of attraction between the basal plane of nanoflakes and the exposed to van der Waals forces of attraction between the basal plane of nanoflakes and the exposed nitrogenous bases of the FAM-Lprobe, giving rise to significant fluorescence quenching[56]. Ge et al. developed a novel fluorescence-activated DNA–MoS$_2$ nanosheet biosensor for detecting biomolecular targets such as proteins and small molecules based on the self-assembled architecture of a DNA aptamer and a MoS$_2$ nanosheet[59].

1.2.2 Exciton Funneling

Strained 2D materials can cause a variable band gap profile, leading to formation of new 'artificial materials' or 'artificial atoms' with unique and tunable optical properties[60–65]. Using a

smooth gradient of biaxial strain as previously shown on monolayer MoS_2[66,67] the band-gap of the strained material changes causing the photoexcited electron–hole pairs funnel towards the area of maximum strain. At this funneled area, the excitons recombine which produces a localized photoluminescence (PL) enhancement[65] shown in Figure 1.3. This process is termed "exciton funneling".
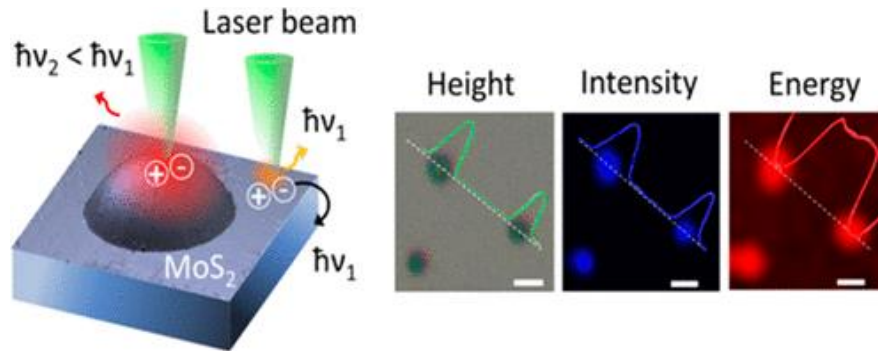
Figure 1.3 Exciton funneling demonstration. Strained-caused "artificial atoms" utilizes the exciton funnelling effect, which leads to enhancement in the PL near the bubble as compared to the flat region[65].

Chapter 2: Ultrafast UV Laser Integrating Cavity Mediated Inactivation of Viruses[i]

2.1 Introduction

Viral inactivation methods using Ultraviolet (UV) irradiation have provided an important avenue for inactivating severe acute respiratory-syndrome coronavirus-2 (SARS-CoV-2) virus. One of the major limitation with the state-of-the-art UV inactivation technology is that it is based on UV lamps, which requires high power and doses, long irradiation times and still are of limited efficiency. These drawbacks limit the use of UV lamps in air filtering systems and other applications. To overcome these drawbacks, herein we fabricated a device comprising of a pulsed nanosecond 266 nm UV laser coupled to an integrating cavity (LIC) composed of a UV reflective material, polytetrafluoroethylene (PTFE). Our viral inactivation results show that LIC device can inactivate several respiratory viruses including SARS-CoV-2, at ~ 1 millisecond effective irradiation time, with >2 orders of magnitude higher efficiency compared to UV lamps. To the best of our knowledge this is the first demonstration of LIC application for broad viral inactivation with high efficiency.

2.2 Materials and Methods

2.2.1 Laser Integrating Cavity Device (LICD)

Light absorption can be enhanced by coupling UV pulsed lasers to integrating cavities (ICs). Typical ICs have spherical geometry and walls made of highly reflective diffuse scattering materials[68,69]. The Lambertian light scattering from the walls generates uniform fields inside ICs

---

[i] This chapter has been accepted in Scientific Reports. https://www.nature.com/srep. Permission is included in Appendix D: Copyright Permission for Chapter 2.

and large effective optical path lengths, which have been used for sensing and spectroscopic applications[70–73]. Even though various UV boxes and cavities have previously been used for pathogen inactivation[74], the virucidal properties of ICs have not been much explored. The diffuse scattering nature of ICs has an advantage over the specular scattering of the conventional cavities by providing a larger range of illumination angles that may reduce the shielding of viruses by microparticles. Therefore, we hypothesized that pulsed UV laser coupled to ICs can destroy virus
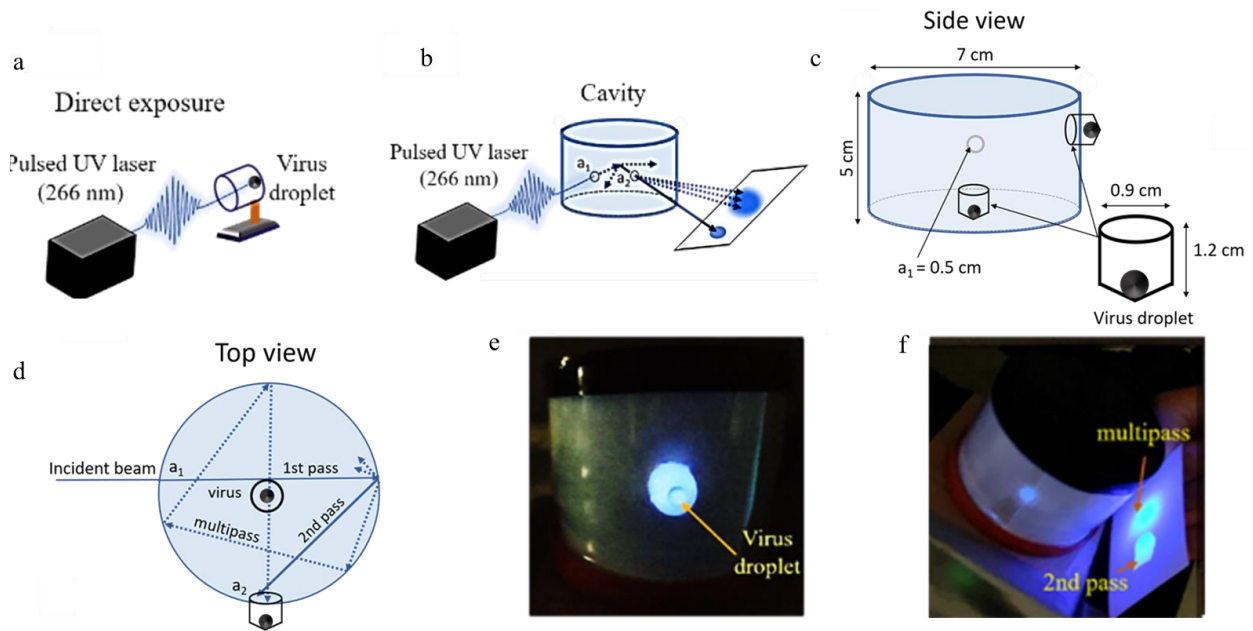
Figure 2.1 Virus inactivation using ultrafast UVC laser integrating cavity. (a) Schematic of the direct exposure of pulsed UV laser on a droplet of virus solution in a vial. (b) Schematic of the LICD exposure of UVC laser irradiation on a droplet of virus placed inside the cavity at the location of aperture a2. (c, d) Schematic of the integrating cavity. (c) Side view shows cavity dimensions, laser beam entrance aperture a1 and two plastic vials containing virus droplets, one at the bottom of the cavity and one on the side. (d) Top view shows the schematic of laser beam scattering inside the cavity. A vial with a virus droplet placed at the aperture a2 is illuminated by multiply scattered beams: the 2nd pass (solid line) and one of the multipass beams (dashed line) formed by diffuse scattering inside the integrating cavity are shown. (e) Photograph of the cavity with a virus droplet inside a vial. (f) Photograph of the cavity filled with UV laser light and the reflection of fluorescence from the 2nd pass and multipass scattering as two bright spots on a white card, placed at the a2 aperture.

more efficiently in reduced time. To test this hypothesis, we developed herein a new virus inactivation device based on a pulsed nanosecond 266 nm UV laser coupled to an integrating cavity, referred to as Laser Integrating Cavity Device (LICD).

Two different methods of laser exposure were investigated: (1) a direct exposure of the virus to the UV laser beam (Figure 2.1 a); (2) an indirect exposure of the virus to the UV laser irradiation when placed at a random location inside the LICD enclosure (Figure 2.1 b). We designed the LICD by coupling the 266 nm nanosecond pulsed UVC laser to a cylindrical IC enclosure with nearly Lambertian walls made of highly UV reflective polytetrafluoroethylene (PTFE) coating[75,76]. Detailed schematics and spatial dimensions of LICD are shown in the Figure (2.1 c, d).

For the direct exposure, a plastic vial was placed horizontally as shown in Figure 2.1 a and a virus droplet was held at the bottom of the vial. For the LICD exposure, one vial was randomly placed at the bottom and the second vial was randomly placed on the side wall of the enclosure as shown in Figure (2.1 e, f).

After the incident laser beam is reflected from the inner wall of the enclosure, the diffusely scattered light undergoes multiple reflections, uniformly filling the whole volume. The diffuse scattering efficiency can be estimated by observing the brightness of the two fluorescence spots on a white card placed at the exit aperture of the cavity (Figure 2.1 f). The spot from the 2nd pass is directly reflected from the cavity wall by the incident laser beam. The spot from the multipass scattering is of similar brightness, indicating high diffuse reflectivity of the cavity walls. The PTFE coating has omnidirectional diffuse reflectivity of $> 93\%$ due to the porous structure.

The optical path increase in the IC may be estimated using the approach of Fry, et al [68,71]. The average distance between reflections inside an integrating cavity $\bar{d} = 4.1$ cm is given by $\bar{d} =$

$4\frac{V}{S}$, where V is the cavity volume, and S is the surface area. The average path length inside the IC,

L = 63 cm was calculated by $L = 4\frac{V}{S(1-\rho)}$, where ρ = 0.935 is the IC reflectivity estimated from

the reflectivity of PTFE at 266 nm. The cavity enhancement factor (EF) for each virus was

calculated by $EF = \frac{k_{cavity}}{k_{direct}}$, where k_{direct} and k_{cavity} is the inactivation rate constant for the direct

and LICD exposure.

2.2.2 UV Irradiation

The following UV sources were used: i) Pulsed UVC source was 266 nm Nd:YAG

nanosecond pulsed laser (JDS Uniphase NanoLaserTM) with 1 mW average power, ~ 1 ns

temporal pulse duration, and 10 kHz repetition rate. ii) Pulsed UVB source was 337 nm nitrogen

laser (VSL-337ND) with 5.2 mW average power, < 4 ns temporal pulse duration, and 10 Hz

repetition rate. iii) Cw UVC lamp (Stratalinker® UV Crosslinker 1800) had 5 bulbs, 8 W each,

with 254 nm wavelength. iv) Cw UVC lamp (Handheld Wand, Clear-RazeTM) had a bulb of 18

W with 254 nm wavelength.

2.2.3 Cell Culture

Cell lines (Calu3 and Hep2) were purchased from the American Type Culture Collection

(ATCC, Virginia USA) and passaged no more than 25 times. Cells were cultured in a humidified

incubator at 37⁰C in a 5% CO_2 (Carbon Dioxide) atmosphere. Cells were cultured in tissue culture-

treated plates in the appropriate complete cell culture media [HEP2= DMEM (GE Healthcare)

containing 10% fetal bovine serum (FBS) (Atlanta Biologicals) and 1% penicillin/streptomycin

(GE Healthcare)] [Calu3= MEM (GE Healthcare) containing 20% FBS, 1% non-essential amino

acids (GE Healthcare), 1% 100mM sodium pyruvate (Gibco), and 1% penicillin/streptomycin].

2.2.4 Viral Infection

Three different viruses were used in these experiments. Red fluorescent protein (RFP) expressing respiratory syncytial virus (RSV-RFP), human coronavirus 229E (HCoV-229E), and SARS-CoV-2. HCoV-229E was obtained through BEI Resources, NIAID, NIH: Human Coronavirus, 229E, NR-52726. SARS-CoV-2 was provided to us by Dr. PEI-Yong Shi from the University of Texas Medical Branch, Galveston, TX, USA.[77]The strain of RSV used in all the experiments (RSV-RFP) was a recombinant A2 strain expressing a red fluorescent marker, mKate2, as well as the F protein from the clinical strain Line 19 (rA2-KL19F). Handling and storage of RSV-RFP and HCoV-229E, including all experimental procedures, were performed in a biosafety level 2 (BSL-2) laboratory. Handling, storage, and experiments using SARS-CoV-2 were performed in a BSL-3 laboratory. For all experiments, a monolayer of Hep2 (RSV-RFP) or Calu3 (SARS-CoV-2 and HCoV-229E) cells at 80% confluence was infected with various concentrations of the indicated virus MOI (as indicated in the figure legends). Cells were then incubated with the viral inoculum in Opti-MEM (Life Technologies) for 2 hours at 37°C. After this, the infectious medium was replaced by fresh growth media. Fluorescent microscopy (Keyence BZ-X800 or EVOS) was used to image cells and then the cell pellets were collected for RNA analysis.

2.2.5 Quantitative Reverse Transcriptase (qPCR)

Total cellular RNA was extracted from cell pellets using Trizol (Thermo Fisher Scientific) according to the manufactures' protocol. RNA was quantified using the Nanodrop (Thermo Fisher Scientific). One microgram of RNA was then reverse transcribed using the Maxima cDNA Reverse Transcription Kit (Thermo Fisher Scientific) according to the manufactures' protocol. qPCR performed on the cDNA was used to quantitate the relative expression levels of certain

genes to β-actin as a control. Real time analysis was performed using BlazeTaq SYBR Green qPCR Mix 2.0 (Genecoepia), according to the manufactures' protocol, in a Bio Rad CFX-384 thermocycler using primers obtained from Integrated DNA Technologies (IDT). The data was analyzed using ΔΔCt calculations and expression of all genes was normalized to β-actin expression as a housekeeping gene. Average fold change ±SEM, compared to control, was then calculated. Data analysis was performed using the CFX Maestro software (Bio-Rad).

2.2.6 Inactivation Kinetics

The results of inactivation experiments were analyzed using the qPCR relative gene expression data (Figures 2.2 and 2.5). The linear regression parameters in Table 1 were calculated using the first order kinetics given by $\ln(N/N0) = -k\ D$, where N/N0 is the survival fraction, N is the relative gene expression at each UV dose (D), and N0 is the relative gene expression at zero dose. The experiments were carried out in 3 replicates for HCoV-229E and 4 replicates for SARS-CoV-2. The inactivation rate constant, k (cm^2/mJ), was calculated for each virus strain and for both direct and LICD exposures. The load reduction doses to inactivate 90% (D_{90}), 99% (D_{99}) and 99.9% ($D_{99.9}$) of the virus are given by , $D_{90} = \frac{-\ln[1-0.9]}{k}$, $D_{99} = \frac{-\ln[1-0.99]}{k}$ and $D_{99.9} = \frac{-\ln[1-0.999]}{k}$.

2.3 HCoV-229E Inactivation

To investigate coronavirus inactivation, we used a direct exposure of the 266 nm nanosecond UVC laser to inactivate the HCoV-229E virus. A 6 μl virus droplet in PBS was placed in a vial as described above. The laser irradiation times of 1, 5, 10 and 30 s correspond to the doses of 3.5, 17.6, 35.3 and 105.9 mJ/cm^2. Upon the direct exposure of UVC laser, HCoV-229E replication was completely inactivated (99.9% reduction) after 4 s exposure, which corresponds to 15.6 ± 0.3 mJ/cm^2 dose, measured using qPCR for 229E spike (S) (Figure 2.2 c.) and nucleocapsid (N) (Figure 2.2 a.) transcripts after 72 hours of infection in Calu-3 cells. To investigate the effects

11

of the indirect exposure to the UVC laser on viral replication inside the IC enclosure, we performed

the LICD exposure of HCoV-229E virus droplet in PBS placed inside a vial at two random

positions inside the IC (shown in Figure 2.1c) with the irradiation times of 10, 30, 120 and 1800

s, which correspond to 0.05, 0.15, 0.6, and 9 mJ/cm^2 doses, respectively.
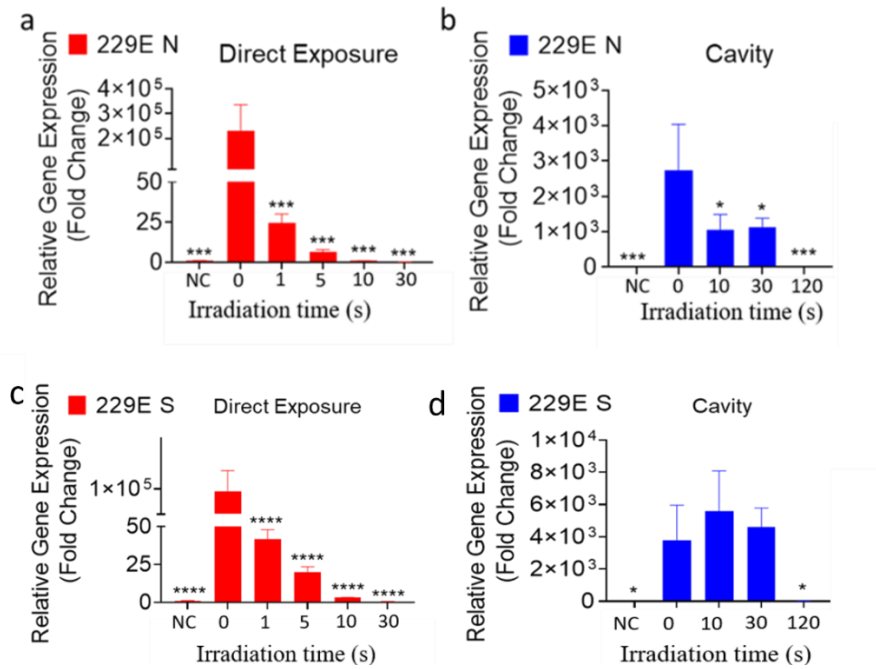
Figure 2.2 HCoV-229E virus inactivation. HCoV-229E virus was exposed to direct pulsed UVC laser (a, c) and cavity (b, d) for the indicated times. Calu-3 cells were treated 24 hours after seeding with the indicated groups of 229E (3 MOI).

After the UV dose of 0.63 ± 0.02 mJ/cm^2, HCoV-229E viral replication was inactivated

(99.9% reduction), when measured by qPCR for 229E S (Figure 2.2 d) and N (Figure 2.2 b)

proteins after 72 hours of infection in Calu-3 cells.

Figure 2.3a shows the log-linear survival plot of the direct inactivation kinetics, where N_0

and N are the initial and final concentrations of the infectious viral units determined from the qPCR

analysis. Only the linear part of the graph was fitted in agreement with the common approach, and

the small fraction of the tailing part was ignored[78] as described in the Methods section. The linear

regression fit resulted in the inactivation rate constant $k = 0.443 \pm 0.006$ cm^2/mJ. Figure 2.3b shows

the LICD survival plot and the linear fitting with the inactivation rate constant $k = 10.9 \pm 0.4$ cm^2/mJ. These results indicate that both direct and LICD exposure to pulsed UVC laser eradicate viral ability to replicate in host cells. However, the LICD is an order of magnitude more effective as it requires a lower dose to achieve similar inactivation.
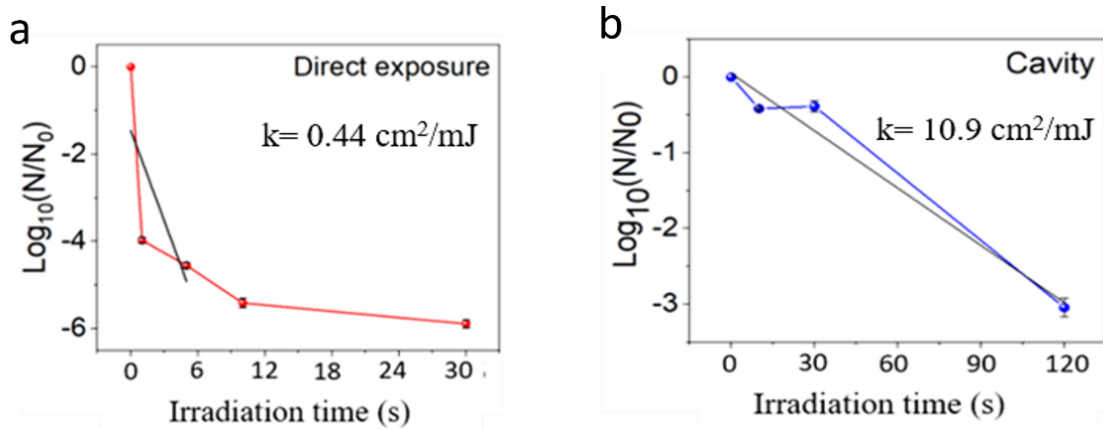
Figure 2.3 HCoV-229E survival plots. HCoV-229E survival as a function of UV irradiation time via direct (a) and cavity (b) exposure.

2.3.1 Morphological Analysis

To observe the morphological changes caused by the pulsed UVC laser exposure, we performed AFM measurements on the treated (irradiated by direct pulsed UVC laser) and untreated (non-irradiated) HCoV-229E virions (Figures 2.4c and 2.4a). For the statistical analysis, ten virions were selected from both treated and untreated samples. The average height of the untreated virions was ~ 31 nm, while the treated virions had an average height of ~ 19 nm (Figure 2.4b).The lateral width profiles showed the average width of the untreated virions ~ 159 nm and of the treated virions ~ 82 nm (Figure 2.4b). The AFM height profiles of the typical examples of the untreated and treated virions are shown in Figures 2.4c and 2.4d. These results indicate shrinkage of the viral

particles after exposure to ultrashort UVC laser pulses, confirming the contribution of the ablation mechanism to virus inactivation.
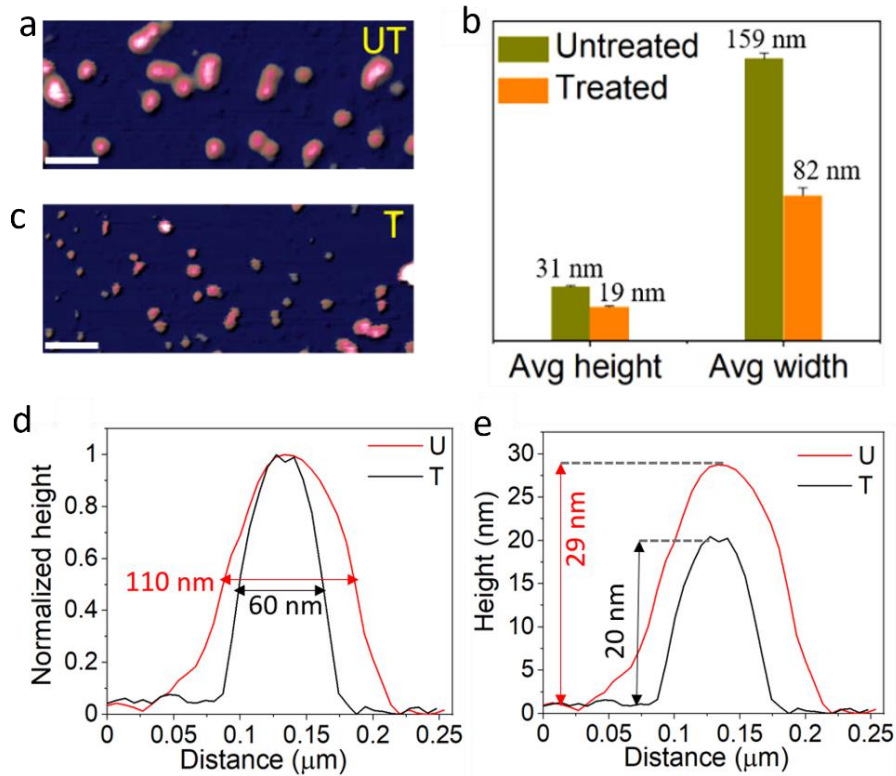
Figure 2.4 AFM height images of the untreated (UT) and UVC laser treated (T) HCoV-229E virions. Scale bar is 0.3 µm. (b) Average height and width of the untreated and treated HCoV-229E virions. (d) Normalized height profiles show the comparison of the virion width. (e) Height profiles show the comparison of the virion height.

2.4 SARS-CoV-2 Inactivation

Next we performed a direct exposure of the 266 nm nanosecond UVC laser to inactivate SARS-CoV-2. We used a 23 µl droplet of virus in PBS placed in a vial for the direct and LICD exposures as described above. The irradiation times of 30, 60, 120 and 300 s correspond to doses of 105.9, 211.8, 423.6 and 1059 mJ/cm^2, respectively. Upon the direct exposure of UVC laser, SARS-CoV-2 replication was inactivated (99.9%) after 3 min and 715 mJ/cm^2 dose exposure, measured using fluorescent microscopy (Figures 2.5 a – d) and qPCR for SARS-CoV-2 S

14
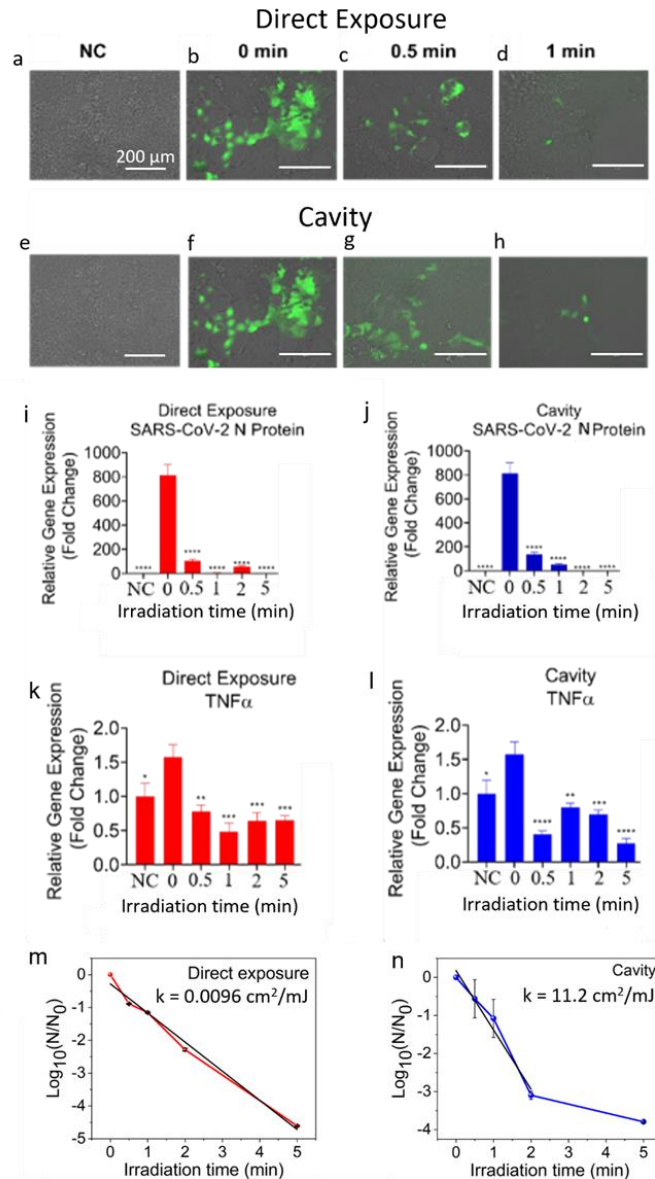
Figure 2.5 SARS-CoV-2 virus inactivation. SARS-CoV-2 virus was exposed to indicated irradiation times of direct or cavity UVC laser light. Calu-3 cells were infected 24 hours after seeding with the indicated groups of CoV-2 (0.1 MOI). (a - h) Images were taken 48 hours post-infection using the EVOS microscope (Thermo Fisher). 200X. Scale bar = 200 µm. (i – j) SARS-CoV-2 N protein expression in Calu-3 cells. At 72 hours post-infection RNA was extracted and qPCR performed. Average fold change ±SEM, compared to the negative control (NC), is shown (N=3). A 1-Way ANOVA and Dunnett's post hoc test was used to determine significance compared to 0 sec. (k - l) Inflammatory marker expression in Calu-3 cells after SARS-CoV-2 infection. For the negative control, CoV-2 was exposed to UVC light under a handheld wand for 2 minutes. At 48 hours post-infection RNA was extracted and qPCR performed. Average fold change ±SEM, compared to the negative control (NC), is shown (N=3). A 1-Way ANOVA and Dunnett's post hoc test was used to determine significance compared to 0 sec. SARS-CoV-2 survival as a function of irradiation time via direct exposure (m) and cavity (n). * = p<0.05, ** = p<0.01, *** = P<0.001, ****= P<0.0001.

15

and N (Figure 2.5i) proteins after 48 hours of infection in Calu-3 cells. We then performed the LICD exposure of SARS-CoV-2 with the irradiation times of 30, 60, 120 and 300 s corresponding to exposure doses of 0.15, 0.3, 0.6 and 1.5 mJ/cm^2, respectively. After the UV dose of 0.60 ± 0.02 mJ/cm^2, viral replication was inactivated (99.9% reduction), when measured using fluorescent microscopy (Figures 2.5e – h) and qPCR for SARS-CoV-2 S and N (Figure 2.5j) transcripts after 48 hours of infection in Calu-3 cells. SARS-CoV-2 infection usually results in a pathological increase of the inflammatory protein TNF-α[79].However, after exposure to both the direct (Figure 2.5k) and LICD (Figure 2.5l) UVC laser irradiation, SARS-CoV-2 infection causes significantly less TNF-α expression in Calu-3 cells. The linear regression analysis of the survival curve for the direct exposure in Figure 3m resulted in the inactivation rate constant of $k = 0.00965 \pm 0.00004$ cm^2/mJ. The linear regression fit for the LICD in Figure 3n resulted in the inactivation rate constant of $k = 11.2 \pm 0.1$ cm^2/mJ. This showed that LICD was three orders of magnitude more efficient than the direct exposure.

We next used the Calu-3 cell culture supernatant from the previous experiment to reinfect a new batch of Calu-3 cells with SARS-CoV-2. The cell culture supernatant containing the SARS-CoV-2 virus was exposed to the direct laser or LICD to inactivate the virus. The laser irradiation times were 60 and 120 s with 211.8 and 423.6 mJ/cm^2 doses for direct exposure and 0.3 and 0.6 mJ/cm^2 for LICD. Upon the direct exposure to the UVC laser, SARS-CoV-2 replication was completely inactivated at 211.8 mJ/cm^2 dose, measured using fluorescent microscopy (Figures 2.6 a – c) and qPCR for SARS-CoV-2 N (Figure 2.6e) transcript after 48 hours of infection in Calu-3 cells. After the UV dose of 0.6 mJ/cm^2, viral replication was inactivated in LICD, when measured using fluorescent microscopy (Figure 2.6d) and qPCR for SARS-CoV-2 N (Figure 2.6f) transcripts after 48 hours of infection in Calu-3 cells. These results show that after exposure to the direct

16

pulsed UVC laser or LICD, coronavirus samples, including SARS-CoV-2, are no longer able to cause a productive infection in cultured cells.
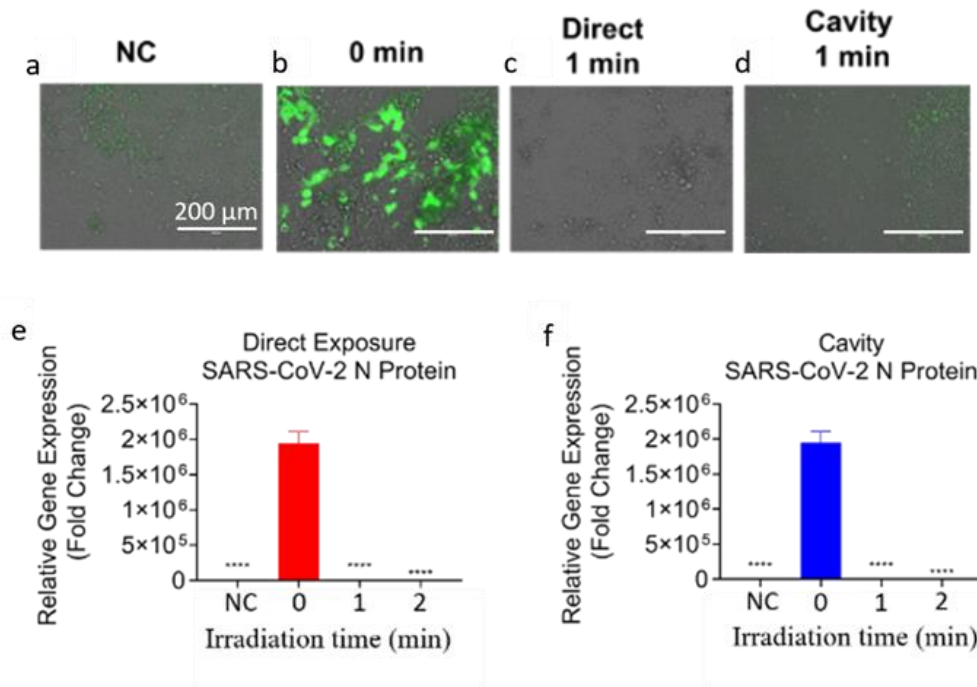
Figure 2.6 Reinfection of Calu-3 cells with culture supernatant from SARS-CoV-2 exposed to direct or cavity UVC laser light. (a - d) Images were taken 48 hours post-infection using EVOS microscope (Thermo Fisher). 200X. Scale bar = 200 µm. (e - f) SARS-CoV-2 N protein expression in Calu-3 cells. At 48 hours post-infection RNA was extracted and qPCR performed. Average fold change ±SEM, compared to the negative control (NC), is shown (N=3). A 1-Way ANOVA and Dunnett's post hoc test was used to determine significance compared to 0 sec. * = p<0.05, ** = p<0.01, *** = P<0.001, ****= P<0.0001

2.5 RSV-RFP Inactivation

To test LICD on a different respiratory virus, we next exposed RSV virus expressing red fluorescent protein (RSV-RFP) to direct 266 nm nanosecond pulsed UV laser with irradiation times of 1, 5 and 15 s with corresponding doses of 3.5, 17.6 and 52.9 mJ/cm^2 (Figures 2.7a-h). A dose of 17.6 mJ/cm^2 resulted in a complete viral inactivation in Hep2 cells at 72 hours post
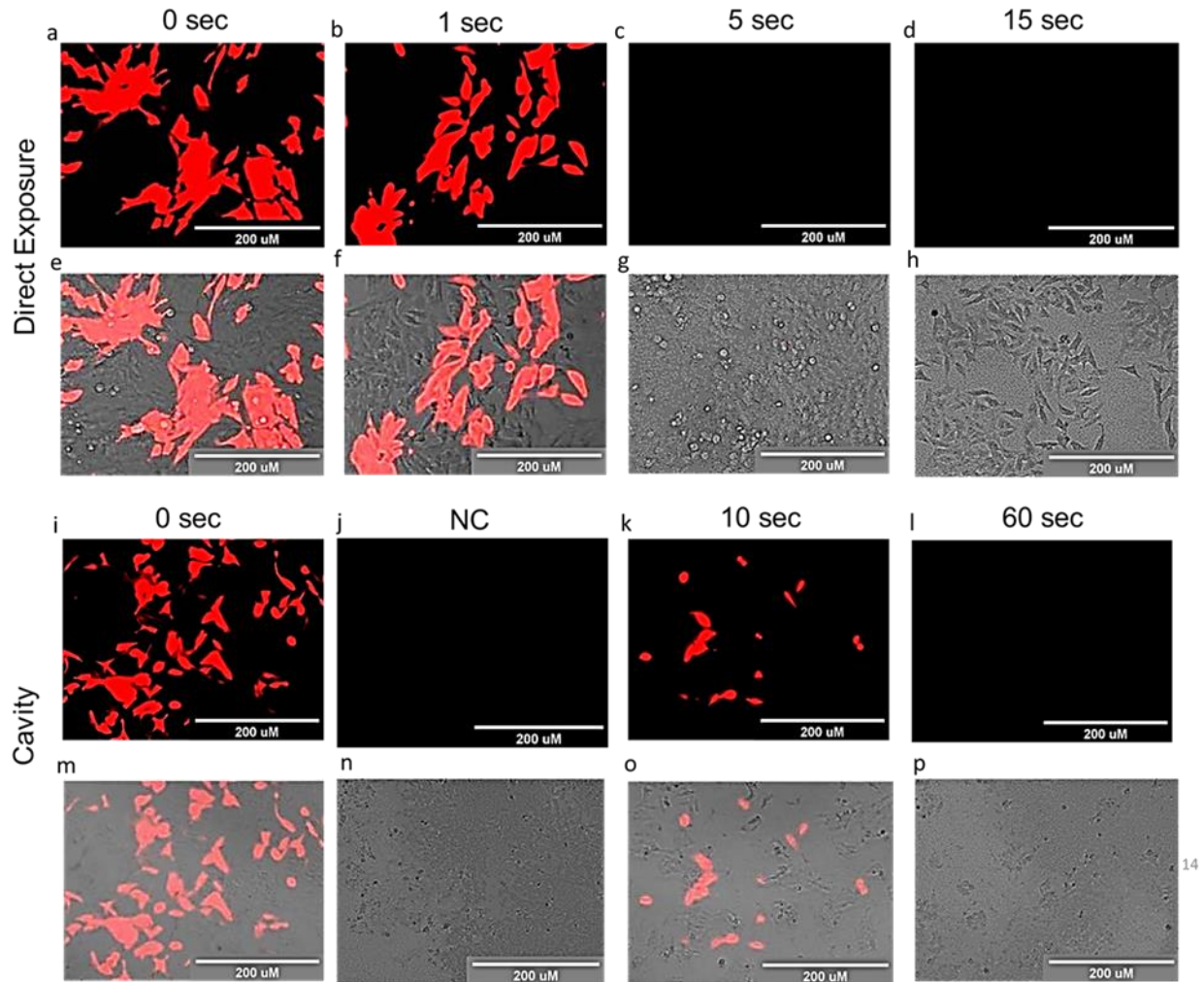
Figure 2.7 RSV-RFP inactivation. Direct UVC laser (a-h) and cavity (i-p) exposure of RSV-RFP virus. Hep-2 cells were treated 24 hours after seeding with the indicated groups of RSV-RFP (1 MOI) or the negative control (NC). Images were taken 72 hours post-infection using the Keyence BZ-X800 microscope. 200X.

infection when observed by fluorescent microscopy. RSV-RFP virus was then exposed to the LICD, which successfully inactivated RSV-RFP in Hep-2 cells at 72 hours of infection when exposed to doses as small as 0.3 mJ/cm^2, however, a dose of 0.05 mJ/cm^2 also inactivated most of the virus (Figures 2.7i - p).

As a control measurement, we also directly exposed the RSV-RFP virus to a 337 nm pulsed nanosecond UVB laser (Figure 2.8). The UVB laser irradiation had no inhibitory effect on the

RSV-RFP viral replication in Hep-2 cells. These results confirm the use of UVC pulsed laser radiation for viral inactivation.
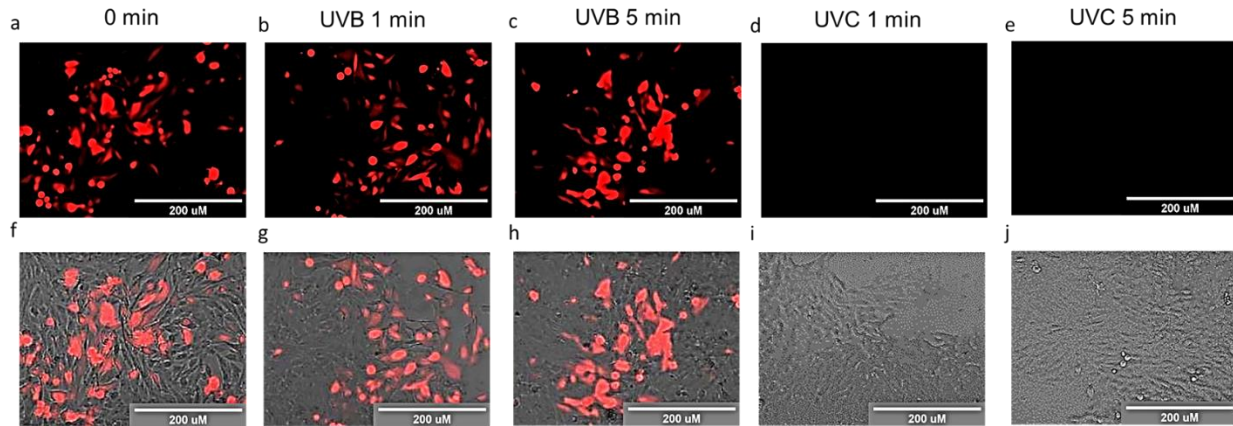
Figure 2.8 RSV-RFP exposure to UVB/UVC laser light. RSV-RFP virus was exposed to direct UVB or UVC laser light for the indicated times (a-j). Hep-2 cells were treated 24 hours after seeding with the indicated groups of RSV-RFP (1 MOI). Images were taken 96 hours post-infection using the Keyence BZ-X800 microscope. 200X.

We performed additional control measurements using two different UVC lamp sources for viral inactivation, Stratalinker unit (Figure 2.9 a-d) and a Handheld Wand (Figure 2.9 e-h).
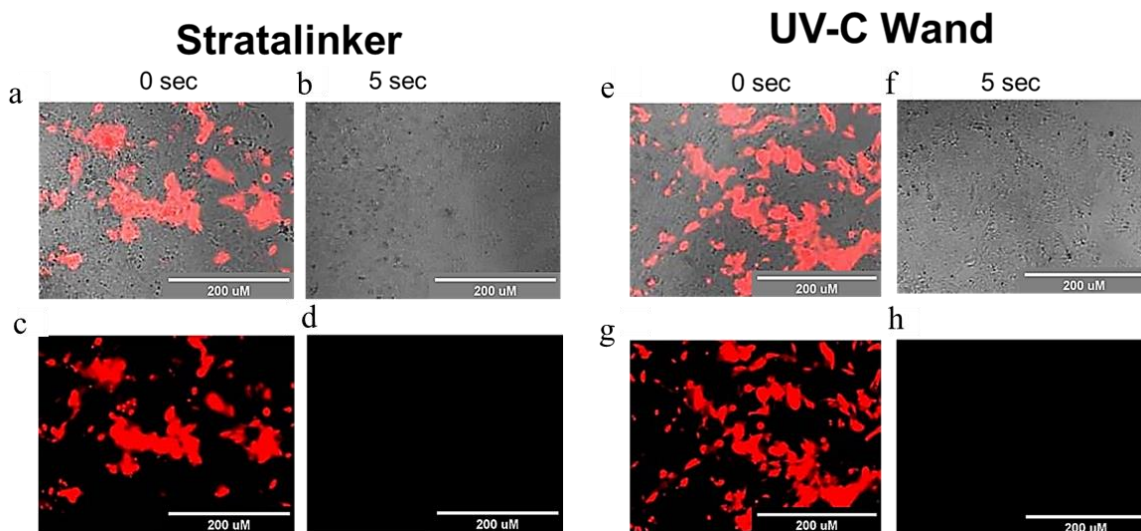
Figure 2.9 RSV-RFP virus exposure to UVC lamp .RSV-RFP virus was exposed to UVC lamp (Stratalinker and Handheld Wand) irradiation for the indicated times (a-d). Hep-2 cells were treated 24 hours after seeding with the indicated groups of RSV-RFP (1 MOI). Images were taken at 96 hours post-infection using the Keyence BZ-X800 microscope. 200X.

Both UVC lamps were able to inactivate the RSV-RFP viral replication in Hep2 cells at 72 hours post-infection with irradiation time of 5 s and a dose of 68.5 mJ/cm^2, when observed by fluorescent microscopy. However, two orders of magnitude higher inactivation efficiency was obtained using the LICD (dose of 0.6 mJ/cm^2, Table 1).

Table 2.1 presents the results of the linear regression analysis of the HCoV-229E and SARS-CoV-2 inactivation kinetics. The inactivation rate constants k were obtained from the survival curves described in the Methods section. Table 1 also shows the UVC dose needed to inactivate 90% (D90), 99% (D99), and 99.9% (D99.9). D99.9 represents the "complete inactivation" requiring 715 mJ/cm^2 for SARS-CoV-2 using the direct exposure, while only 0.6 mJ/cm^2 using the LICD. This difference is quantified as the cavity enhancement factor (EF) of 1160 (Table 2.1) given by the EF equation in the Methods section.

The complete inactivation (99.9%) of HCoV-229E required 15.6 mJ/cm^2 for the direct exposure, while only 0.63 mJ/cm^2 was needed using the LICD (Table 2.1), resulting in the EF of 25 due to the cavity. The inactivation rate constant for the LICD of k = 10.9. cm^2/mJ was similar

Table 2.1 Linear regression parameters from fitting of the survival curves for the direct pulsed UVC laser and LICD cavity exposures of the HCoV-229E and SARS-CoV-2. Cavity enhancement factors show the increase of the inactivation efficiency of the LICD compared to the direct exposure

Virus	Exposure	k (cm^2/mJ)	D90 (mJ/cm^2)	D99 (mJ/cm^2)	D99.9 (mJ/cm^2)	Cavity enhancement
HCoV-229E	Direct	0.44 ± 0.01	5.1 ± 0.1	10.4 ± 0.2	15.6 ± 0.3	25
	Cavity	10.9 ± 0.4	0.21 ± 0.01	0.42 ± 0.02	0.63 ± 0.02	
SARS-CoV-2	Direct	0.00965 ± 0.00004	238 ± 1	476 ± 2	715 ± 3	1160
	Cavity	11.2 ± 0.1	0.201 ± 0.003	0.41 ± 0.01	0.60 ± 0.02	

to that of SARS-CoV-2 for LICD. However, a larger rate constant of $k = 0.44$ cm^2/mJ for the direct pulsed UVC exposure of SARS-CoV-2 was obtained compared to $k = 0.01$ cm^2/mJ for HCoV-229E. This difference could be attributed to a smaller droplet size (6 μl) and structural and morphological differences.

2.6 Discussion and Conclusion

The obtained inactivation rate constant for LICD exposure $k = 11.2$ cm^2/mJ is more than an order of magnitude larger than the previously observed rate constants for most ssRNA viruses using UVC lamps at 254 nm and ~ 5 times larger than that predicted for SARS-CoV-2.[78] On the other hand, the observed $k = 0.01$ cm^2/mJ for the direct exposure is by an order of magnitude lower than the typical literature values for other ssRNA viruses using 254 nm lamps. This difference could be explained by the different experimental conditions such as the relatively large droplet size of the SARS-CoV-2 solution (23 μl) and absence of stirring. These effects could lead to light attenuation in the sample and lower k values. Note that these effects, however, do not affect the EF values, which show the increase of the inactivation efficiency due to the IC effect.

A major difference between the UVC lamp and a pulsed UVC laser exposure from the applications point of view is in the effective irradiation time, which is much shorter for the pulsed laser. The total duration of laser exposure per unit time may be obtained by multiplying the nanosecond pulse duration by the pulse repetition rate. This results in the effective total irradiation time to inactivate both HCoV-229E and SARS-CoV-2 coronaviruses of ~ 1 ms using LICD, while only ~ 0.1 ms to inactivate RSV. Similar inactivation times are required for the direct exposure but with larger doses due to the difference of the illumination areas of the direct (~ 0.2 cm^2) compared to the LICD (~ 200 cm^2). Due to the differences in the genome organization and composition of

the non-structural proteins these three viruses allow us to demonstrate the broad range inactivation ability of the pulsed UVC laser and LICD.

In these studies, we performed fast inactivation of viruses using a pulsed 266 nm nanosecond UVC laser toward developing a broad anti-viral LIC device. To test this novel system, we used 3 different types of viruses including HCoV-229E, RSV-RFP and SARS-CoV-2. A comparison of the LICD, fabricated using a highly UV diffuse scattering material PTFE, with the direct exposure of the UVC laser beam, demonstrated efficient viral inactivation after exposure to LICD. The time needed for inactivation might be further reduced by increasing the laser power, by using additional optical elements, and improving the diffuse reflecting properties of the device with more advanced reflective materials. Also, beyond viral inactivation, the application of LICD may be extended to other pathogens such as bacteria[80–82] and mold[83]. The technological progress in the development of UV lasers is envisioned to reduce the cost and make the LICD technology widely available in the near future. The application of LICD to air and water purification systems will benefit from the increased inactivation efficiency. LICD-based air conditioners may be used in enclosed spaces such as airplanes, stores and offices. LICD-based water purification systems may be used in household and industrial settings. PTFE-coated water pipes would be useful in conjunction with their anti-fouling properties for wastewater treatment[84].

The LICD may be used in public places due to the enclosed protection of the UVC exposed volume by the cavity. In general, exposure of skin to UVC radiation may cause oxidative damage by either the direct absorption of UV or by the reactive oxygen species[85]. However, it has been reported that low doses of far-UVC light (207–222 nm) may be harmless to the exposed human tissues[6]. Additionally, aluminum nanoparticles were proposed as shielding agents in a quantum

medical approach based on UV radiation to significantly decrease the risk of photodamage of

healthy tissues, while inactivating pathogens[86].

Chapter 3: Exciton Funneling in 2D Heterostructures[ii]

3.1 Introduction

Two-dimensional (2D) transition metal dichalcogenides (TMDs) have recently emerged as promising materials for optoelectronic applications[87,88]. Lateral and vertical heterostructures of 2D TMDs may be used to design new devices with controllable functionalities[89–92]. Micro and nano-sized bubbles in graphene revealed unique elastic and optical properties[93,94]. Monolayer TMDs have been studied by strain engineering to control photoluminescence (PL)[65,95–97]. Strain was correlated with bubble topography[65,98]. Additionally, nanobubbles, nanotents and other nanostructures have been fabricated, having unique properties of quantum emitters[99–102]. These materials have enabled new explorations of fundamental physics at the nanoscale.

Heterogenous properties of 2D materials affect their nano-optical response. For example, superacid treatment by bis(trifluoromethane) sulfonimide (TFSI) was previously used to enhance the PL of MoS_2 [103,104]. However, previous work on characterization of micro/nano-sized bubbles was focused on single materials, without the comparison of the properties of bubbles in different TMDs under similar conditions, such as lateral heterostructures. Strain was used to create localized areas of high PL intensity, so-called "artificial atoms", with tunable band gap via exciton funnelling[65,105,106]. However, conventional far-field (FF) PL characterization techniques provide limited information about the nanoscale properties of nanobubbles. Therefore, we used high

---

[ii]This chapter was published in Nanoscale., Reference[151] (Ambardar, S., Kamh, R., Withers, Z. & Voronine, D. V. Coupling nanobubbles in 2D lateral heterostructures. Nanoscale (2022)). https://pubs.rsc.org/en/content/articlehtml/2022/nr/d2nr00512c. Permission is included in Appendix E: Copyright Permission for Chapter 3.

resolution near-field (NF) tip-enhanced PL (TEPL) imaging to improve the nanobubble characterization. Previously, NF PL imaging was used for characterizing excitons in MoS_2[107–110] and WS_2[111–113], 2D nanobubbles[98], local strain control in WSe_2[114] , probing dark excitons[115], and studying the nanoscale heterogenous[116–118] and quantum plasmonic effects [119] in 2D heterostructures. TEPL is based on the predominantly out-of-plane excitation by the electric field component polarized along the tip axis, perpendicular to the sample plane, which is less efficient than the in-plane excitation of 2D materials. TEPL signals can be enhanced by out-of-plane protrusions such as bubbles and wrinkles[120,121]. Synergistic enhancement of MoS_2 PL by TFSI and gold nanoparticles has also been shown[122].

Here, we fabricated MoS_2 and WS_2 nanobubbles in monolayer 2D lateral heterostructure using high temperature TFSI treatment. We characterized nanobubbles using high-resolution TEPL imaging, which is not limited by diffraction, to obtain information about PL enhancement mechanisms and coupling. We observed large synergistic enhancement of PL signals, due to the coupled plasmonic antenna, hot electron, and exciton funnelling.

3.2 Experimental Setup

Coupling nanobubbles in 2D materials is challenging due to their nanoscale size and limitations of the conventional fabrication and characterization techniques. Far-field PL imaging of exciton funneling was previously used to characterize TMD bubbles[65,102]. Figure. 3.1A shows schematically that in isolated bubbles excitons are symmetrically attracted (dashed arrows) to the regions of smaller band gap in bubbles. However, the proximity of the two bubbles causes the band edge asymmetry (Figure. 3.1B), resulting in the directional funnelling from WS_2 bubble to MoS_2 bubble, coupling the bubbles (solid arrows in Figure. 3.1A).
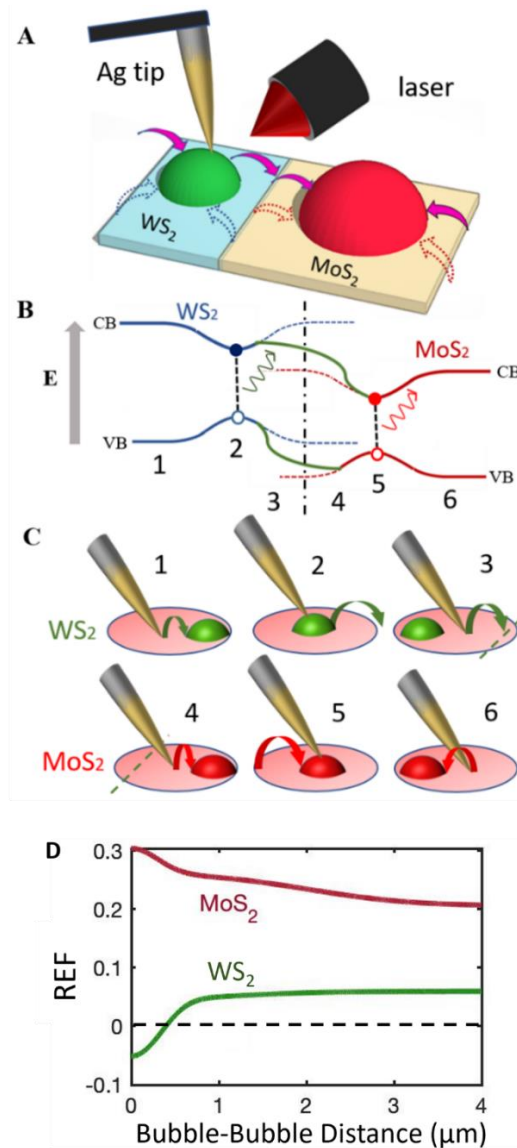
Figure 3.1 Sketch of tip-enhanced photoluminescence (TEPL) experiment showing coupled MoS_2 and WS_2 nanobubbles (solid arrows). (A) Funnelling is symmetric in the uncoupled bubbles (dotted arrows). (B) Schematic energy diagram for the symmetric uncoupled (dashed) and directionally coupled (solid) WS_2 and MoS_2 nanobubbles. (C) Tip-sample-laser configurations showing laser excitation spot (red oval) with tip on flat (1,6), bubble (2,5), and junction (3,4) areas. (D) Theoretical relative enhancement factor (REF) as a function of bubble-to-bubble distance.

The photocarriers generated by excitons separated at the junction can transfer across the junction[123]. The transfer distance can be increased due to funneling to several hundred nm, which corresponds to the typical bubble width. Similar transfer of hot electrons across the junction was

26

previously observed using TEPL in MoSe$_2$-WSe$_2$[124] and MoS$_2$-WS$_2$[125] heterostructures without bubbles. Therefore, the junction also has a direct effect on the funnelling and PL distribution in the vicinity of the bubbles, as shown here. Conventional confocal PL imaging is limited in the spatial resolution of a few hundred nm. In contrast, TEPL has a spatial resolution of ~20 nm, and can be used to determine the PL enhancement and directional coupling of WS$_2$ and MoS$_2$ nanobubbles via a 2D lateral heterojunction.

3.3 Enhancement Mechanisms

We identified four PL enhancement mechanisms: (i) bubble enhancement, which includes exciton funnelling; (ii) electromagnetic near-field tip enhancement; (iii) out-of-plane polarization tip enhancement on bubble; and (iv) synergistic enhancement due to the bubble-bubble coupling via exciton and hot electron funnelling.

Different mechanisms contribute to the PL enhancement when the tip is placed at different sample locations. Figure. 3.1C shows six tip-sample-laser configurations, which correspond to the locations 1-6 in Figure 3.1B, when the tip is placed on the bubble (2,5), near the junction (3,4), or on flat areas near the bubble but far from the junction (1,6). Plasmonic Ag tip plays a role of a nanoantenna generating a larger number of excitons in a localized area (receiver) and enhancing the PL signal (emitter). Solid arrows in Figure 3.1C illustrate the transport of excitons and photocarriers in coupled bubbles. Depending on tip location, excitons generated by the near and far fields transfer in and out of the tip-enhanced recombination area, leading to modified PL enhancement factors (EF). For example, when the tip is placed on the flat WS$_2$ (1) or MoS$_2$ areas (6) near the bubble, the tip-enhanced excitons transfer toward the bubble leading to a reduced EF. When the tip is placed on the coupled WS$_2$ (2) and MoS$_2$ bubbles (5), the photocarriers generated

by separated funnelled excitons transfer across the junction, reducing PL of WS$_2$ and enhancing PL of MoS$_2$[124] .

Figure 3.2 shows the graphical representation of six different EFs given by Eqs. (1) – (6) based on different combinations of the four enhancement mechanisms (i) – (iv), which are marked by the "x" symbols in Table 3.1 and are indicated by the following graphical symbols. Large red circle indicates the FF enhancement of the PL signal due to the funnelling mechanism (i) of the bubble. It is present in Figures. 3.2A, 3.2E and 3.2F and contributes to Eqs. (1), (5) and (6). Blue shade on bubble indicates the NF enhancement of the PL signal due to the funnelling mechanism (i) of the bubble. It is present in Figures. 3.2B, 3.2E and 3.2F and contributes to Eqs. (2), (5) and (6). Blue shade on tip indicates the NF enhancement of the PL signal due to the conventional TEPL mechanism (ii) on flat sample. It is present in Figures. 3.2C, 3.2D, 3.2E and 3.2F and contributes to Eqs. (3), (4), (5) and (6). Small yellow circle indicates the enhancement of the PL signal due to the out-of-plane tip-bubble mechanism (iii). It is present in Figures. 3.2B, 3.2D, 3.2E and 3.2F and contributes to Eqs. (2), (4), (5) and (6). Red arrow indicates the synergistic PL signal enhancement (or quenching) due to the bubble coupling mechanism (iv). It is present in Figure. 2F and contributes to Eqn. (6).

We obtained the following EF equations based on different combinations of the experimentally measured FF and NF PL signals on bubble (B) and flat (F) areas. Eq. (1), shown in Figure 3.2A, describes the enhancement factor EF_{Out}^{BF} obtained by the ratio of FF PL signals on bubble I_{FF}^{B} and flat I_{FF}^{F} areas. This describes the FF bubble funnelling mechanism (i). If there is no funnelling, then the PL signals on both areas are the same, and the ratio of I_{FF}^{B} and I_{FF}^{F} equals 1, leading to $EF_{Out}^{BF}= 0$. Figure 3.2A shows the graphical representation of this EF by the large red circle indicating the FF funnelling mechanism (i).

Eq. (2), shown in Figure 3.2B, is the NF analog of Eq. (1). It describes the enhancement factor EF_{In}^{BF}, obtained by the ratio of NF PL on bubble (I_{NF}^B) and flat (I_{NF}^F) areas. This describes the mixed contribution of the NF bubble funnelling mechanism (i) and the out-of-plane polarization bubble-tip enhancement mechanism (iii). If there is no PL enhancement on the bubble, then the PL signals on both areas are the same, and the ratio of I_{NF}^B and I_{NF}^F equals 1, leading to $EF_{In}^{BF} = 0$. Figure 3.2B shows the graphical representation of this EF by the blue shade on bubble indicating the NF enhancement due to the funnelling mechanism (i) and by the small yellow circle indicating the enhancement due to the out-of-plane tip-bubble mechanism (iii).

Figure 3.2 Graphical representation of the PL enhancement factors for coupled WS_2 and MoS_2 nanobubbles.

Eq. (3), shown in Figure 3.2C, is the conventional TEPL equation due to mechanism (ii) used to calculate the EF from the comparison of the measured PL intensities on the flat area with tip ($I_{Tip\ In}^F$) and on the flat area without tip ($I_{Tip\ Out}^F$) with the multiplication by the surface area scaling factor ($\frac{S_{FF}}{S_{NF}}$):

$$\mathrm{EF_{In}^F} = \left(\frac{I_{Tip\ In}^F}{I_{Tip\ Out}^F} - 1\right) \times \frac{S_{FF}}{S_{NF}} = \frac{I_{NF}^F}{I_{FF}^F} \times \frac{S_{FF}}{S_{NF}},$$

where $I_{Tip\ Out}^F = I_{FF}^F$ corresponds to the measured FF PL signal with the tip out of contact with the

sample, and $I_{Tip\ In}^F = I_{NF}^F + I_{FF}^F$ corresponds to the measured PL signal when the tip is in contact

with the sample. The scaling factor $\left(\frac{S_{FF}}{S_{NF}}\right)$ is used to make sure that the same number of molecules

is used for the comparison of the NF and FF signals. If there is no near field enhancement on the

flat area, then $I_{NF}^F = 0$ and there is no TEPL, leading to $\mathrm{EF_{In}^F} = 0$. Figure 3.2C shows the graphical

representation of this EF by the *blue shade on tip* indicating the near-field enhancement of the PL

signal due to the conventional TEPL mechanism (ii).

Eq. (4), shown in Figure 3.2D, is the bubble analog of Equation (3). The enhancement

factor $\mathrm{EF_{In}^B}$ has contributions of both the in-plane (ii) and out-of-plane (iii) mechanisms, and is

obtained by the tip-in and tip-out measurements on the bubble area analogous to those on flat area

described in Equation (3):

$$\mathrm{EF_{In}^B} = \left(\frac{I_{Tip\ In}^B}{I_{Tip\ Out}^B} - 1\right) \times \frac{S_{FF}}{S_{NF}} = \frac{I_{NF}^B}{I_{FF}^B} \times \frac{S_{FF}}{S_{NF}}.$$

If there is no near field enhancement on the bubble area, then $I_{NF}^B = 0$ and there is no TEPL

on the bubble, leading to $\mathrm{EF_{In}^B} = 0$. Figure 3.2D shows the graphical representation of this EF by

the *blue shade on tip* indicating the near-field in-plane TEPL mechanism (ii) and by the *small

yellow circle* indicating the enhancement due to the out-of-plane tip-bubble mechanism (iii).

Eq. (5) is obtained after expansion of the following equation shown in Figure 3.2E, which

describes the non-synergistic enhancement factor $\mathrm{EF_{NS}}$, which includes the three mechanisms (i)-

(iii) as the sum of the product of the NF enhancement factors $\mathrm{EF_{In}^{BF}} \times \mathrm{EF_{In}^F}$ and the FF enhancement

factor $\mathrm{EF_{Out}^{BF}}$:

$$\text{EF}_{\text{NS}} = \left(\frac{I_{NF}^B}{I_{NF}^F} - 1\right) \times \frac{I_{NF}^F}{I_{FF}^F} \times \frac{S_{FF}}{S_{NF}} + \left(\frac{I_{FF}^B}{I_{FF}^F} - 1\right).$$

Figure 3.2E shows the graphical representation of this EF by the *large red circle* and *blue shade on bubble* due to the funnelling mechanism (i), *blue shade on tip* indicating the near-field in-plane TEPL mechanism (ii) and by the *small yellow circle* indicating the enhancement due to the out-of-plane tip-bubble mechanism (iii).

Finally, *Eq. (6),* shown in Figure 3.2E, describes the total enhancement factor EF_{Tot}, obtained from the comparison of the FF PL intensities on the bubble (I_{FF}^B) and on the flat area (I_{FF}^F), and the corresponding NF PL signals (I_{NF}^B and I_{NF}^F) multiplied by the surface area scaling factor ($\frac{S_{FF}}{S_{NF}}$) :

$$\text{EF}_{\text{Tot}} = \frac{I_{NF}^B}{I_{FF}^F} \times \frac{S_{FF}}{S_{NF}} + \left(\frac{I_{FF}^B}{I_{FF}^F} - 1\right),$$

which gives Eq. (6). It includes all four mechanisms (i)-(iv). Figure 3.2F shows the graphical representation of this EF by the *large red circle* and *blue shade on bubble* due to the funnelling mechanism (i), *blue shade on tip* indicating the near-field in-plane TEPL mechanism (ii), the *small yellow circle* indicating the enh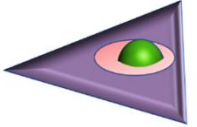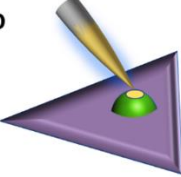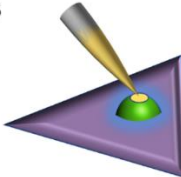a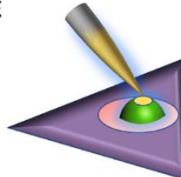ncement due to the out-of-plane tip-bubble mechanism (iii) and by the *red arrow* indicating the synergistic enhancement (or quenching) due to the bubble coupling mechanism (iv).

3.4 Results

Figure 3.3A shows the AFM height image of the TFSI-treated monolayer MoS_2-WS_2 heterostructure, which reveals multiple randomly distributed nanobubbles. Due to the atomic thickness and smooth contrast between the two materials, the heterojunction was not clearly visible. First, we selected two isolated, uncoupled WS_2 and MoS_2 nanobubbles in the vicinity of the junction, separated by ~ 2 µm, and indicated by red crosses in Figure 3.3A. The geometric

31

properties of the two nanobubbles are shown in the zoomed-in AFM height image in Figure 3.3B

and in the AFM height profile in Fig. 3.3C. We label these bubbles as W1 and Mo1, respectively.

The PL measurements with 633 nm excitation allowed for the mapping of the full spectral

band of MoS_2 centered at 675 nm and a part of the spectral band of WS_2 at 635 nm as shown in

the FF PL spectra of WS_2 (Figure 3.3F) and MoS_2 (Figure 3.3G).The chosen locations correspond

to the regions of interest 2-5 in Figure 3.1C. Significant PL enhancement on the bubble as

compared to the flat area was observed in both materials. The corresponding enhancement factors

EF_{Out}^{BF} are shown using Eq. (1) in Table 3.1. The EFs were calculated based on the FF and NF PL

intensities ($I_{FF}^{F}, I_{FF}^{B}, I_{NF}^{F}$, and I_{NF}^{B}) measured on the bubble (B) and flat (F) areas, respectively. Note

that the flat areas were chosen on the side of the bubble away from the junction, to avoid alloying

effects (see discussion below). The FF PL on MoS_2 was enhanced by ~ 4% and on WS_2 by ~ 30%

due to the exciton funnelling mechanism. The larger funnelling efficiency in WS_2 could be due to

its larger dipole moment compared to MoS_2. To further enhance the PL signals and to obtain the

nanoscale resolution, we coupled the laser to the plasmonic Au-coated Ag tip as shown in Figure

3.1A. The TEPL spectra in Figure 3.3D and 3.3E show a significant enhancement of the NF PL

signals on bubbles as compared to the flat areas.

Near-field PL imaging also gives an opportunity to investigate the spatially heterogenous

optical properties of 2D materials. Figure 3.4 shows the NF PL maps of the uncoupled WS_2 (W1)

and MoS_2 (Mo1) nanobubbles obtained by integrating the PL signals in the selected spectral ranges

highlighted in red and green shaded areas in Figures 3.3D and 3.3E. The AFM topographic image

(Figure 3.4B) is correlated with the TEPL maps (Figures 3.4A and 3.4C), revealing a high degree

of PL localization in the vicinity of the bubbles. Note that the smaller particles on the left side of

the WS_2 nanobubbles are not the bubbles but the random particles from oxidation products of
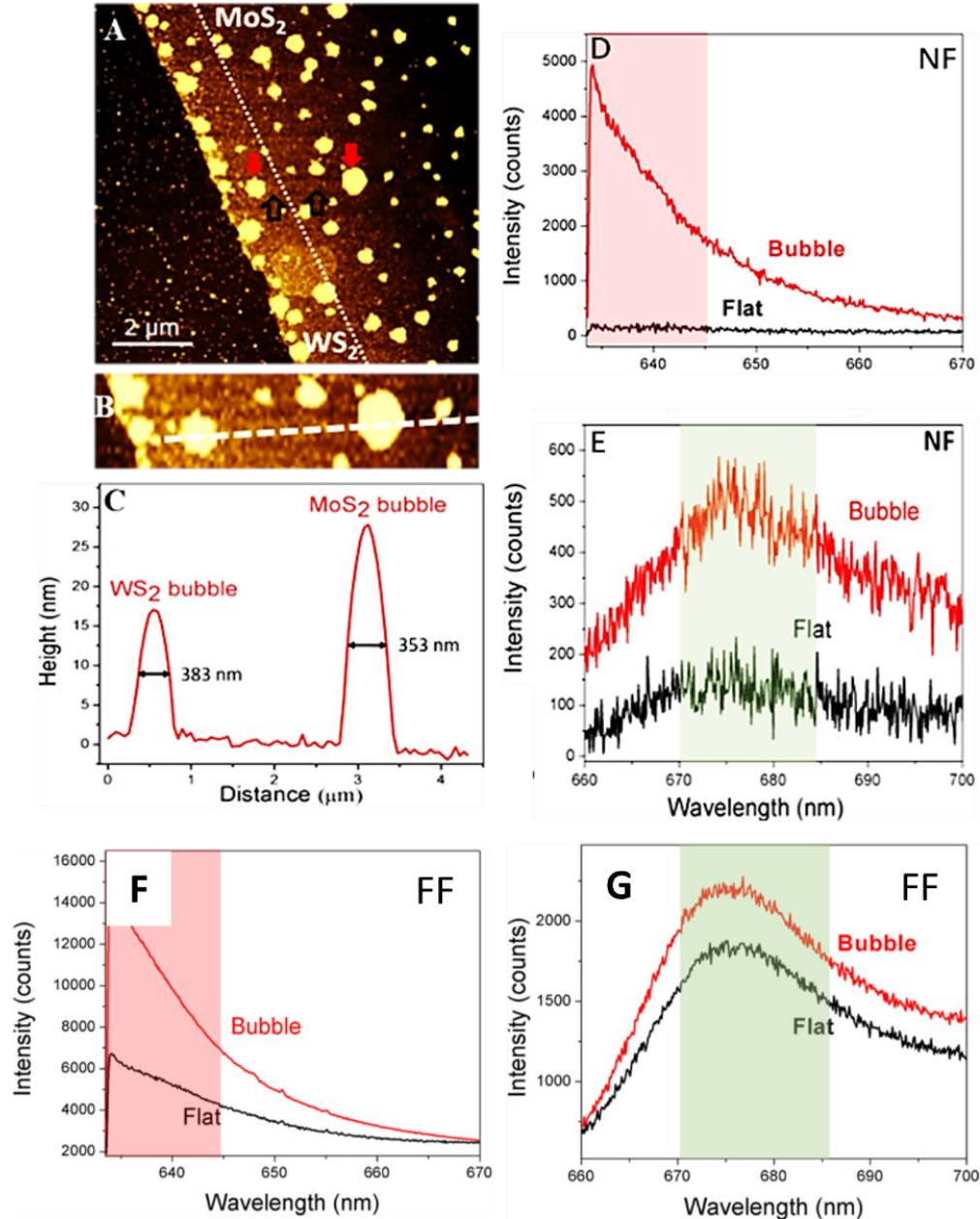
Figure 3.3 Nanobubbles characterization. (A) AFM height image of a monolayer lateral MoS_2-WS_2 heterostructure on a SiO_2/Si substrate. The white dashed line in (A) indicates the junction between MoS_2 and WS_2. (B) AFM height image of the zoomed-in area, which includes WS_2 and MoS_2 nanobubbles marked by red arrows in (A), which are referred to as W1 and Mo1, respectively. (C) AFM height profile of the bubbles, which corresponds to the white dashed line in (B). Near-field (NF) PL spectra on WS_2 (D) and MoS_2 (E). Far-field (FF) PL spectra on the bubble and flat areas on WS_2 (F) and MoS_2 (G) indicated by solid red and open black arrows in (A), respectively.

Figure 3.4 Near-field imaging of uncoupled nanobubbles. WS_2 (A) and MoS2 (C) TEPL images are correlated with the AFM height image (B) of a monolayer lateral MoS_2-WS_2 heterostructure on a SiO_2/Si substrate. The white dotted line in (B) indicates the 2 μm distance between the MoS_2 and WS_2 bubbles. Dashed circles indicate the positions of bubbles. Dashed rectangular areas highlight the asymmetry between the sides of the bubbles closer and further from a junction. Experimental PL enhancement factors (EF) for the WS_2 (D) and MoS_2 (E) bubbles are shown overlapped with AFM height profiles (dotted lines). Theoretical PL EFs for the WS_2 (F) and MoS_2 (G) bubbles are shown overlapped with height profiles (dashed lines).

CVD growth or ambient oxidation that do not show any PL enhancement. We performed FF

Raman and TERS measurements using 532 nm laser excitation to confirm the presence of the 2D

materials and nanobubbles or random particles.

The experimental EF profiles in Figures 3.4D and 3.4E were calculated using Eqs. (3) and (4) for the flat and bubble areas, respectively. As explained in the Enhancement mechanisms section with Figure 3.2, these EFs reflect contributions of the (ii) and (iii) mechanisms that use tip as antenna enhancing NF PL signals without the synergistic contribution of hot electron transfer across the junction. The latter is shown as total enhancement factor, EF_{Tot} in table 3.1. The corresponding raw intensity data are shown in Figure 3.5. below.
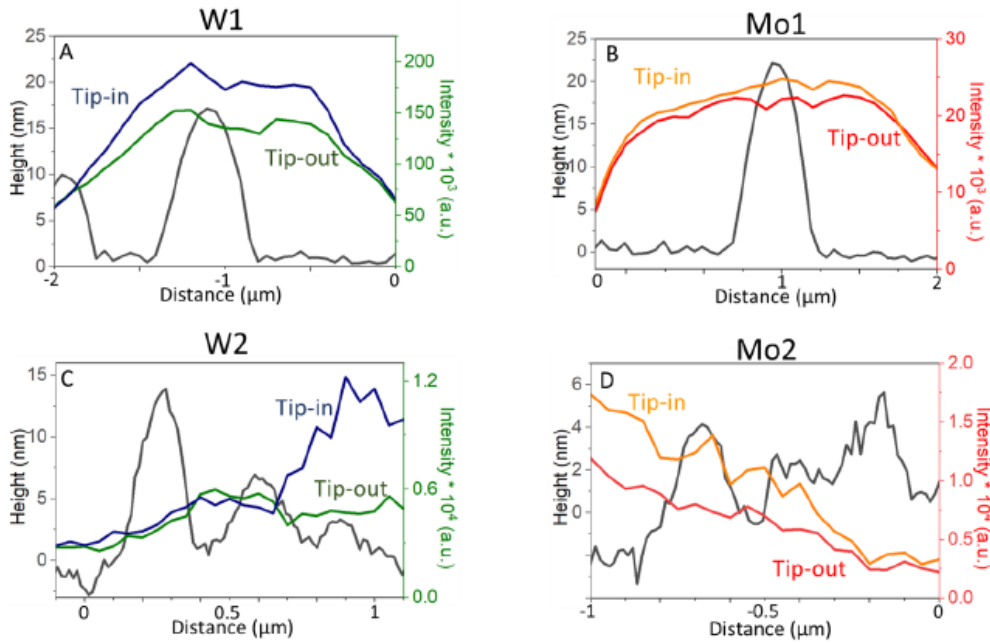
Figure 3.5 Raw intensity data for EF profile calculations. Raw intensity data for EF profile calculations for W1 (A) and Mo1 (B) bubbles in Figures 3.4d and 3.4e, respectively; and for W2 (C) and Mo2 (D) bubbles in Figures 3.5d and 3.5e, respectively, with (Tip-In) and without (Tip-Out) tip-sample contact.

Next we compared these experimental EF profiles with theoretically calculated EFs, shown in Figures. 3.4F and 3.4G. The details of the theoretical model are shown in section 3.8 and are discussed below. Overall, both the experiments and theory showed good agreement, with positive EF values in the bubble areas. This corresponds to the symmetric funnelling shown by dashed lines in Figure 3.1A. The small asymmetry observed in these profiles is due to the symmetry breaking

effect of the junction. It does not lead to negative EF values, indicative of the coupling, as shown below.

To investigate coupling, we performed near-field PL imaging of another pair of the coupled WS_2 (W2) and MoS_2 (Mo2) nanobubbles separated by a smaller distance (~ 760 nm) across the junction (Figure. 3.6). The AFM topographic image (Figure 3.6B) is correlated with the TEPL maps (Figures. 3.6A and 3.6C), revealing a high degree of PL localization in the vicinity of the Mo2 bubble. However, the PL and AFM signals are not well overlapped in the case of the W2 bubble. In fact, the TEPL signal has a negative dip, as shown in the EF profile in Figure. 3.6E. This characteristic negative EF dip is a direct feature of the bubble coupling as described by the theoretical model below and is confirmed in the theoretical EF in Figure. 3.6G. In contrast, both the experimental (Figure 3.6D) and theoretical (Figure 3.6F) EF profiles of Mo2 bubble have positive values and do not show the negative signal on the bubble. This confirms the good agreement between the theoretical model and experiments. Note that the particle at the junction (in AFM image in Figure 3.6B near the dashed white line) is not the bubble but the random particle from oxidation products of CVD growth or ambient oxidation that do not show any PL enhancement.

To distinguish between the bubbles and particles, we performed Kelvin probe force microscopy (KPFM) measurements (Figure 3.7). We measured both the capacitance gradient and contact potential difference (CPD) signals, which both showed significant differences and were able to clearly distinguish between the particles and bubbles. The nature of the capacitance difference is the different chemical composition of the particles and bubbles. The capacitance gradient correlates well with the CPD signals under optical excitation. The basis for the CPD sensitivity is the different response of bubbles and particles to light. We measured CPD with

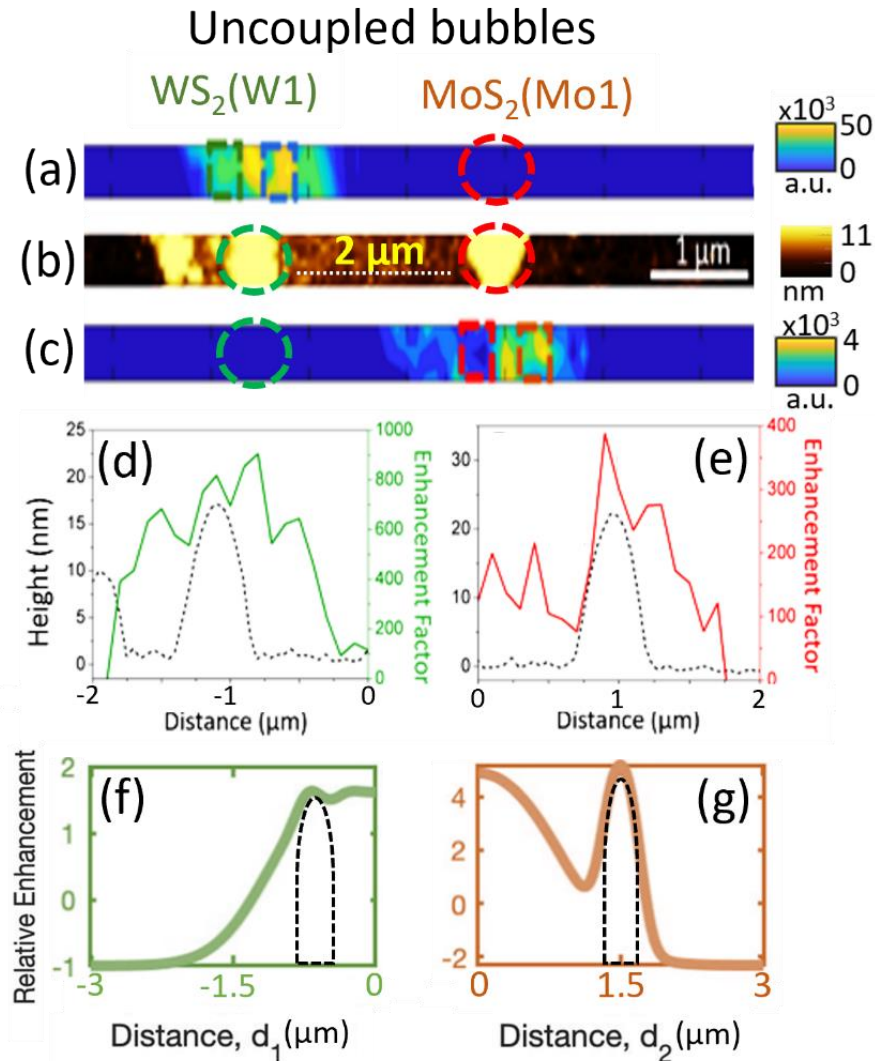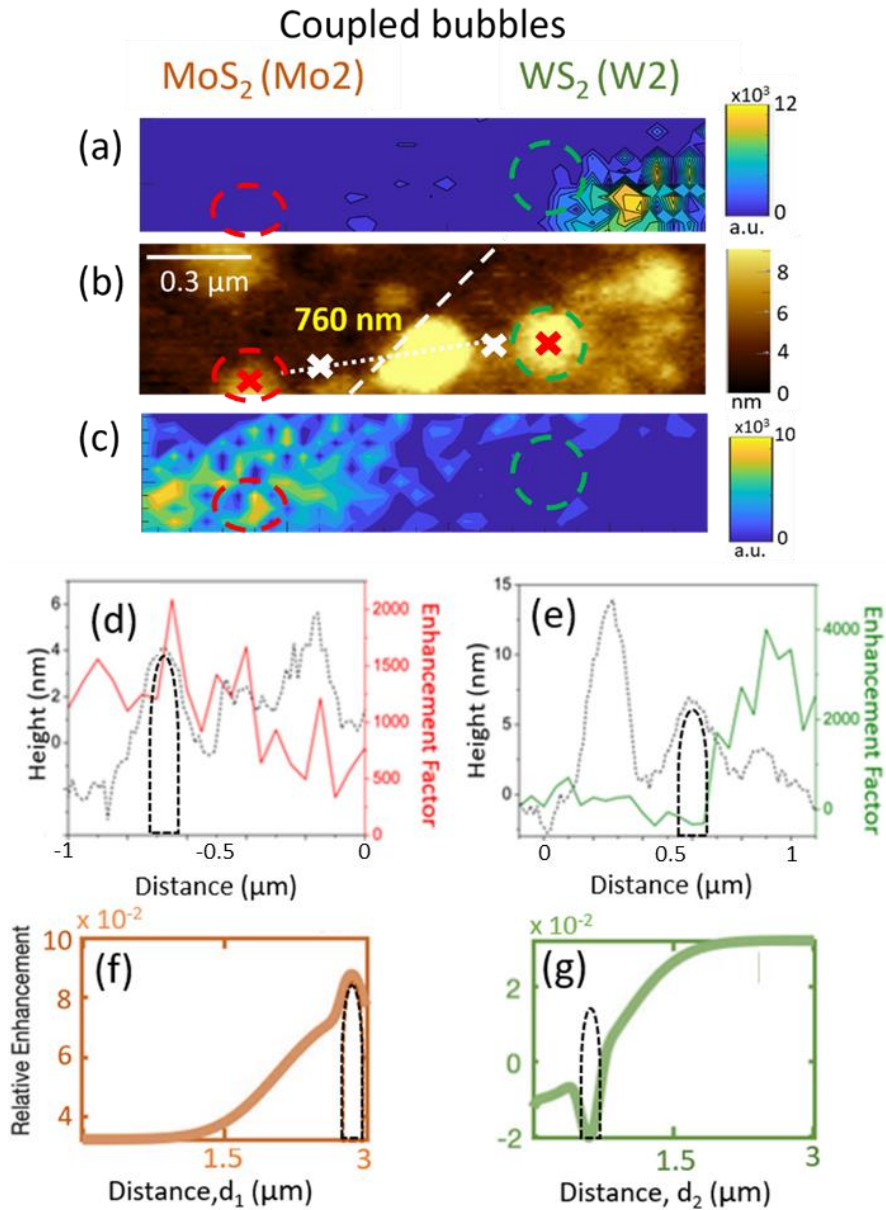Figure 3.6 Near-field imaging of coupled nanobubbles. WS$_2$ (A) and MoS$_2$ (C) TEPL images are correlated with the AFM height image (B) of a monolayer lateral MoS$_2$-WS2 heterostructure on a SiO2/Si substrate. The white dotted line in (B) indicates the 760 nm distance between the MoS$_2$ and WS$_2$ bubbles. White dashed line shows the junction. Dashed circles indicate the positions of bubbles. Experimental PL enhancement factors (EF) for the MoS$_2$ (D) and WS$_2$ (E) bubbles are shown overlapped with AFM height profiles (dotted lines). Theoretical PL EFs for the MoS$_2$ (F) and WS$_2$ (G) bubbles are shown overlapped with height profiles (dashed lines).

(Figures 3.7b. and f) and without (Figures 3.7 d and h) laser excitation. Bubbles are sensitive to

resonant optical excitation, generating excitons and free carriers which significantly modify the

37

CPD signal. However, the particles are not resonant and, therefore, are insensitive to the light. The corresponding CPD signals from the particles are not significantly modified and form dips in the CPD profiles, which are distinguishable from the bubbles, which do not form dips. Other small particles at the edge of the flake show similar dips (indicated by a blue arrow in Figure. 3.7).

The EF values for the uncoupled (W1 and Mo1) and coupled (W2 and Mo2) nanobubbles are presented in Table 3.1.
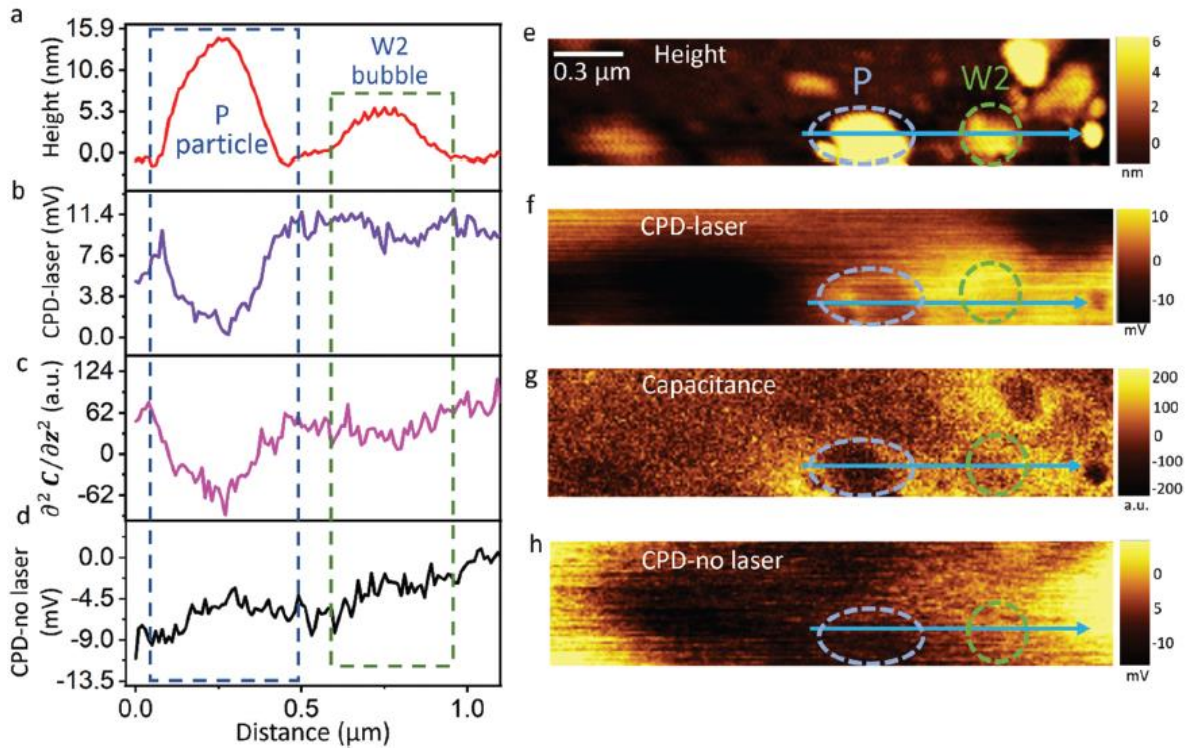
Figure 3.7 Kelvin probe force microscopy (KPFM) of bubbles and particles. (a) AFM height profile that corresponds to the blue arrow line in height map (e). (b) Contact potential difference (CPD) profile that corresponds to the line in CPD map (f), both of which were obtained with ~0.1 mW illumination with 532 nm laser. (c) Capacitance gradient profile that corresponds to the capacitance gradient map (g). (d) CPD profile that corresponds to the line in CPD map (h), both of which were obtained without laser illumination. Blue ellipse and green circle highlight the particle and WS_2 (W2) bubble, respectively.

Table 3.1 Enhancement factors (EF) for the MoS_2 and WS_2 parts of the monolayer lateral heterostructure on bubble (B) and flat (F) areas with (In) and without (Out) plasmonic tip. The EF values were calculated using Eqs. (1) - (6) described above for the uncoupled (W1 and Mo1) and coupled (W2 and Mo2) nanobubbles.

Enhancement Factor	Mechanism				WS_2 (W1)	MoS_2 (Mo1)	WS_2 (W2)	MoS_2 (Mo2)
	(i)	(ii)	(iii)	(iv)				
EF_{Out}^{BF}	x				0.3	0.04	0.17	-0.25
EF_{In}^{BF}	x		x		0.7	1.5	-1.11	-0.26
EF_{In}^{F}		x			559	118	3138	1540
EF_{In}^{B}		x	x		726	284	-273	1520
EF_{NS}	x	x	x		382	176	-3457	-404
EF_{Tot}	x	x	x	x	941	294	-319	1136

3.5 Theoretical Model

We developed a theoretical model to describe the tip-sample distance dependence of the MoS_2 and WS_2 materials as well as the coupled MoS_2 and WS_2 nanobubbles based on the combination of our previous models of $MoSe_2$-WSe_2[124] and MoS_2-WS_2[125] heterostructures without nanobubbles.

Figure 3.8A shows the theoretical model that we developed to describe the tip-sample distance dependence of the MoS_2-WS_2 heterostructure as three-level systems based on our previous model of TEPL in $MoSe_2$-WSe_2 heterostructures[124]. The PL signal of MoS_2 is proportional to the population of exciton state $|X\rangle$, which is coupled to a higher state $|X^0\rangle$ and the ground state $|g\rangle$. The rate equations for the corresponding state populations N_X, N_{X0} and N_g are given by

$$\frac{dN_g}{dt} = -\Gamma_p(d)N_g + \frac{N_X}{\tau_X}, \tag{1}$$

$$\frac{dN_X}{dt} = \alpha N_{X0} - \frac{N_X}{\tau_x}, \qquad (2)$$

$$N_g + N_X + N_{X0} = 1, \qquad (3)$$

where α is the $|X\rangle$ exciton generation rate. The tip-sample distance dependent near-field excitation rate is given by[114,124]

$$\Gamma_p(d) = \begin{cases} A\left(1 - \frac{B}{(R+d-c)^3}\right)^{-2}, & \text{for } d > 0.36 \text{ nm} \\ 1 - e^{-\frac{d-c}{d_p}}, & \text{for } c < d < 0.36 \text{ nm} \end{cases}, \qquad (4)$$

where A is a constant for continuity of the piecewise function, $B = 5028$ characterizes the probe's material properties[114,124], $R = 20$ nm is the radius of curvature of the tip apex, $c = 0.17$ nm is the ohmic conduction distance, and $d_p = 0.02$ nm is the average quantum tunneling distance[124]. The
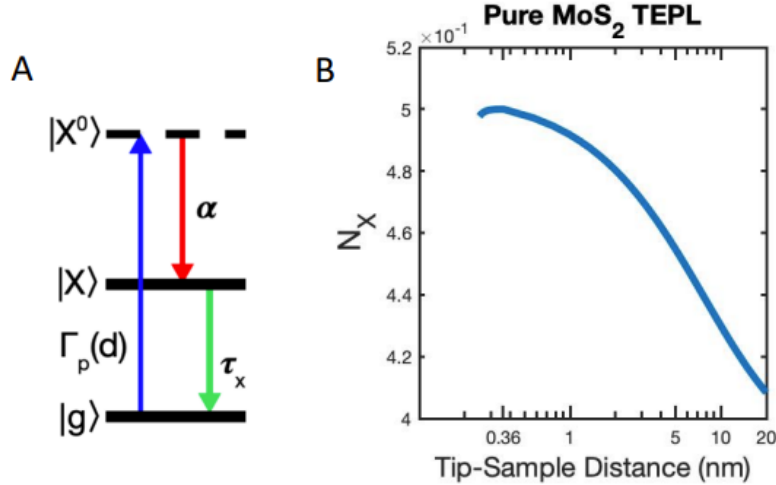
Figure 3.8 Phenomenological model diagram of exciton dynamics in uncoupled pure MoS$_2$ and WS$_2$ materials. (B) Simulated tip-sample distance dependance of exciton population in pure MoS$_2$.

exciton generation rate $\alpha = 1 \, ps^{-1}$ and the average exciton lifetime $\tau_X = 2 \, ps$ were used. The tip-sample distance dependence of the N_X population in steady state using these parameters is shown in Figure. 3.8 B.

3.5.1 TEPL of Coupled MoS$_2$ and WS$_2$

The PL signals of the coupled MoS$_2$ and WS$_2$ are proportional to the populations of exciton states $|X\rangle$ and $|Y\rangle$, respectively, which are coupled to the ground state $|g\rangle$, and the corresponding higher states $|X^0\rangle$ and $|Y^0\rangle$. The rate equations for the state populations N_g, N_{X0}, N_{Y0}, N_X, and N_Y are given by

$$\frac{dN_g}{dt} = -2\Gamma_p(d)N_g + \frac{N_X}{\tau_X} + \frac{N_Y}{\tau_Y}, \tag{5}$$

$$\frac{dN_X}{dt} = \alpha N_{X0} - \frac{N_X}{\tau_x} + \gamma_1\Gamma_p(d)N_Y, \tag{6}$$

$$\frac{dN_Y}{dt} = \beta N_{Y0} - \frac{N_Y}{\tau_Y} - \gamma_1\Gamma_p(d)N_Y, \tag{7}$$

$$\frac{dN_{X0}}{dt} = \Gamma_p(d)N_g - \alpha N_{X0} - \gamma_2\Gamma_p(d)N_{X0}, \tag{8}$$

$$N_g + N_X + N_Y + N_{X0} + N_{Y0} = 1, \tag{9}$$

where α and β are exciton $|X\rangle$ and $|Y\rangle$ generation rates, τ_X and τ_Y are the average exciton lifetimes, and $\Gamma_p(d)$ is the tip-sample distance dependent near-field excitation rate, described above. Similar simulation parameters were used for $\Gamma_p(d)$ as for the uncoupled model. The coupling between the states $|X\rangle$ and $|Y\rangle$ via the junction was modeled by the photoinduced charge transfer rate $\gamma_1\Gamma_p(d)$ (purple arrow in Figure 3.9A) as previously described for the nonresonant TEPL of MoSe$_2$-WSe$_2$[124]. This leads to an increasing N_X for the decreasing tip-sample distance as shown in Figure. 3.9B. Similarly, the coupling between the states $|X^0\rangle$ and $|Y^0\rangle$ via the junction was modeled by the photoinduced charge transfer rate $\gamma_2\Gamma_p(d)$ (blue arrow in Figure 3.9A) as previously described for the resonant TEPL of MoS$_2$-WS$_2$[125]. This leads to an increasing N_Y for the decreasing tip-sample distance (not shown) similar to N_X. This model agrees with our experimental observations for the bubble-junction coupling. For both bubbles coupled to each other via the junction we set

$\gamma_2 = 0$ and use $\gamma_1(d_1 = 0) = 0.278$ instead of γ_1' because the effects from the presence of the

bubbles at the junction cannot be ignored. This leads to quenching of N_Y (Figure 3.9C).
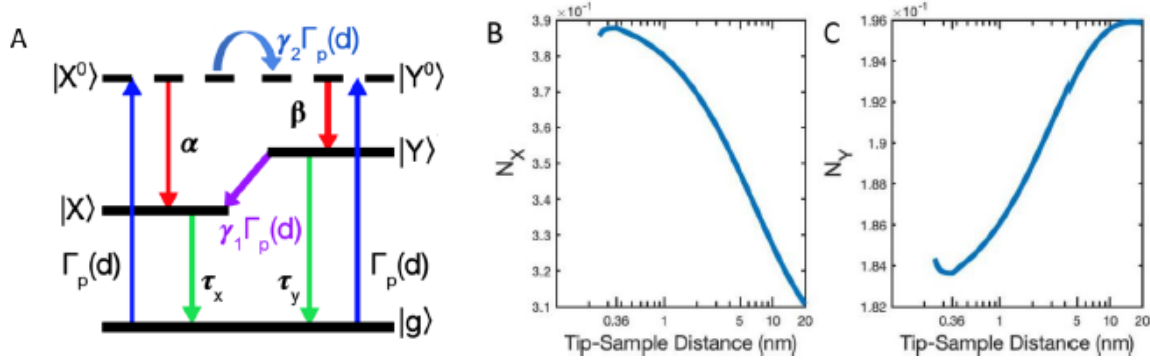
Figure 3.9 Phenomenological model diagram of exciton dynamics in coupled MoS₂ and WS₂
nanobubbles near junction. Simulated tip sample distance dependance of exciton population in
coupled MoS₂ (B) and WS₂ (C) nanobubbles.

The lateral spatial dependence of the effect of the junction width and nanobubbles were

described using the following forms of the charge transfer rates

$$\gamma_1(d_1) = \gamma_1' \left(e^{-\frac{1}{2}(\frac{d_1}{\sigma})^2} + e^{-\frac{1}{2}(\frac{d_1-r_1}{\sigma_b})^2} \right),$$ (10)

and

$$\gamma_2(d_2) = \gamma_2' \left(e^{-\frac{1}{2}(\frac{d_2}{\sigma})^2} + e^{-\frac{1}{2}(\frac{d_2-r_2}{\sigma_b})^2} \right),$$ (11)

which include the effects of charge funneling due to the shapes of the junction and bubbles

approximated by Gaussian functions with the values of the parameters based on the experimental

observations. Here, we consider the *bubble-junction coupling* case when either the MoS₂ or WS₂

bubbles are in the vicinity of the junction and are, therefore, coupled to the flat areas of the

respective other material. The coupled MoS₂ bubble corresponds to the nonresonant TEPL model

of the MoSe₂-WSe₂ flat heterostructure[124] and its lateral spatial dependence is described by the d_1

coordinate in the γ_1 rate function in Eq. (10). Similarly, the coupled WS₂ bubble corresponds to

the resonant TEPL model of the MoS$_2$-WS$_2$ heterostructure[125] and its lateral spatial dependence is described by the d_2 coordinate in the γ_2 rate function in Eq. (11) due to the charge tunneling effect. Note that in our model we always assume the junction at the center of the coordinate system with $d_1 = d_2 = 0$, while the bubble is assumed to be on the right side of the junction.

The first term in the left sides of Eqs. (10) and (11) describes the shape of the junction with the width of $\sigma = 667\ nm$ based on the experimental TEPL measurements of the junction without bubbles. This width corresponds to the smooth MoS$_2$->WS$_2$ junction, that was obtained during the CVD growth of the 2D heterostructures as previously described[92]. This junction width results in the negligible effects ~ 1 µm away from the junction, and approximately corresponds to the far-field spatial resolution of our measurements.

The second term in the left sides of Eqs. (10) and (11) describes the shape of the nanobubbles with the positions (r$_1$ and r$_2$) and widths (σ_b) obtained from the experiments. TEPL enhancement factors were simulated by solving Eqs. (5) - (11) in steady state as relative enhancements ΔN of MoS$_2$ (N$_X$) and WS$_2$ (N$_Y$) populations equal to the differences between the corresponding near-field (NF) and far-field (FF) signals at 0.36 nm and 20 nm tip-sample distance, respectively: ΔN$_X$ = N$_X$(0.36nm) - N$_X$(20nm) and ΔN$_Y$ = N$_Y$(0.36nm) − N$_Y$(20nm). The exciton generation rates were $\alpha = \beta = 1\ ps^{-1}$ and the exciton lifetimes were $\tau_X = \tau_Y = 2\ ps$. The coefficients γ_1' and γ_2' were set equal to 0.25 and 1, respectively.

3.6 Discussion

The enhancement of the FF PL signals without the tip due to the mechanism (i) is described by EF_{Out}^{BF} represents spatially averaged information over the bubble area due to the limited FF spatial resolution. The NF analogue of Eq. (1) is given by Eq. (2) for the enhancement factor EF_{In}^{BF}, which provides an improved description of funnelling with a higher spatial resolution. It shows

43

larger EF_{In}^{BF} values compared to EF_{Out}^{BF} for both uncoupled bubbles W1 and Mo1 (Table 3.1). Also, as expected, the EF_{In}^{BF} value of the coupled W2 bubble is smaller compared to EF_{Out}^{BF} value because of the more pronounced negative quenching signal, which gets averaged out in the far-field case of EF_{Out}^{BF}. Also, EF_{In}^{BF} of W2 bubble is smaller than -1, because of the negative I_{NF}^{B} signal of WS_2 bubble due to the coupling to MoS_2 bubble. However, both mechanisms (i) and (iii) contribute to EF_{In}^{BF}. Therefore, further analysis of other EFs is needed to separate these contributions. Note that the small negative values of the EF_{Out}^{BF} and EF_{In}^{BF} of Mo2 bubble are due to the possible allying effect and the uneven distribution of MoS_2 material close to the junction. These values may be ignored and the positive value of the total enhancement factor for Mo2 bubble still support the coupling mechanism, as shown below.

To understand the effects of other mechanisms, we investigate the EFs given by Eqs. (3)-(6). For example, the values of EF_{In}^{F} and EF_{In}^{B} in Eqs. (3) and (4), respectively, correspond to the tip enhancement on flat and bubble areas. EF_{In}^{F} is the conventional TEPL enhancement factor determined by the in-plane tip enhancement mechanisms (ii). EF_{In}^{B} is the analogous TEPL enhancement factor on the bubble and is determined by both the in-plane (ii) and out-of-plane (iii) mechanisms. The out-of-plane mechanism (iii) is due to the PL enhancement of the non-flat part of the 2D material (bubble) by the polarization component of the near-field along the tip axis[114,121]. These EFs are normalized by the areas for the near-field (S_{NF}) and far-field (S_{FF}) excitation spots, where $S_{FF} = \pi R_{FF}^2$ with the FF excitation spot radius R_{FF}=500 nm and $S_{NF} = \pi R_{NF}^2$ with NF spot size equal to the tip apex radius R_{NF}=10 nm. Surprisingly, the value of EF_{In}^{F} on WS_2 is larger than on MoS_2 for both the flat areas near the uncoupled and coupled bubbles (Table 3.1), which could be explained due to the stronger light-matter coupling and slight p-doping nature of WS_2. However, the value of EF_{In}^{B} on WS_2 is negative for the coupled W2 bubble and is positive for the

uncoupled W1 bubble, indicating the PL intensity quenching due to the coupling to the MoS_2 bubble as expected based on the schematic in Figure 3.1A and the theoretical model. These EFs are influenced by the mechanisms (ii) and (iii), in which the tip is used as an antenna probing the bubble coupling by funnelling. Here the tip is used as a nanoscale reporter and does not contribute to the coupling. The combination of the three mechanisms (i)-(iii), where tip only performs the passive role of a reporter is presented in the non-synergistic EF_{NS} shown in Table 3.1. It shows the coupling of nanobubbles via the junction without the active influence by the tip. However, the tip may also contribute to the bubble coupling effect, for example, via hot electron injection into the WS_2 flat area and subsequent hot electron transfer to WS_2 bubble and then to MoS_2 bubble. This additional flat-bubble-tip-bubble coupling effect may be observed as synergistic contribution to the total enhancement factor, EF_{Tot}, which includes an additional synergistic mechanism (iv), as shown in Eq. (6) in Table 3.1. It is schematically represented by the four solid arrows in Figure 3.1A. The subtraction of I_{NF}^F in the numerator in Eq. (5), compared Eq. (6), explains the synergistic effect in EF_{Tot}, since subtracting I_{NF}^F from the numerator eliminates the "near-field flat-to-bubble" coupling effects. As a result, the final EF_{Tot} of the coupled WS_2 bubble is still negative, and both the uncoupled WS_2 and MoS_2, as well as the coupled MoS_2 bubbles all have positive values. All four mechanisms are included in the combined synergistic EF_{Tot}, which provides direct evidence of coupling with and without the contributions of the plasmonic tip. Thus, our discovered additional tip-induced bubble coupling mechanism could be used in developing new active nanophotonic devices.

3.7 Conclusion

In summary, we have studied the coupling of MoS_2 and WS_2 nanobubbles by the plasmonic antenna tip and a heterojunction using tip-enhanced near-field imaging. The observed quenching

of the PL signals provides experimental and theoretical evidence for the coupling. The work provides a step towards developing new coupled quantum emitters based on 2D nanobubbles are promising candidates for quantum information and communication applications.

Chapter 4: Picoscale Control of Quantum Plasmonic Photoluminescence at 2D Lateral Heterojunction[iii]

4.1 Introduction

Two-dimensional (2D) materials and heterostructures have recently gained wide attention due to potential applications in optoelectronic devices such as atomically thin p-n junctions and phototransistors. However, the optical properties of the heterojunction have not been properly characterized due to the limited spatial resolution, requiring nano-optical characterization beyond the diffraction limit. Here, we investigate the lateral monolayer MoS_2-WS_2 heterostructure using tip-enhanced photoluminescence (TEPL) spectroscopy on a non-metallic substrate with picoscale tip-sample distance control. By placing a plasmonic Au-coated Ag tip at the heterojunction, we observed more than three orders of magnitude photoluminescence (PL) enhancement due to the classical near-field mechanism and charge transfer across the junction. The sub-Angstrom precision of the distance-dependent TEPL measurements allowed for investigating the classical and quantum tunneling regimes above and below the ~320 pm tip-sample distance, respectively. Quantum plasmonic effects usually limit the maximum signal enhancement due to the near-field depletion at the tip. We demonstrate a more complex behavior at the 2D lateral heterojunction, where tunneling of hot electrons leads to the quenching of the PL of WS_2, while simultaneously increasing the PL of MoS_2. Our simulations show agreement with the experiments, revealing the

---

[iii] This chapter was uploaded online on arXiv., Reference[125] (Withers, Z. H. et al. Picoscale control of quantum plasmonic photoluminescence enhancement at 2D lateral heterojunction. arXiv preprint arXiv:2001.10138 (2020)). Permission is included in Appendix F: Copyright Permission for Chapter 4.

range of parameters and enhancement factors corresponding to various regimes. The controllable photoresponse of the lateral junction can be used in novel nanodevices.

4.2 Results

Figure 4.1a illustrates the picoscale controlled tip-sample distance dependent TEPL measurements on a monolayer lateral MoS_2-WS_2 heterostructure using three different tip locations on the MoS_2 (left), WS_2 (right) and center of the heterojunction (middle). The measured TEPL signals with the tip-sample distance, d < 20 nm, are referred to as the classical regime. As the metallic tip reaches the quantum regime, there is a charge transfer from WS_2 to MoS_2 across the heterojunction which is represented by purple arrow (Γp *(d)*). This charge transfer process across the heterojunction is theoretically described in electron-exciton schematic diagram of the MoS_2-WS_2 heterostructure in the TEPL measurements in figure 4.1b. The hot electrons are injected with the rate of $G_{HEI}\Gamma_{CT}(d)$ occurs from the plasmonic tip to a virtual state within the conduction band of the semiconductor. These hot electrons then relax by forming excitons at rates α or β in MoS_2 and WS_2, respectively, or through nonradiative decay channels at a rate of R_{HEI} followed by exciton relaxation at rates τx and τy in MoS_2 and WS_2, respectively. The transfer of exciton transfer occurs from WS_2 to MoS_2 at the heterojunction and is assumed to be proportional to the near field optical excitation rate of electrons from the ground state, Γp (d). The tip-sample measurements were done on 9 spots, with 4 spots on WS_2 and 4 on MoS_2, and 1 spot on heterojunction. Spot 3 is on the heterojunction. For the sake of data analysis, we chose spots from 1 to 5, since spots 6, 7, 8 and 9 were showing the same qualitative analysis. The distance between spot 2 and spot 3 is 245.9 nm, distance between spot 3 and spot 1 is 318.3 nm, distance between spot 3 and spot 4 is 238 nm and the distance between spot 3 and spot 5 is 469 nm. Since, the laser excitation is at 660 nm, and the

laser filter blocks emitted light before 665 nm, only a small portion of WS$_2$ PL is observed as shown in the green mesh in figure 4.1c. Similarly, red mesh shows the PL area of MoS$_2$.
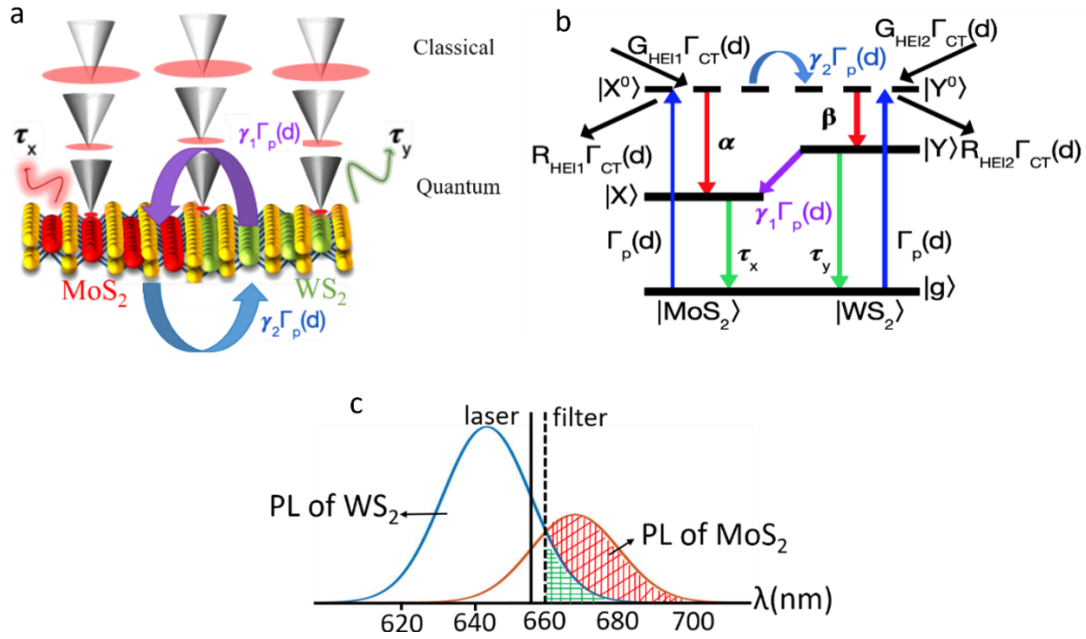
Figure 4.1 Lateral MoS$_2$-WS$_2$ heterostructure. (a) Sketch of the controlled tip-sample distance dependence measurements in the classical and quantum regimes. A 660 nm linearly polarized laser is on the apex of the Au-coated Ag plasmonic tip and the emitted PL signals are detected when the tip-sample distance is in the classical (d>0.36 nm) and in the quantum regime (d<0.36 nm). (b) Schematic state diagram at the junction of the 2D lateral heterojunction in tip-enhanced photoluminescence (TEPL) experiments. Hot electron injection (HEI) occurs from the plasmonic tip to the semiconductor. (c) Sketch of the PL peaks of WS$_2$ and MoS$_2$ and the laser. The green shaded area and red shaded area show the PL of WS$_2$ and MoS$_2$, respectively.

The 2D contour maps in figures 4.2a-e show TEPL intensity with respect to controlled tip-sample distance measurements as a function of wavelength on five spots (S1 to S5). The picometer tip-sample distance resolution has been previously developed[126] and utilized in recent experiments[124,126] by equating the normal force on the AFM tip with the Lennard Jones force. Here we use A=2.2 x 10^{-7} in the repulsive term of the Lennard Jones force, F=A/r^{13}, and a spring constant of 2.8Nm^{-1} for the AFM tip. . The tip-sample distance was controlled from 20 nm to 0.36 nm to observe the effects of classical plasmonics. At 0.36 nm, the subnanometer gap between the metallic

tip and the sample leads to directional electron tunneling towards the sample and all the plasmonic

effects at this distance is quantum mechanically assisted.
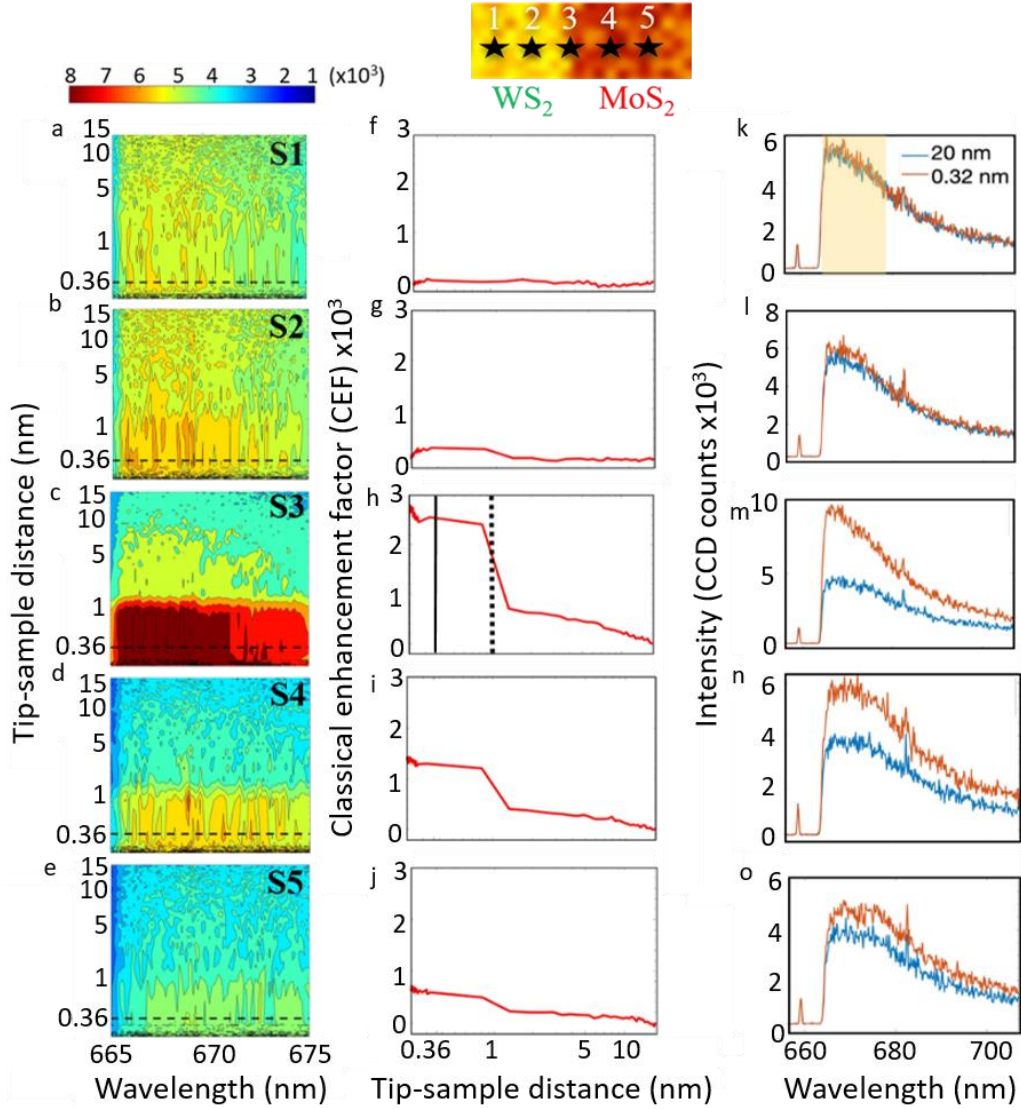
Figure 4.2 Tip-sample distance dependance TEPL measurements. Figure 4.2a-e shows 2D contour plots showing tip-sample distance measurements with $0.2nm \leq d \leq 20nm$ as a function of wavelength on 5 spots. 4.2a-b are the spots on the WS_2 side of heterostructure, very close to junction. As the tip goes from 20 nm to 0.36 nm, no significant change in intensities is observed in spot 1 and spot 2 as observed by 4.2a, b and their corresponding enhancement factors 4.2f and g. At spot 3, a significant enhancement is observed in PL is observed (4.2c and h) as the tip goes at 1nm distance from the sample due to the hot electron enhancement mechanism in MoS_2. Spot 4 and spot 5 show slight enhancement as we go from heterojunction towards MoS_2 as seen in 4.2d-e. The TEPL intensity spectra at all 5 spots are also shown from k-o in 4.2d-e. The TEPL intensity spectra at all 5 spots are also shown from k-o.

At spots 1 and 2, due to the laser filter at 665 nm, only a small, emitted shoulder PL peak of WS_2 is observed as shown in figure 1d reason for very less change in PL intensity from classical to quantum regime. This can be verified by observing the intensity spectra in figure 4.2k at d = 20nm (classical) and d = 0.32 nm (quantum).

As you move towards the heterojunction, a small enhancement is shown from 1 nm to 0.36 nm. However, at the heterojunction, as shown by spot 3, the enhancement in the PL intensity is observed from 20 nm to 1 nm and a much significant enhancement is observed from 1 nm to 0.36 nm. Previously, not many studies were done to observe the effect of PL at d = 1nm, at which tip snaps to contact with the sample. The enhancement at spot 3 can be attributed to the accumulation of hot electrons injected by the tip in MoS_2 when the tip-sample distance reduces from 20 nm to 0.36 nm leading to overall PL enhancement. At spot 4 and spot 5, as shown in figures 4.2d, 4.2n, 4.2e and 4.2o, the enhancement of PL intensity decreases from classical to quantum regime as we go away from the junction. The enhancement factor as a function of tip-sample distance have been calculated and plotted for all the 5 spots. In the classical regime, the furthest data point was the far field reference point. All the data was normalized to this data point and then 1 was subtracted from each entry in the data set. Then, the data was multiplied by 2500 because that is the ratio between the area in the far field with the area in the near field. If X is the data set and x1 is the far field reference point,

$$EF = (\frac{X}{X_1} - 1) \times 2500$$

To analyze the enhancements at these spots quantitively, we made a table for classical enhancement factor (CEF) for 5 spots at d= 1nm, d=0.32 nm and for quantum enhancement factor (QEF) at d =0.20 nm. The enhancement factor plots, and the table clearly shows a huge PL

enhancement of about 624 at spot 3 in classical regime with a much higher increase in the PL intensity at d=0.32 nm of about 2550.

In the quantum plasmonic regime, when the tip reaches at a distance of 0.36 nm, which is the vdW contact, directional electron tunneling takes place from the plasmonic tip to the sample. Previously, it has been shown, even in the absence of metal-metal contacts, quenching of WSe_2 PL has been observed at the heterojunction. We show the similar effect of PL quenching of WS_2 on SiO_2/Si substrate at the heterojunction. The Figures 4.3a, 4.3f for spot 1 and 4.3b, 4.3g for spot 2, shows this quenching effect.

The PL quenching of WS_2 is stronger at Spot 2 because of its proximity to the heterojunction as shown from the enhancement factor plot in figure 4.2g. The enhancement factor plots were calculated the same way as for classical regime, except the normalization factor multiplied, was calculated using ratio of area of the metallic tip to the area of a gold atom giving the value as 12484. At d=0.36 nm, the accumulation of the hot electrons coming from the tip on WS_2 side of the heterojunction, is decreased since there is a charge transfer from WS_2 to MoS_2 across the depletion region.

Table 4.1 Summary of Classical (CEF) and Quantum enhancement factor (QEF) values at contact, 0.32 nm and 0.20 nm for spots 1-5.

Spots	CEF (contact)	CEF (O.32nm)	QEF (0.20 nm)
S1	35	16	-234
S2	14	219	-966
S3	624	2554	445
S4	376	1294	362
S5	202	587	259

At spot 1 and spot 2, due to the charge transfer from WS_2 to MoS_2 and due to depletion region, quenching in WS_2 is observed as seen in a-b and their corresponding enhancement factors f-g. On spot 3, a huge enhancement in TEPL on the heterojunction is observed in MoS_2 due to the

hot electron injection from the plasmonic tip. As we move away from the junction towards pure

MoS$_2$, a gradual decrease in enhancement is observed as seen in spots 4 and 5.

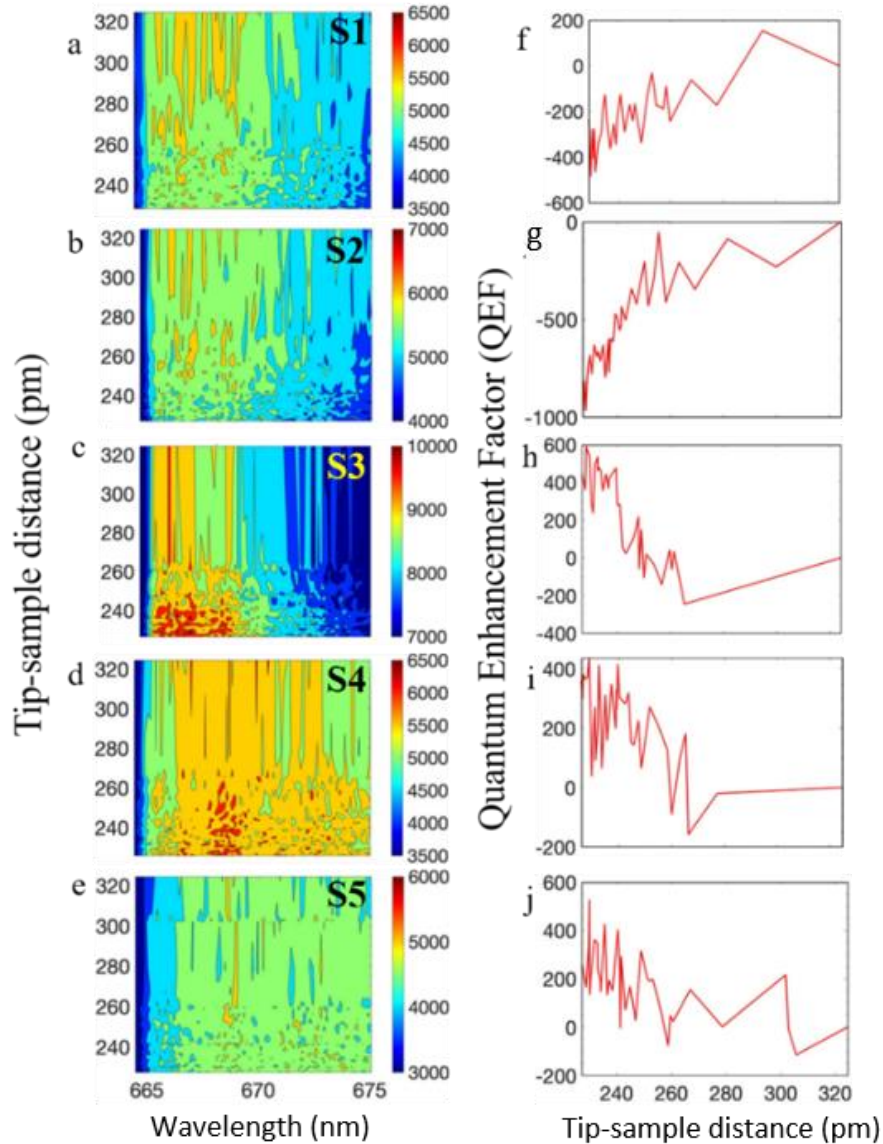Figure 4.3 Tip-sample distance dependance measurements in quantum regime. At the heterojunction the tip-sample distance measurements are done with d <320 pm, referred as quantum plasmonic regime on spots 1 thru 5.

4.3 Theoretical Model

A phenomenological rate equation model is used in order to further understand the

interplay between hot electron injection, electron transfer, and exciton transfer during the

experiment. Figure 4.1b shows the electron-exciton diagram used to model electron excitation and exciton formation near the heterojunction. An initial population, N, of electrons is excited from the ground state, $|g\rangle$, to a virtual state $|X^0\rangle$ or $|Y^0\rangle$, by the plasmonic near field of the AFM tip, which then decays to exciton states $|X\rangle$ or $|Y\rangle$. As a result, the population dynamics can be described by the rate equations:

$$\frac{dN_{X0}}{dt} = \Gamma_p(d)N_g - \alpha N_{X0} - \gamma_2\Gamma_p(d), \tag{1}$$

$$N_{X0} + N_{Y0} + N_X + N_Y + N_g = 1 \tag{2}$$

$$\frac{dN_X}{dt} = \alpha N_{X0} + \gamma_1\Gamma_p(d) - \frac{N_X}{\tau_X}, \tag{3}$$

$$\frac{dN_Y}{dt} = \beta N_{Y0} - \gamma_1\Gamma_p(d) - \frac{N_Y}{\tau_Y} \tag{4}$$

$$\frac{dN_g}{dt} = -2\Gamma_p(d)N_g + \frac{N_X}{\tau_X} + \frac{N_Y}{\tau_Y}. \tag{5}$$

The plasmonic near field pumps electrons (blue arrows) with a rate[127],

$$\Gamma_p(d) = \begin{cases} 1 - e^{-((d-c)/d_p)} & \text{for } c < d < 0.36 \text{ nm} \\ \frac{1}{A_p}\left(1 - \frac{B}{(R+d-c)^3}\right)^2 & \text{for } d > 0.36 \text{ nm} \end{cases}$$

where $d_p = 0.02$ nm is the average quantum coupling distance, $c = 0.17$ nm is the ohmic contact distance, $R = 25$ nm is the radius of the tip apex, A_p ensures continuity, and $B = 5028$ includes the polarizability of the tip[127]. Electrons are assumed to decay with rates $\alpha = 1$ ps^{-1} and $\beta = 15$ ps^{-1} into the exciton states $|X\rangle$ and $|Y\rangle$, respectively (red arrows). Electrons are considered to decay at a higher rate in WS$_2$ since the excitation laser frequency is resonant with the exciton energy of WS$_2$. Then, excitons decay from $|X\rangle$ and $|Y\rangle$, with lifetimes of $\tau_x = \tau_y = 2$ ps^{-1}, respectively[128] (green arrows).

Due to the junction's intrinsic chemical potential difference, excitons transfer from MoS_2 to WS_2 (purple arrow) with a rate $\gamma_1 \Gamma_p(d)$, where γ_1 is the photoinduced exciton transfer coefficient[129]. Lastly, we introduce $\gamma_2 \Gamma_p(d)$ to describe virtual state charge transfer (light blue arrow) from MoS_2 to WS_2. Since electrons decay from $|Y^0\rangle$ at a higher rate than $|X^0\rangle$, virtual state charge transfer ensures the preservation of the detailed balance between the virtual states $|X^0\rangle$ and $|Y^0\rangle$.

Figure 4.4 (a-d) shows simulated TEPL enhancement factors for $\gamma_1 = 0$ (a) and $\gamma_1 = 1$ (b) for several values of the virtual state charge transfer coefficient, γ_2. Figure 4.4d shows how WS_2 enhances at the heterojunction in the classical regime only when virtual state charge transfer is considered in the model, in accordance with Figure 4.2 h, m. In addition, Figure 4.4h shows WS_2 enhances at the heterojunction in the quantum regime with virtual state charge transfer, which agrees with Figure 4.3h. In addition, Figure 4.4f shows quantum regime quenching of TEPL in pure WS_2 and quantum regime enhancement of TEPL in pure MoS_2 Figure 4.4e, which agrees with Figures 4.3f,g and Figure 4.3i,j, respectively.
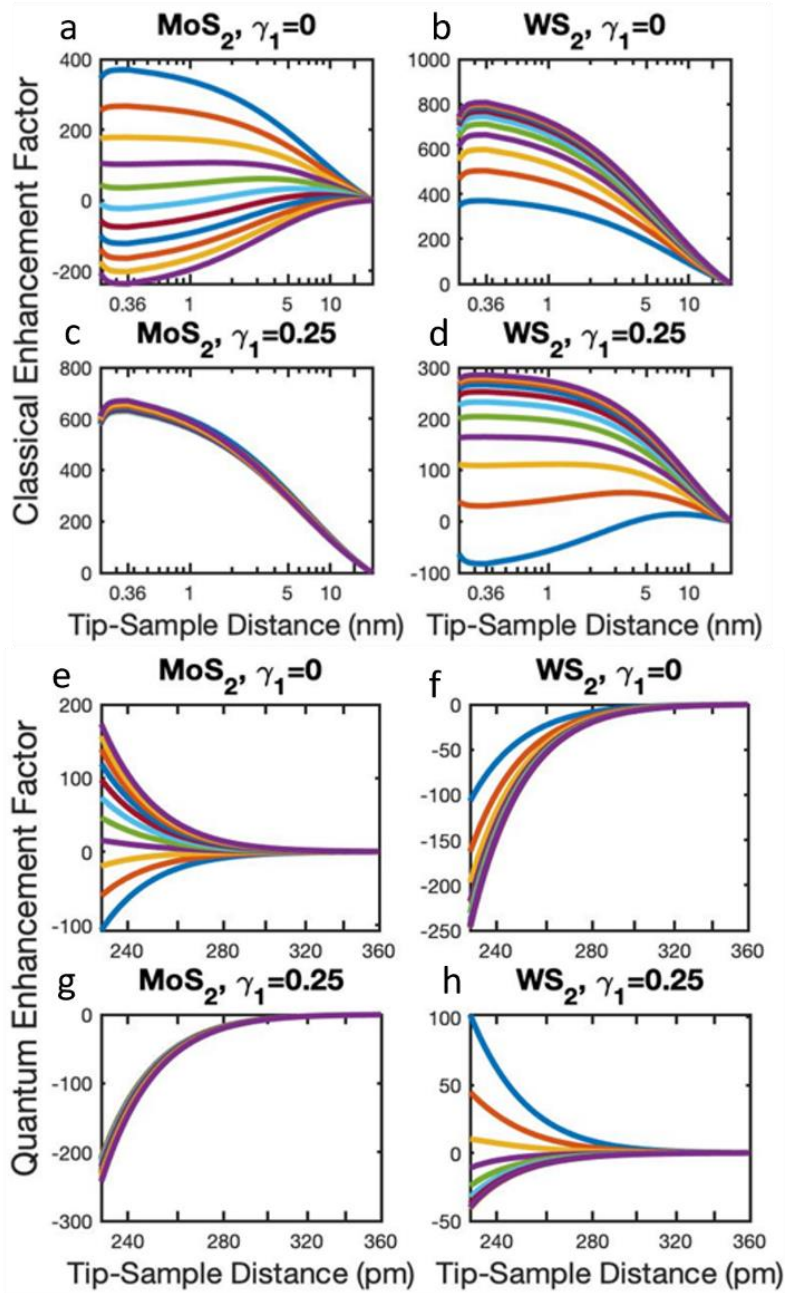
Figure 4.4 Simulated tip-sample distance dependent TEPL at the heterojunction. The exciton charge transfer coefficient, γ_1, equals zero and several values of γ_2 are shown. The case when $\gamma_1 = \gamma_2 = 0$ is for pure materials. In this case, WS_2 quenches and MoS_2 enhances. Simulated tip-sample distance dependence TEPL curves on the heterojunction, $\gamma_1 = 0.25$. Observe, WS_2 enhances in the classical regime due to virtual state charge transfer, $\gamma_2 = 1$, and quenches in its absence, $\gamma_2 = 0$.

Chapter 5: Detection of Bacteriostatic Treatment Using 2D Materials

5.1 Current Live/Dead Bacteria Detection Strategies and their Limitations

Current techniques of bacterial identification require labor demanding culturing techniques that could take several days and/or microscopic investigations and biochemical tests, such as DNA and RNA fingerprints. However, these classical methods of analysis possess major disadvantages, including prohibitive time consumption, difficulties in sample preparation, and other technological limitations[130]. Cell staining techniques introduce multiple limitations leading to the inability of the bacterial strain determination, and must be performed in conjunction with additional procedures to produce viable results[131]. Moreover, side reactions caused by the dyes and bacterial cell wall interactions may lead to false data acquisition[132]. For example, methods based on the flow immunofluorescence are restricted to particular strains, thus providing insufficient means to attain comprehensive screening of multiple bacterial characteristics[131].

Especially, if the bacteria is treated with the bacteriostatic antibiotic drug chloramphenicol, which interferes with bacterial protein synthesis via inhibition of the function of ribosomes[133], leading to a halt in the bacterial reproduction and growth without the requisite presentation of cell death or lysis[134,135]. Bacteriostatic treatment generally preserves cellular shape and does not affect viability. If there is no cell lysis, then the detection of untreated or treated bacteria via AFM also remains questionable. Figure 5.1 shows the comparison of the AFM height images of chloramphenicol treated and untreated *E.coli* bacteria. We observed no significant change in the surface morphology due to the lack of cell lysis. The height of the bacteria was ~ 270 nm for both treated and untreated bacteria. In addition, the fluorescence micrographs in Figure 5.2 show

retention of cell shape of *E.coli* following chloramphenicol treatment; thus, confirming expected

bacteriostatic effects.
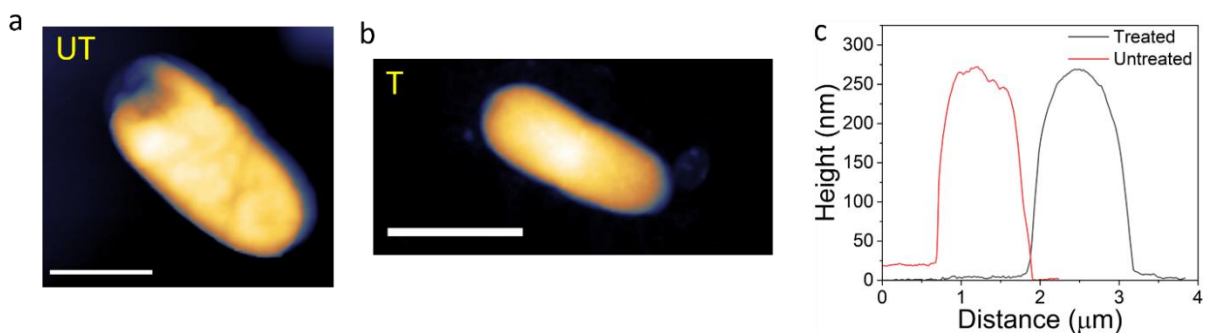
Figure 5.1 AFM height comparison of untreated (UT) vs treated (T) bacteria. As seen in (c) no significant changes in the surface morphology was observed. Scale bar is 10 µm.
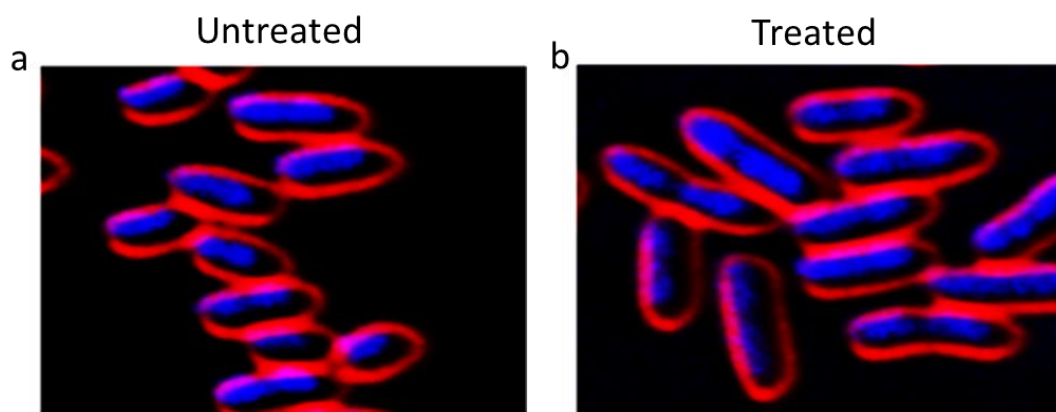
Figure 5.2 Fluorescence micrographs of exponentially-growing *E. coli* cells untreated or treated with 5 µg/ml chloramphenicol for 1 h. Membrane is stained with FM4-64 (red) and DNA is stained with DAPI (blue).

5.2 Detection of Untreated/Treated Bacteria Using FTIR Spectroscopy

5.2.1 Introduction

Novel techniques of label-free rapid bacterial chemical analysis focus on overcoming the restraints of traditional methods due to the superior denouements and expeditious processing[130]. Remarkably, Fourier transform infrared (FTIR) instruments, led by the recent advancements in laser design and utilization of chemometric analysis, allows undemanding and prompt sample

surveys[133]. FTIR spectroscopy is an innovative tool in the areas of biomedical analysis and food microbiology due to its access to the vibrational information concerning a variety of bacterial biochemical processes, replication states, and resistance to antibiotics[136–138]. One of the promising clinical applications of FTIR is bacterial classification based on unique vibrational fingerprints offering a rapid and reliable method of identification[139]. FTIR spectroscopy allows for facile sample analysis of various bacterial phase states, while excluding labor intensive techniques of sample preparation, which, however, does not guarantee a straightforward reproducibility of the results[139]. Therefore, further research is needed to develop robust protocols of using FTIR spectroscopy for various analytical purposes.

We demonstrated the application of FTIR spectroscopy for precise and prompt determination of variations in cell composition of *E.coli* bacteria in response to antibiotic treatment with chloramphenicol. The bacterial constituents identified via FTIR reveal basic differences in chemical signatures between antibiotic-treated and untreated cells, which are instantly distinguishable in the 2nd derivative of the FTIR spectra of *E. coli*. These results could serve as a foundation for future applications of label-free rapid detection of microbial pathogens in food safety and clinical settings.

5.2.2 Materials and Methods

Overnight cultures of *E. coli* (K-12) were grown at 22 °C in Luria-Bertani (LB) medium, and were then diluted 1:10 into fresh LB medium, and grown at 37 °C until mid-logarithmic growth phase (OD600=0.5). Cells (untreated) were harvested by centrifugation of 1 ml aliquots of culture (*E. coli*) and the resulting cell pellet was resuspended in 1 ml sterile water. To prepare the treated samples, 5 mg/ml of the bacteriostatic drug chloramphenicol was applied to cultures for 1 h at

37°C. Following treatment, samples were washed three times in fresh LB media. Aliquots of cultures (1 ml) were prepared as described earlier.

Standard ZnSe substrates and Si substrates were used in FTIR measurements and showed matching and reproducible results. The substrates were sterilized with acetone and isopropanol, followed by deionized water using ultrasonic bath for a period of 10 minutes. Afterwards, the substrates were dried under the flow of N_2 gas. Subsequently, a volume of 500 μL of bacterial cell media was aliquoted on a previously sterilized substrate. The bacterial samples were air dried for a period of 30 minutes in order to remove any water contents. The bacterial samples on Si substrates were used in all AFM measurements.

FTIR spectroscopy measurements were carried out in a transmission mode of FTIR spectrometer (Bruker Vertex 70) with air dried bacterial cells on ZnSe and Si substrates fixed vertically in the FTIR sample holder. Each sample was measured at least three times. Each spectrum was obtained as an average of 1000 scans recorded in less than 20 minutes. The results of repeated scans showed excellent agreement.

5.2.3 Results

We obtained 2nd derivative of the FTIR spectra to amplify opposing features of the non-treated and treated cells as shown in Figure 5.3. The characteristic spectra of *E. coli* were obtained in the range encompassing the vibrational "fingerprint" region of 1000 - 2000 cm^{-1} values, along with high wavenumber region of ~ 2900 - 3500 cm^{-1}. The derivative spectra of the *E. coli* cells in Figure 5.3 display notable distinctions in the protein spectral range, indicating the effects of the bacteriostatic treatment.
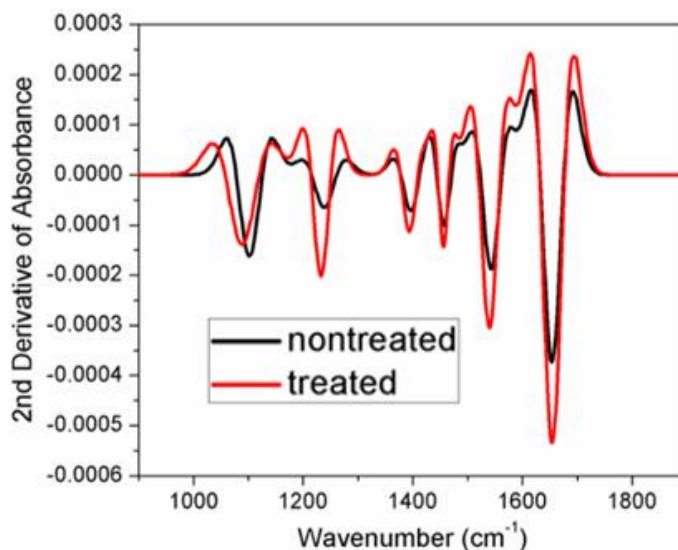
Figure 5.3 Second derivatives of the FTIR spectra of treated/untreated *E.coli* cells. Second derivatives of the FTIR spectra of the chloramphenicol-treated (red) and untreated (black) *E. coli* bacterial cells on Si substrate show significant differences.

The band assignment in Table 5.1 identifies the following spectral bands. The infrared region of 1087 to 1108 cm^{-1} is due to phosphate functional groups of DNA and RNA, along with C−OH, C−C, C-O-C stretching vibrations of cell wall peptidoglycan, polysaccharide, and lipopolysaccharide layers[140] .The spectral band around 1240-1312 cm^{-1} range corresponds to the asymmetric stretching of P=O bonds of phosphodiester, phospholipids, and protonated polyphosphates of nucleic acids[131]. Spectral bands around 1402-1450 cm^{-1} result from the stretching of deprotonated COO- functional groups in amino and fatty acids, while the latter additionally corresponds to the bending of CH$_2$ and CH$_3$ groups of peptidoglycan and lipopolysaccharides[140]. The characteristic Amide II band in the 1529 - 1546 cm^{-1} range is due to the N-H, C-N functional groups in proteins[140]. The Amide I band around 1659 cm^{-1} results from C=O stretching vibrations in proteins[140].

Table 5.1 Characteristic stretching vibrations of infrared spectral bands among *E. coli* and chloramphenicol (control).

	Assignment	
Wavenumber (cm^{-1})	*E. coli*	Chloramphenicol[141]
876	---	C-N stretch
1071	---	C-O stretch
1087	PO$_3$, C-O-C	---
1108	C−OH, C−C, and C-O-C	---
1236	P=O (asymmetric)	---
1346	---	C=O stretch
1395 – 1404	C=O (asymmetric and symmetric)	---
1450 -1457	=CH$_2$ (scissoring), COO-, CH$_2$ and CH$_3$	---
1537 – 1542	N–H, C–N (Amide II)	---
1650	Amide I	---

5.2.4 Discussion

Notably, FTIR deviations between treated and untreated groups generally indicate nucleic acid conformational changes and denaturation processes, observed in the range of 1010 cm^{-1} - 1106 cm^{-1}[142]. The FTIR signals from chloramphenicol do not make a significant contribution to the observed spectra due to the relatively small concentrations of chloramphenicol used for the treatment compared to the concentrations of the bacterial cellular components. Also, the chloramphenicol treatment resulted in the suppression of the relative band intensities of the 1500 – 1700 cm^{-1} range.

FTIR spectra of *E. coli* showed the band in the 900-1200 cm^{-1} range, which is indicative of the cell wall carbohydrate composition, and can be utilized to distinguish bacteria at the strain

level[143]. Therefore, difference in the relative FTIR band intensities, following the antibiotic treatment, indicates alterations in the cell wall composition at the molecular level. The peptidoglycan sacculus defines cellular shape due to its rigidity[144]. Periplasm constitutes an aqueous cavity between outer and inner membranes in gram-negative bacteria, which is enriched with various proteins, adding to its viscosity[145]. The FTIR band around 1400 cm^{-1} demonstrates a variation in the protonation states of carboxylic functional groups among polar amino acids, such as asparagine and glutamine[146]. Additionally, deprotonated carboxylic groups indicate a carboxylate proximally located to hydroxyl groups within polypeptides[147]. The absorption band at 1452 cm^{-1} corresponds to bond bending of ethyl and methyl groups found on bacterial cell wall, which results from the aliphatic nature of amino acids[140]. Inner membrane integrates diverse polypeptides, involved in cellular metabolic processes, such as transport and biosynthesis[148]. The nature of *E.coli* inner membrane bilayer encompasses specific phospholipids, including phosphatidylethanolamine and phosphatidyl glycerol[148]. Bacterial spectra exhibited 1243 cm^{-1} band that is attributed to the asymmetric stretching of phosphate diester P=O bonds and protonated polyphosphate[140]. A wavenumber shift in the treated group represents a diminished energy state, suggesting deprotonation of polyphosphate leading to the reduced strength of the P=O bond. Since phosphate groups are constituents of the phospholipids and peptidoglycan cell wall composition, the significant differences in the FTIR spectra reveal the modifications on the bacterial surface[140]. Similar changes of the bacterial molecular constituents were previously observed in response to several antibiotic treatments[149], however, the morphological correlation with the bacteriostatic treatment was not performed.

5.3 2D-TMDs as Nanoscale Probes to Detect Untreated and Treated Bacteria

5.3.1 Nano-optical Imaging of Bacteria - 2D TMD Interaction

Nanomaterials, especially 2D-TMDs can be harnessed as biosensors and can provide excellent platform for biosensing, due to good biocompatibility, high surface area and due their unique and promising optoelectronic and electrochemical properties[150].

In this work, we developed single bacterial cell-2D material interaction model based on two types of interaction, namely, mechanical and electrical. We analyzed these two interaction models using conventional confocal microscopy and NF imaging.

Mechanical interaction involves strain from the analyte to the 2D material, causing exciton funneling. For a monolayered 2D material, the confirmation of exciton funneling is determined by the PL spectroscopy which shows enhanced PL intensity at the strained region compared to the surrounding region of low to absence of strain[65,106,151]. In our work, when the *E.coli* (K12) was dropcasted on the 2D TMD (MoS_2), the band-gap of the strained TMD decreases in the area where *E.coli* adheres to MoS_2 as shown in Figure 5.4a, causing the photoexcited electron- hole pairs funnel towards the area of maximum strain, leading to localized PL intensity enhancement as shown by the thick, red arrow, as compared to flat material shown by the thin red arrow.

Electrical interaction involves two mechanisms, firstly, electron tunneling from the Au/Ag plasmonic tip to the bacteria@2D TMD and, secondly, the charge transfer between the bacteria and the 2D material. The electron tunneling mechanism has previously been observed when the distance between the tip and the sample (TSD) decreases, specifically to TSD ~ 0.36 nm, which is also termed as "quantum regime" or subnanometer regime[124,126,127,152–159].
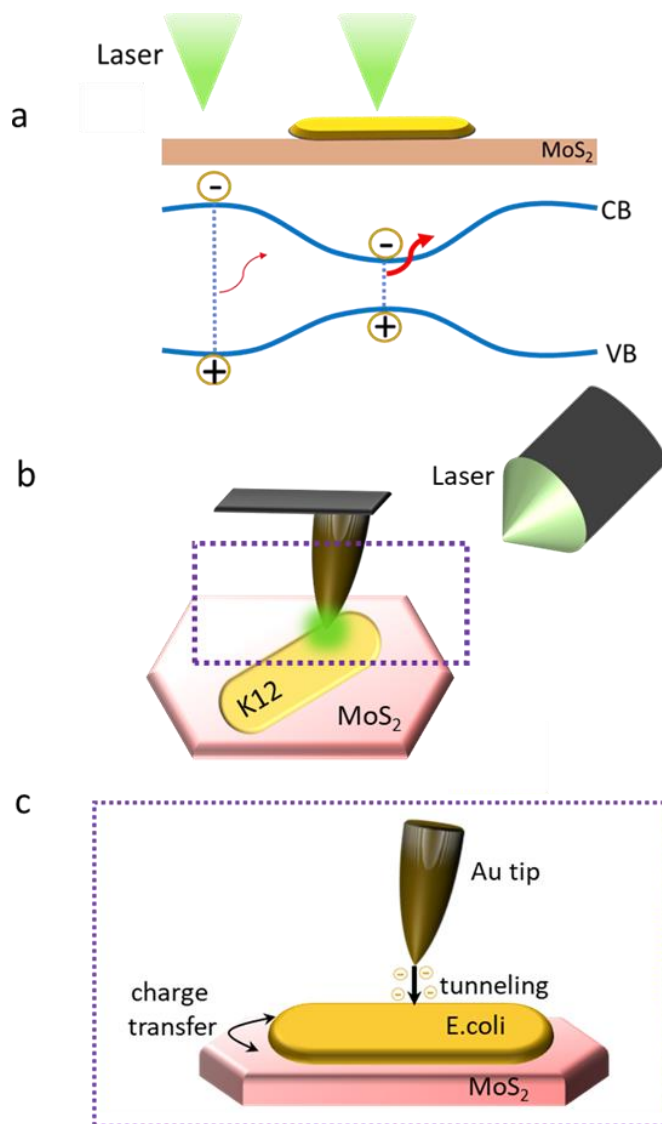
Figure 5.4 Schematic of mechanical and electrical mechanisms of interaction of *E.coli* and MoS$_2$. (a) Exciton funneling formed by bacteria. Bacteria induces strain which decreases the band gap of MoS$_2$ such that the area where bacteria adheres on MoS$_2$ emits enhanced PL as shown by the thick red arrow, as compared to the flat region as shown by thin red arrow. (b) Schematic of the TEPL experiment. The 532 nm laser illuminates the plasmonic Au tip such that the maximum electric field is at the apex of the Au tip. (c) Electrical interaction mechanisms involving tunneling of hot electrons from the Au tip to bacteria and charge transfer between MoS$_2$ and *E.coli*.

5.3.2 Detection of Untreated/Treated Bacteria Using Exciton Funneling

Here, we used the mechanical interaction model, which involves the formation of exciton funnels due to the in-plane tensile strain caused by the bacteria (*E.coli*), as shown in figure 5.5c.

The detection is based on the strength of exciton funnels caused by both treated and untreated *E.coli* upon adhering to MoS$_2$.

Figure 5.5a, b shows the brightfield optical images of the untreated and treated *E.coli* on CVD-grown MoS$_2$. The treated *E.coli* culture was obtained by treating the bacteria with the bacteriostatic antibiotic, chloramphenicol for 1h at 37°C. The detailed procedure is mentioned in section 5.2.2.
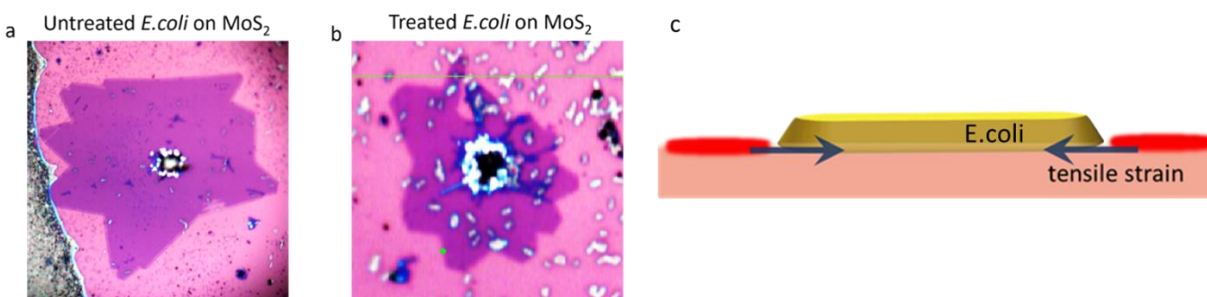

Figure 5.5 Brightfield optical images of untreated and treated *E.coli* on MoS$_2$. (c) Schematic model of in-plane tensile strain caused by bacteria on 2D TMD. Due to this strain, the areas around the bacteria poles emit enhanced PL as shown by dark red areas.

5.3.2.1 Bacterial Adhesion to Surfaces

Bacterial adhesion is an important step in biofilm formation which may cause problems in medical, environmental and industrial setup. *E.coli's* ability to establish itself within different surfaces mainly relies on the adherence to host surfaces, which is mediated by a variety of adhesins. This adherence to host surfaces prevents physical clearance and engages the bacteria in the colonization process[160].

Due to the net negative charge of *E.coli* cell envelope, they are subjected to electrostatic forces when approaching surfaces[161]. Typically, to avoid this repulsive barrier, bacteria uses flagella/pili as a grappling hook to enhance cell-enhancement[162–164].

In general three major types of gram-negative bacterial cell adhesins to abiotic surfaces have been reported before, namely fimbrial, non-fimbrial and discrete polysaccharide adhesins[161].

While there is a whole sea of research done on identifying the proteins/monomers, responsible for bacterial adhesion, our main interest of the work is on single cell *E.coli*.

Fimbrial adhesins for *E.coli* adhesion are categorized into major pilus proteins or minor pilus proteins/assembly proteins. EcpA or MatA are examples of pilus protein and EcpC, EcpD, EcpE are examples of minor proteins/assembly proteins[165]. The non-fimbrial adhesin for *E.coli* is YeeJ[166]. YeeJ is an inverse autotransporter from *E.coli* that binds to peptidoglycan and promotes biofilm formation[167]. It belongs to the intimin/invasin family which are localized on the outer membrane of *E.coli.*

Even though identifying specific adhesin interacting with 2D TMDs is beyond the scope of this work, we analyze the interaction of these bacteria adhesins with 2D TMDs by observing the change in the PL emission of the 2D TMD using mechanical and electrical mechanism.

5.3.2.2 Results

Figure 5.6 shows exciton funneling caused by both untreated and treated *E.coli* on MoS$_2$. We developed a Gaussian-fit 2-band model to deconvolute the raw PL signal from the bacteria (funnel) and flat MoS$_2$, into UStr and Str as shown in Figure 5.6 (c, d, g and h). The strain caused due to exciton funneling was mapped by integrating the area under Str band as shown by the red shade in Figure 5.6(c).

Notably, the maximum PL signal is emitted from the pole of the bacteria as shown in Figure 5.6 (b, f) which indicates that the adhesion force is maximum at the poles compared to the center of the bacteria. Previous bacteria mediated strain-based studies have shown that a single *X.fastidiosa* cell, upon adhering to InP nanowire arrays, induces larger adhesion forces at the cell poles than the center of the bacteria which is shown by the bending of the nanowires at the poles of the single-
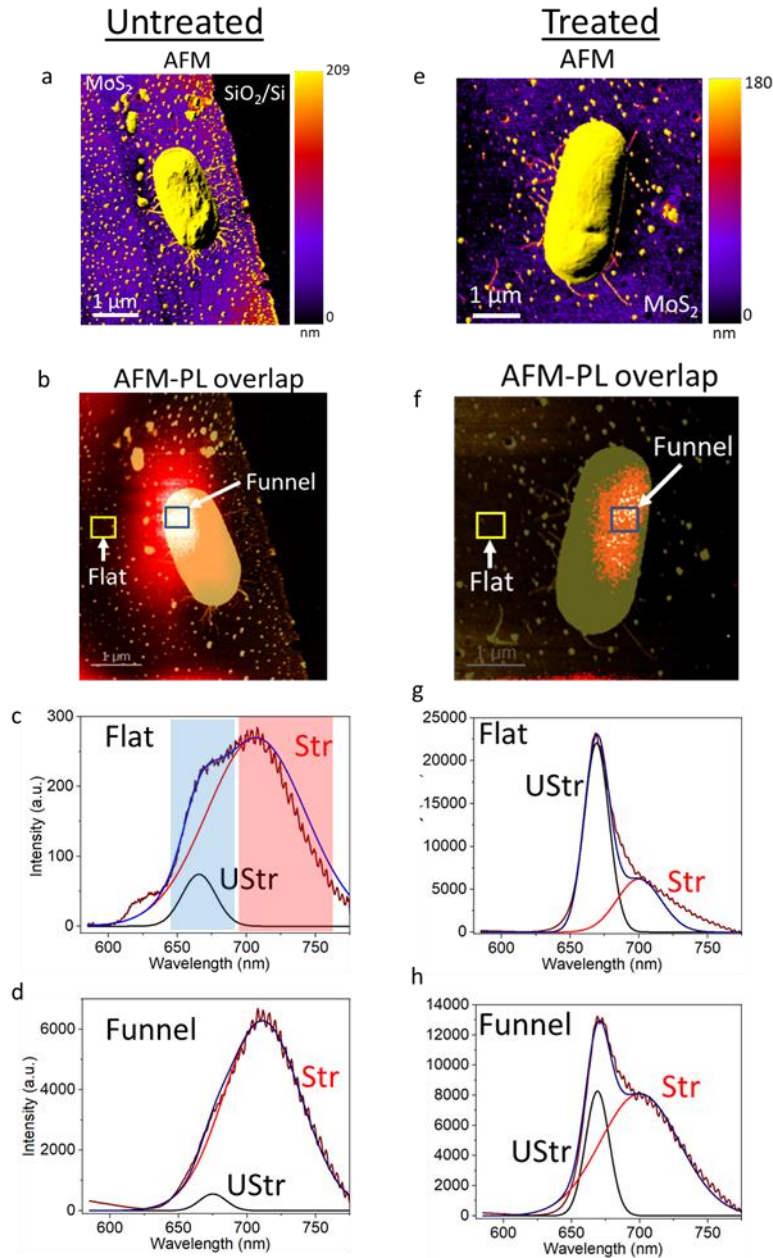
Figure 5.6 Exciton funnels by untreated and treated *E.coli* on MoS$_2$. (a) and (e) show the AFM and (b) and (f) show the overlap of AFM and PL maps, of the untreated and treated *E.coli*, respectively. The PL maps were obtained by integrating the area under Str band, which is the characteristic peak for the strain .(c) and (d) are the spectra recorded from the flat and funnel region of untreated *E.coli*, respectively. (g) and (h) are spectra recorded from the flat and funnel region of treated *E.coli*, respectively

cell bacteria[168]. The bacteria poles are the sites, responsible for the cell-cell contact[169], and the

secretion of extracellular polymeric substances (EPS)[169,170]. These secreted EPS layers and

filaments at the bacteria poles provide mechanical support to the bacteria. In addition, the 'polar proteins' are also essential for cell-cycle regulation, cell differentiation, chemotaxis and more importantly for cell adhesion[171]. Hence, the presence and the nature of the proteins at the poles is responsible for the strain caused by the bacteria on 2D TMDs.

On comparing the intensity of the exciton funnels created by both untreated (UT) and treated (T) *E.coli*, we calculated the enhancement of the PL intensity recorded from the area of maximum strain (funnel), with respect to the PL intensity of flat, unstrained MoS_2, using the formula,

$$EF = \frac{I_{Funnel}}{I_{Flat}} - 1$$

As shown in Table 5.2, the funnel intensity of the untreated bacteria is 22 times larger compared to the treated bacteria, 30 %.This shows that untreated *E.coli* makes ~ 73x stronger exciton funnels compared to the treated *E.coli*.

Table 5.2 Far-field Enhancement Factor (EF) of exciton funnels in untreated and treated bacteria

E.coli (UT/T)	Intensity (a.u.) (Str_{max})	Enhancement Factor (EF) $\frac{I_{Funnel}}{I_{Flat}} - 1$
UT - Funnel	6281	22
UT - Flat	270	
T - Funnel	8098	0.3
T - Flat	6212	

This difference in the intensity of the exciton funnels formed by the untreated and treated bacteria is because of the weak adhesion forces by the treated bacteria since the antibiotic chloramphenicol inhibits the synthesis of the bacterial proteinaceous adhesins, which are the

protein factors responsible for the adhesion[172]. This contention is further substantiated by the fact that after growing *E. coli* in low concentrations of antibiotics, it is a possible that *E.coli* can lose their pili which are responsible for the bacterial adhesion[161].

In addition, we also performed high resolution NF imaging (Figure 5.7) on the same area as shown in figure 5.6 (a) and (e) to get more localized positions of the untreated and treated bacteria-formed
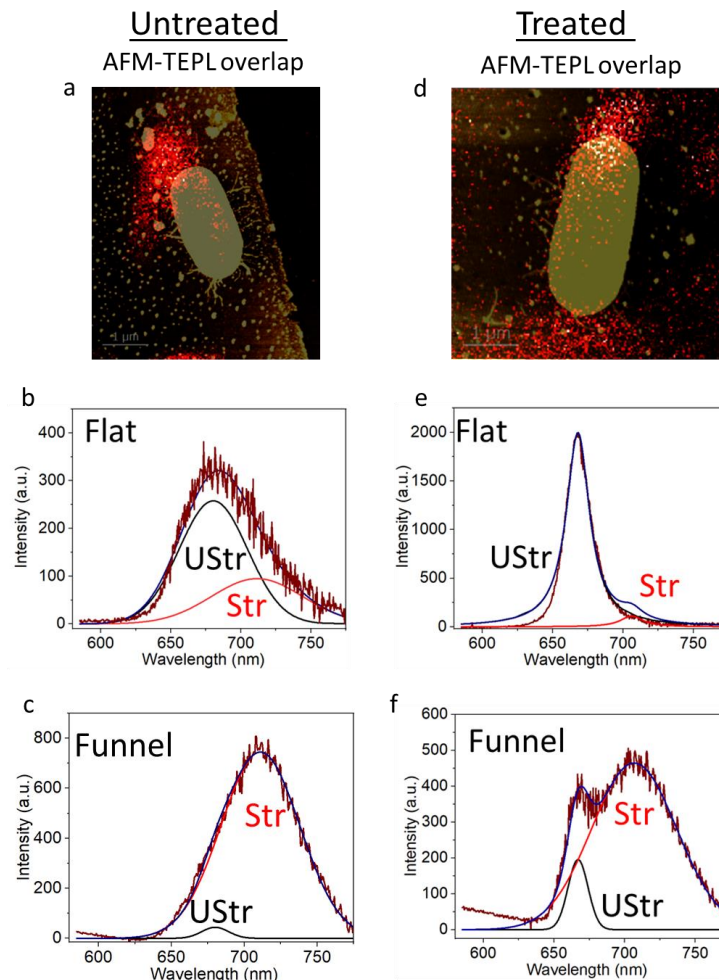

Figure 5.7 Near-field exciton funnels by untreated and treated *E.coli* on MoS_2. The TEPL maps were obtained by integrating the area under Str band, which is the characteristic strain peak.(b) and (c) are the spectra recorded from the flat and funnel region of untreated *E.coli*, respectively. (e) and (f) are spectra recorded from the flat and funnel region of treated *E.coli*, respectively

70

exciton funnels. In addition a more reliable quantitative analysis of the intensity of exciton funnels is obtained using NF PL intensity values. A visual comparison of the low-resolution FF PL maps (Figure 5.6 (b), (f)) and high-resolution NF TEPL maps (Figure 5.7 (b) and (e)) show more localized location of the exciton funnels near the poles of the bacteria, as shown in the case of NF imaging, which is contrary to the FF imaging where the funnels are shown on the top of the bacteria.

We compared the intensity of the exciton funnels by both untreated (UT) and treated (T) *E.coli* as shown in table 5.3 , in the similar way as shown in table 5.2 for FF . As shown in Table 5.3, the funnel intensity of the untreated *E.coli* is 7 times larger as compared to the treated *E.coli*, 300%. This shows that untreated *E.coli* makes ~ 2.3x stronger exciton funnels than treated *E.coli*.

Table 5.3 Near-field Enhancement Factor (EF) of exciton funnels in untreated and treated bacteria

E.coli type (UT/T)	Intensity (a.u.) (Str$_{max}$)	Enhancement Factor (EF) $\dfrac{I_{Funnel}}{I_{Flat}} - 1$
UT - Funnel	745	7
UT - Flat	95	
T - Funnel	465	3
T - Flat	111	

5.3.3 Detection of Untreated and Treated Bacteria Using Electrical Interaction with 2D Materials

Detection of untreated and treated bacteria through electrical mechanism is based on two processes, firstly the directional tunneling of hot electrons from the plasmonic Au tip to the bacteria to MoS$_2$. This happens when the tip-bacteria distance (TBD) is ~ 0.36 nm, which can also be referred to as tip is "in-contact" with the bacteria. The second process involves charge transfer

mechanism between the bacteria and the 2D material, also termed as chemical mechanism (CM). Here, we focus on the charge tunneling mechanism.

5.3.3.1 Charge Tunneling Mechanism

The mechanism of charge transfer for very small gaps between two nanoparticle dimers has been very well studied before. For distances less than 0.5 nm, electrons can tunnel through the flat energy barrier between the nanoparticles, enabling a tunneling-induced charge transfer plasmon (CTP)[152,153,173]. This type of tunneling is termed as direct tunneling and the tunneling efficiency gets stronger with decreasing tip size[174]. In addition, directional hot electrons have been shown to tunnel from plasmonic tip to $MoSe_2$-WSe_2[129] and MoS_2-WS_2[125,151] on SiO_2/Si substrate, when the tip-sample distance (TSD) ~ 0.3 nm, also termed as "quantum regime".

On the other hand, in addition to the direct tunneling mechanism, Fowler-Nordheim tunneling, which is based on the field-emission effect in the presence of high electric fields[175,176], has been utilized in the full quantum mechanical study of the nonlinear effects for the field enhancement of a small nanoparticle dimer[173]. Typically, in the Fowler-Nordheim tunneling regime, the tunneling barrier between nanoparticles have sloped energy-space profile. Due to this, the electrons do not tunnel directly to the other nanoparticle, instead they can tunnel from the conduction band of one nanoparticle into the gap, from which they can go to the other nanoparticle. However, the consequence of this is the formation of a conductive gap, or a "space-charge" region[177]. Contextually, space charge can be considered as the continuum of electrons emitted from one nanoparticle into the entire gap region[178].

Our work on tunneling from a plasmonic Au tip to *E.coli*@MoS_2 follows Fowler-Nordheim tunneling, since we observe tunneling even with gap size bigger than 0.3 nm. Figure 5.8 (a) shows the capacitance derivative map of *E.coli* on MoS_2-WS_2 heterostructure, which clearly shows

different materials. Upon measuring contact potential difference (CPD) of this area as shown in Figure 5.8 (b), we clearly observe the CPD signal which correlates with the shape of WS$_2$ on the bacterial cell. During Fowler-Nordheim tunneling, there is a formation of the space charge region.
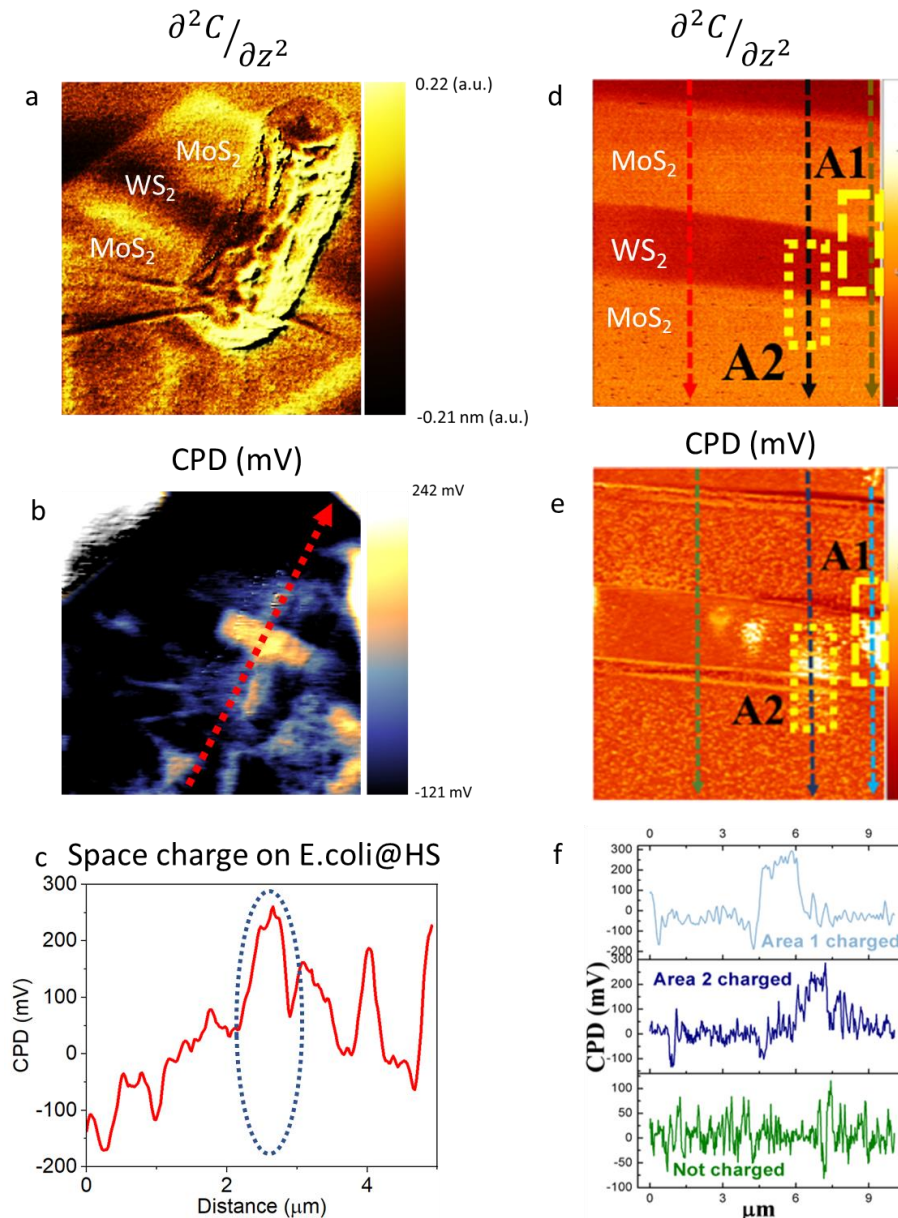

Figure 5.8 Accumulative doping of hot electrons in the bacteria on MoS$_2$-WS$_2$ heterostructure. Hot electrons, tunneled from the plasmonic tip, using Fowler-Nordheim mechanism, can accumulate in the gaps between the tip and 2D material. (c) the profile of contact potential difference (CPD) across the red dashed line in (b). CPD map of MoS$_2$-WS$_2$ heterostructure (e) shows the similar effect of accumulative doping in WS$_2$. The CPD profiles for A1 and A2 show the increase in CPD on the WS$_2$ part of the heterostructure.

The CPD of WS$_2$ on the bacteria as shown in Figure 5.8 (b) and in the profile 5.82 (c), marked within blue dashed oval, is an indication of the accumulation of charges/ hot-electrons from the plasmonic tip. We observed similar accumulation of hot electrons on MoS$_2$-WS$_2$ heterostructure as shown in Figure 5.8 (e). We investigated 2 areas, A1 and A2. A1 had MoS$_2$ on top and WS$_2$ below, and A2 had WS$_2$ on top and MoS$_2$ below. As seen by the profiles in Figure 5.8 (f), WS$_2$ has more accumulated hot electrons than MoS$_2$, which is consistent with the results shown in 5.8 (b).

This accumulation of electrons from the plasmonic tip towards the sample of interest, due to Fowler-Nordheim tunneling can be used in a wide-variety of surface interactions, where the gap sizes are bigger than 0.3 nm, which is the direct quantum tunneling regime. For our interest, this tunneling mechanism and accumulative doping of electrons can be used to study the nanoscale interaction of treated and untreated bacteria or even in the field of cancer imaging and therapy, where tunneling of high energy hot electrons can effectively kill the cancer cells due to the photothermal effect.

5.3.3.2 Detection of Untreated/Treated Bacteria Using Tunneling

Our previous work on exciton funneling (section 5.3.2) by bacteria, demonstrated stronger adhesion at the bacteria poles due to the presence of polar proteins aggregation. Here, we take our nanoscale imaging technology to study a correlative measurement of AFM, Contact Potential Difference (CPD) and TEPL across the bacterial cell to detect untreated and treated bacteria. Using this correlation, nanoscale analysis of bacteria-2D TMD interface can be obtained. Our hypothesis is based on bacteria assisted tunneling towards MoS$_2$ is stronger in the case of untreated *E.coli* poles as compared to treated *E.coli*.

Figure 5.9 shows the correlative AFM, TEPL and CPD signals of untreated and treated *E.coli* on MoS$_2$. The TEPL maps were obtained by integrating the area under UStr band as shown by the blue shade in Figure 5.6c. We observed that the bacteria assisted tunneling is enhanced on the poles of the untreated *E.coli* (Figure 5.9 b) as compared to the poles of treated *E.coli* (Figure 5.9 d), which confirms that the polar proteins are strongly interacting with MoS$_2$ in the case of untreated bacteria. The AFM, CPD and TEPL correlated profiles across the red dashed line for
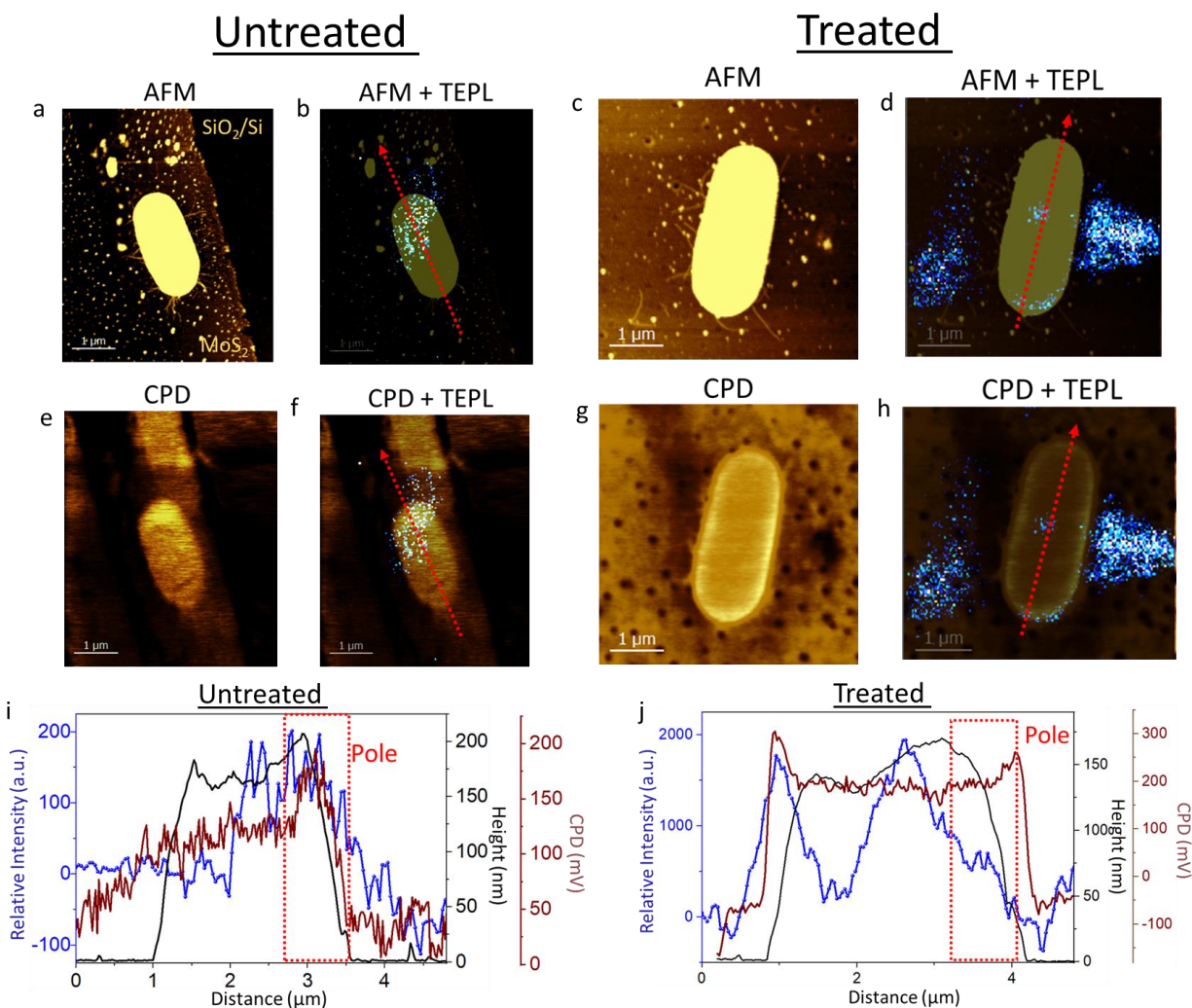

Figure 5.9 Correlated map comparison between the untreated and treated *E.coli* on MoS$_2$. (a), (e) and (c), (g) show AFM and CPD maps of untreated and treated *E.coli*, respectively. (b), (f) and (d) and (h) show the AFM-TEPL overlap and CPD-TEPL overlap of untreated and treated *E.coli*, respectively. The AFM, CPD and TEPL line profiles across the red dashed line a strong correlation in the case of the untreated *E.coli*.

both untreated and treated *E.coli* are shown in Figure 5.9 (i) and (j), respectively. A strong TEPL

and CPD correlation is shown in the case of the untreated *E.coli*, integrated under the red dashed

rectangular box.

Chapter 6: Conclusion

The goal of this work was to develop an efficient microbial detection and inactivation platform, using nanophotonics and nanomaterials. We developed a new virus inactivation technique using pulsed nanosecond 266 nm UV laser coupled to an integrating cavity (LIC), which overcomes the limitations of the current state-of-the-art UV inactivation strategies based on UV lamps by providing higher efficiency, low dose requirement, and shorter irradiation times. The LIC device shows > 2 orders of magnitude higher efficiency compared to UV lamps and can inactivate SARS-CoV-2 at ~ 1 millisecond effective irradiation time. This LIC device has huge potential for development of air and water purification systems and LIC device-based air conditioners can be used in enclosed spaces such as airplanes, stores and offices.

In addition, we used nanomaterials, specifically, 2D TMDs for the detection of bacteriostatic treatment of bacteria. We used exceptional optical properties of MoS_2, such as efficient PL for optical biosensing of the untreated and chloramphenicol-treated *E.coli*. We developed single bacterial cell-2D TMD interaction model based on the mechanical (in-plane) and electrical (out-of-plane) interactions. The mechanical interaction model is based on the strain caused by untreated and treated *E.coli* on MoS_2, leading to formation of exciton funnels. Due to weak adhesion forces, the treated *E.coli* generated smaller exciton funnels as compared to untreated *E.coli*. The mechanical interaction model opens new avenues for real-time bacteriostatic detection using flexible 2D TMDs and can avoid conventional time consuming and labor demanding detection techniques. The electrical interaction model was based on quantum plasmonic charge tunneling. We showed the first demonstration of 'space-charge' formation due

to tunneling through bacteria towards 2D TMD using the correlated NF imaging and CPD. We used this electrical interaction for the detection of bacteriostatic treatment and observed stronger charge tunneling in the case of untreated *E.coli* as compared to the treated due to the presence of polar proteins. The electrical interaction model opens a new platform to analyze cell-surface interaction at the nanoscale.

References

1. Ozaki, Y., Saito, Y. & Kawata, S. Introduction to FUV and DUV Spectroscopy. in *Far-and Deep-Ultraviolet Spectroscopy* 1–16 (Springer, 2015).

2. Rutala, W. A. & Weber, D. J. Disinfection and sterilization in health care facilities: what clinicians need to know. *Clinical infectious diseases* **39**, 702–709 (2004).

3. Cutler, T. D. & Zimmerman, J. J. Ultraviolet irradiation and the mechanisms underlying its inactivation of infectious agents. *Animal Health Research Reviews* **12**, 15–23 (2011).

4. Darnell, M. E., Subbarao, K., Feinstone, S. M. & Taylor, D. R. Inactivation of the coronavirus that induces severe acute respiratory syndrome, SARS-CoV. *Journal of virological methods* **121**, 85–91 (2004).

5. McDevitt, J. J., Rudnick, S. N. & Radonovich, L. J. Aerosol susceptibility of influenza virus to UV-C light. *Applied and environmental microbiology* **78**, 1666–1669 (2012).

6. Buonanno, M., Welch, D., Shuryak, I. & Brenner, D. J. Far-UVC light (222 nm) efficiently and safely inactivates airborne human coronaviruses. *Scientific Reports* **10**, 1–8 (2020).

7. Ambardar, S., Nguyen, D., Binder, G., Withers, Z. W. & Voronine, D. V. Quantum leap from gold and silver to aluminum nanoplasmonics for enhanced biomedical applications. *Applied Sciences* **10**, 4210 (2020).

8. Hadi, J., Dunowska, M., Wu, S. & Brightwell, G. Control Measures for SARS-CoV-2: A Review on Light-Based Inactivation of Single-Stranded RNA Viruses. *Pathogens* **9**, 737 (2020).

9.   Kim, D.-K., Kim, S.-J. & Kang, D.-H. Inactivation modeling of human enteric virus surrogates, MS2, Qβ, and ΦX174, in water using UVC-LEDs, a novel disinfecting system. *Food Research International* **91**, 115–123 (2017).

10.   Santa Maria, F. *et al.* Inactivation of Zika virus in platelet components using amotosalen and ultraviolet A illumination. *Transfusion* **57**, 2016–2025 (2017).

11.   Fryk, J. J. *et al.* Reduction of Zika virus infectivity in platelet concentrates after treatment with ultraviolet C light and in plasma after treatment with methylene blue and visible light. *Transfusion* **57**, 2677–2682 (2017).

12.   Schubert, P., Johnson, L., Marks, D. C. & Devine, D. V. Ultraviolet-based pathogen inactivation systems: untangling the molecular targets activated in platelets. *Frontiers in medicine* **5**, 129 (2018).

13.   Owada, T. *et al.* Establishment of culture systems for G enotypes 3 and 4 hepatitis E virus (HEV) obtained from human blood and application of HEV inactivation using a pathogen reduction technology system. *Transfusion* **54**, 2820–2827 (2014).

14.   Kwon, S.-Y. *et al.* Pathogen inactivation efficacy of Mirasol PRT System and Intercept Blood System for non-leucoreduced platelet-rich plasma-derived platelets suspended in plasma. *Vox sanguinis* **107**, 254–260 (2014).

15.   Lanteri, M. C. *et al.* Inactivation of a broad spectrum of viruses and parasites by photochemical treatment of plasma and platelets using amotosalen and ultraviolet A light. *Transfusion* **60**, 1319–1331 (2020).

16.   Aubry, M., Richard, V., Green, J., Broult, J. & Musso, D. Inactivation of Z ika virus in plasma with amotosalen and ultraviolet a illumination. *Transfusion* **56**, 33–40 (2016).

17.   Girard, Y. A., Santa Maria, F. & Lanteri, M. C. Inactivation of yellow fever virus with amotosalen and ultraviolet A light pathogen-reduction technology. *Transfusion* **60**, 622–627 (2020).

18.   Inagaki, H., Saito, A., Sugiyama, H., Okabayashi, T. & Fujimoto, S. Rapid inactivation of SARS-CoV-2 with deep-UV LED irradiation. *Emerging Microbes & Infections* **9**, 1744–1747 (2020).

19.   Heßling, M., Hönes, K., Vatter, P. & Lingenfelder, C. Ultraviolet irradiation doses for coronavirus inactivation–review and analysis of coronavirus photoinactivation studies. *GMS hygiene and infection control* **15**, (2020).

20.   Criscuolo, E. *et al.* Fast inactivation of SARS-CoV-2 by UV-C and ozone exposure on different materials. *Emerging Microbes & Infections* 1–18 (2021).

21.   Heilingloh, C. S. *et al.* Susceptibility of SARS-CoV-2 to UV irradiation. *American journal of infection control* **48**, 1273–1275 (2020).

22.   Storm, N. *et al.* Rapid and complete inactivation of SARS-CoV-2 by ultraviolet-C irradiation. *Scientific reports* **10**, 1–5 (2020).

23.   Kitagawa, H. *et al.* Effect of intermittent irradiation and fluence-response of 222 nm ultraviolet light on SARS-CoV-2 contamination. *Photodiagnosis and Photodynamic Therapy* **33**, 102184 (2021).

24.   Minamikawa, T. *et al.* Quantitative evaluation of SARS-CoV-2 inactivation using a deep ultraviolet light-emitting diode. *Scientific Reports* **11**, 1–9 (2021).

25.   Biasin, M. *et al.* UV-C irradiation is highly effective in inactivating SARS-CoV-2 replication. *Scientific Reports* **11**, 1–7 (2021).

26. Liu, S. *et al.* Sec-Eliminating the SARS-CoV-2 by AlGaN Based High Power Deep Ultraviolet Light Source. *Advanced functional materials* **31**, 2008452 (2021).

27. Horton, L. *et al.* Spectrum of virucidal activity from ultraviolet to infrared radiation. *Photochemical & Photobiological Sciences* **19**, 1262–1270 (2020).

28. Kampf, G., Voss, A. & Scheithauer, S. Inactivation of coronaviruses by heat. *Journal of Hospital Infection* **105**, 348–349 (2020).

29. Trujillo, R. & Dugan, V. L. Synergistic inactivation of viruses by heat and ionizing radiation. *Biophysical journal* **12**, 92–113 (1972).

30. Abraham, J. P., Plourde, B. D. & Cheng, L. Using heat to kill SARS-CoV-2. *Reviews in Medical Virology* **30**, e2115 (2020).

31. Tsen, S.-W. D. *et al.* Ultrashort pulsed laser treatment inactivates viruses by inhibiting viral replication and transcription in the host nucleus. *Antiviral research* **110**, 70–76 (2014).

32. Tsen, K. T., Tsen, S.-W. D., Sankey, O. F. & Kiang, J. G. Selective inactivation of micro-organisms with near-infrared femtosecond laser pulses. *Journal of Physics: Condensed Matter* **19**, 472201 (2007).

33. Tsen, K.-T. *et al.* Inactivation of viruses by coherent excitations with a low power visible femtosecond laser. *Virology journal* **4**, 1–5 (2007).

34. Prodouz, K. N., Fratantoni, J. C., Boone, E. J. & Bonner, R. F. Use of laser-UV for inactivation of virus in blood products. (1987).

35. Daryany, M. K. A., Hosseini, S. M., Raie, M., Fakharie, J. & Zareh, A. Study on continuous (254 nm) and pulsed UV (266 and 355 nm) lights on BVD virus inactivation and its effects on biological properties of fetal bovine serum. *Journal of Photochemistry and Photobiology B: Biology* **94**, 120–124 (2009).

36. Nikogosyan, D. N., Kapituletz, S. P. & Smirnov, Y. A. Effects of ultraviolet laser radiation on Venezuelan equine encephalomyelitis virus. *Photochemistry and photobiology* **54**, 847–849 (1991).

37. Chhowalla, M. *et al.* The chemistry of two-dimensional layered transition metal dichalcogenide nanosheets. *Nature chemistry* **5**, 263–275 (2013).

38. Nicolosi, V., Chhowalla, M., Kanatzidis, M. G., Strano, M. S. & Coleman, J. N. Liquid exfoliation of layered materials. *Science* **340**, (2013).

39. Sun, Y., Gao, S. & Xie, Y. Atomically-thick two-dimensional crystals: electronic structure regulation and energy device construction. *Chemical Society Reviews* **43**, 530–546 (2014).

40. Loo, A. H., Bonanni, A., Sofer, Z. & Pumera, M. Exfoliated transition metal dichalcogenides (MoS2, MoSe2, WS2, WSe2): an electrochemical impedance spectroscopic investigation. *Electrochemistry Communications* **50**, 39–42 (2015).

41. Tsai, D.-S. *et al.* Few-layer MoS2 with high broadband photogain and fast optical switching for use in harsh environments. *Acs Nano* **7**, 3905–3911 (2013).

42. Tongay, S. *et al.* Broad-range modulation of light emission in two-dimensional semiconductors by molecular physisorption gating. *Nano letters* **13**, 2831–2836 (2013).

43. Hu, P. *et al.* Highly responsive ultrathin GaS nanosheet photodetectors on rigid and flexible substrates. *Nano letters* **13**, 1649–1654 (2013).

44.   Mak, K. F., He, K., Shan, J. & Heinz, T. F. Control of valley polarization in monolayer MoS 2 by optical helicity. *Nature nanotechnology* **7**, 494–498 (2012).

45.   Britnell, L. *et al.* Field-effect tunneling transistor based on vertical graphene heterostructures. *Science* **335**, 947–950 (2012).

46.   Yu, W. J. *et al.* Vertically stacked multi-heterostructures of layered materials for logic transistors and complementary inverters. *Nature materials* **12**, 246–252 (2013).

47.   Xue, W. *et al.* Nano-optical imaging of monolayer MoSe2-WSe2 lateral heterostructure with subwavelength domains. *Journal of Vacuum Science & Technology A: Vacuum, Surfaces, and Films* **36**, 05G502 (2018).

48.   Ugeda, M. M. *et al.* Giant bandgap renormalization and excitonic effects in a monolayer transition metal dichalcogenide semiconductor. *Nature materials* **13**, 1091–1095 (2014).

49.   Guo, Y. & Robertson, J. Band engineering in transition metal dichalcogenides: Stacked versus lateral heterostructures. *Applied Physics Letters* **108**, 233104 (2016).

50.   Gong, C. *et al.* Band alignment of two-dimensional transition metal dichalcogenides: Application in tunnel field effect transistors. *Applied Physics Letters* **103**, 053513 (2013).

51.   Cheng, R. *et al.* Electroluminescence and photocurrent generation from atomically sharp WSe2/MoS2 heterojunction p–n diodes. *Nano letters* **14**, 5590–5597 (2014).

52.   Roy, T. *et al.* 2D-2D tunneling field-effect transistors using WSe2/SnSe2 heterostructures. *Applied Physics Letters* **108**, 083111 (2016).

53.   Tang, C., Jia, S., Chen, W., Lou, J. & Voronine, D. V. Nano-optical imaging of monolayer MoSe2 using tip-enhanced photoluminescence. *arXiv preprint arXiv:1704.02396* (2017).

54.   Holzinger, M., Le Goff, A. & Cosnier, S. Nanomaterials for biosensing applications: a review. *Frontiers in chemistry* **2**, 63 (2014).

55.   Chen, Y., Tan, C., Zhang, H. & Wang, L. Two-dimensional graphene analogues for biomedical applications. *Chemical Society Reviews* **44**, 2681–2701 (2015).

56.   Loo, A. H., Bonanni, A. & Pumera, M. Strong dependence of fluorescence quenching on the transition metal in layered transition metal dichalcogenide nanoflakes for nucleic acid detection. *Analyst* **141**, 4654–4658 (2016).

57.   Zhang, Y. *et al.* Single-layer transition metal dichalcogenide nanosheet-based nanosensors for rapid, sensitive, and multiplexed detection of DNA. *Advanced Materials* **27**, 935–939 (2015).

58.   Zhu, C. *et al.* Single-layer MoS2-based nanoprobes for homogeneous detection of biomolecules. *Journal of the American Chemical Society* **135**, 5998–6001 (2013).

59.   Ge, J., Ou, E.-C., Yu, R.-Q. & Chu, X. A novel aptameric nanobiosensor based on the self-assembled DNA–MoS 2 nanosheet architecture for biomolecule detection. *Journal of Materials Chemistry B* **2**, 625–628 (2014).

60.   Johari, P. & Shenoy, V. B. Tuning the electronic properties of semiconducting transition metal dichalcogenides by applying mechanical strains. *ACS nano* **6**, 5449–5456 (2012).

61.   Shi, H., Pan, H., Zhang, Y.-W. & Yakobson, B. I. Quasiparticle band structures and optical properties of strained monolayer MoS 2 and WS 2. *Physical Review B* **87**, 155304 (2013).

62.   Rice, C. *et al.* Raman-scattering measurements and first-principles calculations of strain-induced phonon shifts in monolayer MoS 2. *Physical Review B* **87**, 081307 (2013).

63.   He, K., Poole, C., Mak, K. F. & Shan, J. Experimental demonstration of continuous electronic structure tuning via strain in atomically thin MoS2. *Nano letters* **13**, 2931–2936 (2013).

64.   Li, H. *et al.* Optoelectronic crystal of artificial atoms in strain-textured molybdenum disulphide. *Nature communications* **6**, 1–7 (2015).

65.   Tyurnina, A. V. *et al.* Strained bubbles in van der Waals heterostructures as local emitters of photoluminescence with adjustable wavelength. *ACS Photonics* **6**, 516–524 (2019).

66.   Feng, J., Qian, X., Huang, C.-W. & Li, J. Strain-engineered artificial atom as a broad-spectrum solar energy funnel. *Nature Photonics* **6**, 866 (2012).

67.   Fu, X. *et al.* Tailoring Exciton Dynamics by Elastic Strain-Gradient in Semiconductors. *Advanced Materials* **26**, 2572–2579 (2014).

68.   Fry, E. S., Musser, J., Kattawar, G. W. & Zhai, P.-W. Integrating cavities: temporal response. *Applied optics* **45**, 9053–9065 (2006).

69.   Cone, M. T., Musser, J. A., Figueroa, E., Mason, J. D. & Fry, E. S. Diffuse reflecting material for integrating cavity spectroscopy, including ring-down spectroscopy. *Applied optics* **54**, 334–346 (2015).

70.   Elterman, P. Integrating cavity spectroscopy. *Applied Optics* **9**, 2140–2142 (1970).

71.   Fry, E. S., Kattawar, G. W. & Pope, R. M. Integrating cavity absorption meter. *Applied optics* **31**, 2055–2065 (1992).

72.   Bixler, J. N. *et al.* Ultrasensitive detection of waste products in water using fluorescence emission cavity-enhanced spectroscopy. *Proceedings of the National Academy of Sciences* **111**, 7208–7211 (2014).

73. Cone, M. T. *et al.* Measuring the absorption coefficient of biological materials using integrating cavity ring-down spectroscopy. *Optica* **2**, 162–168 (2015).

74. Trivellin, N. *et al.* Inactivating SARS-CoV-2 Using 275 nm UV-C LEDs through a Spherical Irradiation Box: Design, Characterization and Validation. *Materials* **14**, 2315 (2021).

75. Janecek, M. Reflectivity spectra for commonly used reflectors. *IEEE Transactions on Nuclear Science* **59**, 490–497 (2012).

76. Weidner, V. R. & Hsia, J. J. Reflection properties of pressed polytetrafluoroethylene powder. *Josa* **71**, 856–861 (1981).

77. Xie, X. *et al.* An infectious cDNA clone of SARS-CoV-2. *Cell host & microbe* **27**, 841–848 (2020).

78. Rockey, N. C., Henderson, J. B., Chin, K., Raskin, L. & Wigginton, K. R. Predictive modeling of virus inactivation by UV. *Environmental Science & Technology* **55**, 3322–3332 (2021).

79. Zhang, W., Lockey, R. F. & Mohapatra, S. S. Respiratory syncytial virus: immunopathology and control. *Expert review of clinical immunology* **2**, 169–179 (2006).

80. Setlow, R. B., Swenson, P. A. & Carrier, W. L. Thymine dimers and inhibition of DNA synthesis by ultraviolet irradiation of cells. *Science* **142**, 1464–1466 (1963).

81. Li, R., Dhankhar, D., Chen, J., Cesario, T. C. & Rentzepis, P. M. A tryptophan synchronous and normal fluorescence study on bacteria inactivation mechanism. *Proceedings of the National Academy of Sciences* **116**, 18822–18826 (2019).

82. Boyce, J. M. & Donskey, C. J. Understanding ultraviolet light surface decontamination in hospital rooms: A primer. *Infection Control & Hospital Epidemiology* **40**, 1030–1035 (2019).

83. Watanabe, M. *et al.* Inactivation effects of UV irradiation and ozone treatment on the yeast and the mold in mineral water. *Journal of food protection* **73**, 1537–1542 (2010).

84. Zhu, Y. *et al.* Antifouling performance of polytetrafluoroethylene and polyvinylidene fluoride ultrafiltration membranes during alkali/surfactant/polymer flooding wastewater treatment: Distinctions and mechanisms. *Science of the total environment* **642**, 988–998 (2018).

85. Matsumura, Y. & Ananthaswamy, H. N. Toxic effects of ultraviolet radiation on the skin. *Toxicology and applied pharmacology* **195**, 298–308 (2004).

86. Withers, Z. H. & Voronine, D. V. Quantum medicine with ultraviolet aluminum nanolasers. *IEEE Journal of Selected Topics in Quantum Electronics* **25**, 1–6 (2018).

87. Mak, K. F., Lee, C., Hone, J., Shan, J. & Heinz, T. F. Atomically thin MoS 2: a new direct-gap semiconductor. *Physical review letters* **105**, 136805 (2010).

88. Splendiani, A. *et al.* Emerging photoluminescence in monolayer MoS2. *Nano letters* **10**, 1271–1275 (2010).

89. Geim, A. K. & Grigorieva, I. V. Van der Waals heterostructures. *Nature* **499**, 419–425 (2013).

90. Schaibley, J. R. *et al.* Valleytronics in 2D materials. *Nature Reviews Materials* **1**, 1–15 (2016).

91. Zhang, Z. *et al.* Robust epitaxial growth of two-dimensional heterostructures, multiheterostructures, and superlattices. *Science* **357**, 788–792 (2017).

92.   Sahoo, P. K., Memaran, S., Xin, Y., Balicas, L. & Gutiérrez, H. R. One-pot growth of two-dimensional lateral heterostructures via sequential edge-epitaxy. *Nature* **553**, 63–67 (2018).

93.   Zabel, J. *et al.* Raman spectroscopy of graphene and bilayer under biaxial strain: bubbles and balloons. *Nano letters* **12**, 617–621 (2012).

94.   Khestanova, E., Guinea, F., Fumagalli, L., Geim, A. K. & Grigorieva, I. V. Universal shape and pressure inside bubbles appearing in van der Waals heterostructures. *Nature communications* **7**, 1–10 (2016).

95.   Bertolazzi, S., Brivio, J. & Kis, A. Stretching and breaking of ultrathin MoS2. *ACS nano* **5**, 9703–9709 (2011).

96.   Johari, P. & Shenoy, V. B. Tuning the electronic properties of semiconducting transition metal dichalcogenides by applying mechanical strains. *ACS nano* **6**, 5449–5456 (2012).

97.   Conley, H. J. *et al.* Bandgap engineering of strained monolayer and bilayer MoS2. *Nano letters* **13**, 3626–3630 (2013).

98.   Darlington, T. P. *et al.* Imaging strain-localized excitons in nanoscale bubbles of monolayer WSe 2 at room temperature. *Nature Nanotechnology* 1–7 (2020).

99.   Levy, N. *et al.* Strain-induced pseudo–magnetic fields greater than 300 tesla in graphene nanobubbles. *Science* **329**, 544–547 (2010).

100. Klimov, N. N. *et al.* Electromechanical properties of graphene drumheads. *Science* **336**, 1557–1561 (2012).

101. Palacios-Berraquero, C. *et al.* Large-scale quantum-emitter arrays in atomically thin semiconductors. *Nature communications* **8**, 1–6 (2017).

102. Shepard, G. D. *et al.* Nanobubble induced formation of quantum emitters in monolayer semiconductors. *2D Materials* **4**, 021019 (2017).

103. Amani, M. *et al.* Near-unity photoluminescence quantum yield in MoS2. *Science* **350**, 1065–1068 (2015).

104. Amani, M. *et al.* Recombination kinetics and effects of superacid treatment in sulfur-and selenium-based transition metal dichalcogenides. *Nano letters* **16**, 2786–2791 (2016).

105. Feng, J., Qian, X., Huang, C.-W. & Li, J. Strain-engineered artificial atom as a broad-spectrum solar energy funnel. *Nature Photonics* **6**, 866 (2012).

106. Li, H. *et al.* Optoelectronic crystal of artificial atoms in strain-textured molybdenum disulphide. *Nature communications* **6**, 1–7 (2015).

107. Bao, W. *et al.* Visualizing nanoscale excitonic relaxation properties of disordered edges and grain boundaries in monolayer molybdenum disulfide. *Nature communications* **6**, 1–7 (2015).

108. Lee, Y. *et al.* Characterization of the structural defects in CVD-grown monolayered MoS 2 using near-field photoluminescence imaging. *Nanoscale* **7**, 11909–11914 (2015).

109. Su, W., Kumar, N., Mignuzzi, S., Crain, J. & Roy, D. Nanoscale mapping of excitonic processes in single-layer MoS 2 using tip-enhanced photoluminescence microscopy. *Nanoscale* **8**, 10564–10569 (2016).

110. Okuno, Y. *et al.* Probing the nanoscale light emission properties of a CVD-grown MoS 2 monolayer by tip-enhanced photoluminescence. *Nanoscale* **10**, 14055–14059 (2018).

111. Kastl, C. *et al.* The important role of water in growth of monolayer transition metal dichalcogenides. *2D Materials* **4**, 021024 (2017).

112. Lee, Y. *et al.* Near-field spectral mapping of individual exciton complexes of monolayer WS 2 correlated with local defects and charge population. *Nanoscale* **9**, 2272–2278 (2017).

113. He, Z. *et al.* Quantum plasmonic control of trions in a picocavity with monolayer WS$_2$. *Science advances* **5**, eaau8763 (2019).

114. Park, K.-D. *et al.* Hybrid tip-enhanced nanospectroscopy and nanoimaging of monolayer WSe2 with local strain control. *Nano letters* **16**, 2621–2627 (2016).

115. Park, K.-D., Jiang, T., Clark, G., Xu, X. & Raschke, M. B. Radiative control of dark excitons at room temperature by nano-optical antenna-tip Purcell effect. *Nature nanotechnology* **13**, 59–64 (2018).

116. Xue, W. *et al.* Nano-optical imaging of monolayer MoSe2-WSe2 lateral heterostructure with subwavelength domains. *Journal of Vacuum Science & Technology A: Vacuum, Surfaces, and Films* **36**, 05G502 (2018).

117. Kim, Y., Yun, S. J., Lee, E. & Kim, J. Near-field visualization of charge transfer at MoSe 2/WSe 2 lateral heterojunction. *Optical Materials Express* **9**, 1864–1871 (2019).

118. Sahoo, P. K. *et al.* Probing nano-heterogeneity and aging effects in lateral 2D heterostructures using tip-enhanced photoluminescence. *Optical Materials Express* **9**, 1620–1631 (2019).

119. Tang, C. *et al.* Quantum plasmonic hot-electron injection in lateral WS e 2/MoS e 2 heterostructures. *Physical Review B* **98**, 041402 (2018).

120. Castellanos-Gomez, A. *et al.* Local strain engineering in atomically thin MoS2. *Nano letters* **13**, 5361–5366 (2013).

121. Bhattarai, A. *et al.* Tip-enhanced Raman scattering from nanopatterned graphene and graphene oxide. *Nano Letters* **18**, 4029–4033 (2018).

122. Zeng, Y. *et al.* Synergetic photoluminescence enhancement of monolayer MoS 2 via surface plasmon resonance and defect repair. *RSC advances* **8**, 23591–23598 (2018).

123. Bellus, M. Z. *et al.* Photocarrier Transfer across Monolayer MoS2–MoSe2 Lateral Heterojunctions. *ACS nano* **12**, 7086–7092 (2018).

124. Tang, C. *et al.* Quantum plasmonic hot-electron injection in lateral $WSe_2/MoSe_2$ heterostructures. *Physical Review B* **98**, 041402 (2018).

125. Withers, Z. H. *et al.* Picoscale control of quantum plasmonic photoluminescence enhancement at 2D lateral heterojunction. *arXiv preprint arXiv:2001.10138* (2020).

126. Zhang, Y. *et al.* Improving resolution in quantum subnanometre-gap tip-enhanced Raman nanoimaging. *Scientific reports* **6**, 1–9 (2016).

127. Kravtsov, V., Berweger, S., Atkin, J. M. & Raschke, M. B. Control of plasmon emission and dynamics at the transition from classical to quantum coupling. *Nano letters* **14**, 5270–5275 (2014).

128. Robert, C. *et al.* Exciton radiative lifetime in transition metal dichalcogenide monolayers. *Physical review B* **93**, 205423 (2016).

129. Tang, C. *et al.* Quantum plasmonic hot-electron injection in lateral WS e 2/MoS e 2 heterostructures. *Physical Review B* **98**, 041402 (2018).

130. Ojeda, J. J. & Dittrich, M. Fourier transform infrared spectroscopy for molecular analysis of microbial cells. in *Microbial Systems Biology* 187–211 (Springer, 2012).

131. Phillips, A. P. & Martin, K. L. Limitations of flow cytometry for the specific detection of bacteria in mixed populations. *Journal of immunological methods* **106**, 109–117 (1988).

132. Nebe-von-Caron, G., Stephens, P. J., Hewitt, C. J., Powell, J. R. & Badley, R. A. Analysis of bacterial function by multi-colour fluorescence flow cytometry and single cell sorting. *Journal of microbiological methods* **42**, 97–114 (2000).

133. Naumann, D., Helm, D. & Labischinski, H. Microbiological characterizations by FT-IR spectroscopy. *Nature* **351**, 81–82 (1991).

134. Nemeth, J., Oesch, G. & Kuster, S. P. Bacteriostatic versus bactericidal antibiotics for patients with serious bacterial infections: systematic review and meta-analysis. *Journal of Antimicrobial Chemotherapy* **70**, 382–395 (2015).

135. Kohanski, M. A., Dwyer, D. J. & Collins, J. J. How antibiotics kill bacteria: from targets to networks. *Nature Reviews Microbiology* **8**, 423–435 (2010).

136. Becker, K. *et al.* Fourier-transform infrared spectroscopic analysis is a powerful tool for studying the dynamic changes in Staphylococcus aureus small-colony variants. *Journal of clinical microbiology* **44**, 3274–3278 (2006).

137. Al-Qadiri, H. M. *et al.* Studying of the bacterial growth phases using fourier transform infrared spectroscopy and multivariate analysis. *Journal of Rapid Methods & Automation in Microbiology* **16**, 73–89 (2008).

138. Amiali, N. M. *et al.* Evaluation of Fourier transform infrared spectroscopy for the rapid identification of glycopeptide-intermediate Staphylococcus aureus. *Journal of antimicrobial chemotherapy* **61**, 95–102 (2008).

139. Rodriguez, M. P. Q. Fourier transform infrared (FTIR) technology for the identification of organisms. *Clinical Microbiology Newsletter* **22**, 57–61 (2000).

140. Jiang, W. *et al.* Elucidation of functional groups on gram-positive and gram-negative bacterial surfaces using infrared spectroscopy. *Langmuir* **20**, 11433–11442 (2004).

141. Sivakumaran, K. Spectroscopic Study of Characterisation of Commercial Drug and its Mixture. *Proc Indian Natn Sci Acad* **79**, 357-363 (2013)

142. Davis, R. & Mauer, L. J. Fourier transform infrared (FT-IR) spectroscopy: a rapid tool for detection and analysis of foodborne pathogenic bacteria. *Current research, technology and education topics in applied microbiology and microbial biotechnology* **2**, 1582–1594 (2010).

143. Mauer, L. J. & Reuhs, B. L. Mid-infrared sensors for the rapid analysis of select microbial food borne pathogens. *Wiley Handbook of Science and Technology for Homeland Security* 1–20 (2008).

144. Gan, L., Chen, S. & Jensen, G. J. Molecular organization of Gram-negative peptidoglycan. *Proceedings of the National Academy of Sciences* **105**, 18953–18957 (2008).

145. Mullineaux, C. W., Nenninger, A., Ray, N. & Robinson, C. Diffusion of green fluorescent protein in three cell environments in Escherichia coli. *Journal of bacteriology* **188**, 3442–3448 (2006).

146. Buszewski, B. *et al.* Assignment of functional groups in Gram-positive bacteria. *Journal of Analytical & Bioanalytical Techniques* **6**, 1 (2015).

147. Hay, M. B. & Myneni, S. C. Structural environments of carboxyl groups in natural organic molecules from terrestrial systems. Part 1: Infrared spectroscopy. *Geochimica et cosmochimica acta* **71**, 3518–3532 (2007).

148. Raetz, C. R. & Dowhan, W. Biosynthesis and function of phospholipids in Escherichia coli. *Journal of Biological Chemistry* **265**, 1235–1238 (1990).

149. Nguyen, N. X., Sarter, S., Nguyen, N. H. & Daniel, P. Detection of molecular changes induced by antibiotics in Escherichia coli using vibrational spectroscopy. *Spectrochimica Acta Part A: Molecular and Biomolecular Spectroscopy* **183**, 395–401 (2017).

150. Hashtroudi, H., Mackinnon, I. D. & Shafiei, M. Emerging 2D hybrid nanomaterials: towards enhanced sensitive and selective conductometric gas sensors at room temperature. *Journal of Materials Chemistry C* **8**, 13108–13126 (2020).

151. Ambardar, S., Kamh, R., Withers, Z. & Voronine, D. V. Coupling nanobubbles in 2D lateral heterostructures. *Nanoscale* **14**, 8050-8059 (2022).

152. Esteban, R., Borisov, A. G., Nordlander, P. & Aizpurua, J. Bridging quantum and classical plasmonics with a quantum-corrected model. *Nature communications* **3**, 1–9 (2012).

153. Zuloaga, J., Prodan, E. & Nordlander, P. Quantum description of the plasmon resonances of a nanoparticle dimer. *Nano letters* **9**, 887–891 (2009).

154. Zhu, W. & Crozier, K. B. Quantum mechanical limit to plasmonic enhancement as observed by surface-enhanced Raman scattering. *Nature communications* **5**, 1–8 (2014).

155. Halas, N. J., Lal, S., Chang, W.-S., Link, S. & Nordlander, P. Plasmons in strongly coupled metallic nanostructures. *Chemical reviews* **111**, 3913–3961 (2011).

156. Tame, M. S. *et al.* Quantum plasmonics. *Nature Physics* **9**, 329–340 (2013).

157. Scholl, J. A., García-Etxarri, A., Koh, A. L. & Dionne, J. A. Observation of quantum tunneling between two plasmonic nanoparticles. *Nano letters* **13**, 564–569 (2013).

158. Savage, K. J. *et al.* Revealing the quantum regime in tunnelling plasmonics. *Nature* **491**, 574–577 (2012).

159. Zhu, W. *et al.* Quantum mechanical effects in plasmonic structures with subnanometre gaps. *Nature communications* **7**, 1–14 (2016).

160. Korea, C.-G., Badouraly, R., Prevost, M.-C., Ghigo, J.-M. & Beloin, C. Escherichia coli K-12 possesses multiple cryptic but functional chaperone–usher fimbriae with distinct surface specificities. *Environmental microbiology* **12**, 1957–1977 (2010).

161. Berne, C., Ducret, A., Hardy, G. G. & Brun, Y. V. Adhesins involved in attachment to abiotic surfaces by Gram-negative bacteria. *Microbial biofilms* 163–199 (2015).

162. Donlan, R. M. Biofilms: microbial life on surfaces. *Emerging infectious diseases* **8**, 881 (2002).

163. Monds, R. D. & O'Toole, G. A. The developmental model of microbial biofilms: ten years of a paradigm up for review. *Trends in microbiology* **17**, 73–87 (2009).

164. O'Toole, G., Kaplan, H. B. & Kolter, R. Biofilm formation as microbial development. *Annual review of microbiology* **54**, 49 (2000).

165. Garnett, J. A. *et al.* Structural insights into the biogenesis and biofilm formation by the Escherichia coli common pilus. *Proceedings of the National Academy of Sciences* **109**, 3950–3955 (2012).

166. Roux, A., Beloin, C. & Ghigo, J.-M. Combined inactivation and expression strategy to study gene function under physiological conditions: application to identification of new Escherichia coli adhesins. *Journal of bacteriology* **187**, 1001–1013 (2005).

167. Martinez-Gil, M. *et al.* YeeJ is an inverse autotransporter from Escherichia coli that binds to peptidoglycan and promotes biofilm formation. *Scientific reports* **7**, 1–16 (2017).

168. Sahoo, P. K. *et al.* Nanowire arrays as cell force sensors to investigate adhesin-enhanced holdfast of single cell bacteria and biofilm stability. *Nano letters* **16**, 4656–4664 (2016).

169. Janissen, R. *et al.* Spatiotemporal distribution of different extracellular polymeric substances and filamentation mediate Xylella fastidiosa adhesion and biofilm formation. Sci Rep 5: 9856. (2015).

170. Ma, L. *et al.* Assembly and development of the Pseudomonas aeruginosa biofilm matrix. *PLoS pathogens* **5**, e1000354 (2009).

171. Laloux, G. & Jacobs-Wagner, C. How do bacteria localize proteins to the cell pole? *Journal of cell science* **127**, 11–19 (2014).

172. Vosbeck, K., Mett, H., Huber, U., Bohn, J. & Petignat, M. Effects of low concentrations of antibiotics on Escherichia coli adhesion. *Antimicrobial Agents and Chemotherapy* **21**, 864–869 (1982).

173. Marinica, D. C., Kazansky, A. K., Nordlander, P., Aizpurua, J. & Borisov, A. G. Quantum plasmonics: nonlinear effects in the field enhancement of a plasmonic nanoparticle dimer. *Nano letters* **12**, 1333–1339 (2012).

174. Ward, D. R., Hüser, F., Pauly, F., Cuevas, J. C. & Natelson, D. Optical rectification and field enhancement in a plasmonic nanogap. *Nature nanotechnology* **5**, 732–736 (2010).

175. Fursey, G. N. Field emission in vacuum micro-electronics, Kluwer Academic Plenum Publishers. (2005).

176. Wu, L. & Ang, L. K. Nonequilibrium model of ultrafast laser-induced electron photofield emission from a dc-biased metallic surface. *Physical Review B* **78**, 224112 (2008).

177. Child, C. D. Discharge from hot CaO. *Physical Review (Series I)* **32**, 492 (1911).

178. Wu, L. *et al.* Fowler–Nordheim tunneling induced charge transfer plasmons between nearly touching nanoparticles. *ACS nano* **7**, 707–716 (2013).

Appendix A: Copyright Permission for Figure 1.1

Appendix B: Copyright Permission for Figure 1.2

Copyright and permission request for 1 figure from the article "Nano-optical imaging of monolayer MoSe2-WSe2 lateral heterostructure with subwavelength domains"

JVST@jvst.org
To: Sharad Ambardar

Tue 6/21/2022 10:18 AM

Dear Mr. Ambardar,

Thank you for reaching our regarding your previous publication in *JVST A*. You do not need formal permission to reuse your own figure in your dissertation, so please proceed with including it. We only ask that you acknowledge the original source using the following format:

"Reproduced with permission from [Full Citation], Copyright AVS [Year]."

Please let me know if you have any other questions.

Regards,
Rachel Bayne
AVS Publications Office Manager

****

*Science and Technology
of Materials, Interfaces, and Processing*

51 Kilmayne Drive, Suite 201
Cary, NC 27511
Phone: 919-361-2728
jvst@jvst.org
AVS Digital Library

Appendix C: Copyright Permission for Figure 1.3

Appendix D: Copyright Permission for Chapter 2

License agreement and author copyright

Appendix E: Copyright Permission for Chapter 3

Copyright/permission request for published article "Coupling nanobubbles in 2D lateral heterostructures"

Nanoscale (shared) <nanoscale@rsc.org>
To: Sharad Ambardar

Mon 6/20/2022 5:46 AM

Dear Mr Ambardar,

Thank you for your email. Permission is granted to reproduce your article in your thesis as long as it is fully acknowledged and includes a link back to the article on our website. Please ensure that all authors are aware that it is being included.

If you have any further questions, please let me know.

Best wishes,
Lee

Lee Colwill (they/them)
Publishing Assistant, Journals
Royal Society of Chemistry

www.rsc.org

| Great, thank you so much! | Thank you so much! I really appreciate it! | Thank you for your confirmation. |

Are the suggestions above helpful?   Yes   No

Appendix F: Copyright Permission for Chapter 4